PEM FUEL CELL ELECTRODES: NANOFIBER-BASED HYBRID AND CeO_2 INCLUDED ELECTRODES FOR BOOSTED PERFORMANCE

by

BILAL ISKANDARANI

Submitted to the Graduate School of Engineering and Natural Sciences in partial fulfillment of the requirements for the degree of Doctor of Philosophy

Sabancı University

December, 2022

PEM FUEL CELL ELECTRODES: NANOFIBER-BASED HYBRID AND CeO_2 INCLUDED ELECTRODES FOR BOOSTED PERFORMANCE

APPROVED BY:

DATE OF APPROVAL:

ABSTRACT

PEM FUEL CELL ELECTRODES: NANOFIBER-BASED HYBRID AND CeO_2 INCLUDED ELECTRODES FOR BOOSTED PERFORMANCE

BILAL ISKANDARANI

Materials Science and Engineering, Ph.D. Dissertation, December 2022

Supervisor: Prof. Dr. Selmiye Alkan Gürsel

Co-supervisor: Dr. Begüm Yarar Kaplan

Keywords: PEM fuel cells, electrodes, fibers, sulfonated silica, cerium oxide

PEM fuel cells have become increasingly drawn attention in numerous applications during the past decade. However, PEM fuel cells suffer from a number of drawbacks such as;the high Pt and Nafion® utilization within the electrodes exhibits a significant financial burden. Furthermore, the catalyst layer undergoes a number of side-processes during operation resulting in its deterioration and loss in performance with time. To address those issues, fiber-based electrodes were fabricated using electrospinning utilizing Pt/C as a catalyst, sulfonated silica as a proton conducting ionomer, and poly (vinylidene fluoride-trifluoroethylene) P(VDF-TrFE) as a carrier polymer. The fabricated electrodes demonstrated a functional and Nafion®-free cost-effective alternative to classically sprayed electrodes. They exhibited superior performance recording up to 417.7 $mW.cm^{-2}$ maximum power density exceeding that of sprayed electrodes and fiber-based electrodes employing Nafion®. Furthermore, the aforementioned electrodes showed impressive durability against Pt-dissolution retaining up to 86.5% and exhibited a 2.6% gain in performance under C-corrosion AST. In the second part of the dissertation, CeO_2-based additives were investigated to enhance the oxygen reduction reaction kinetics. Nanorod CeO_2/NrGO, bare nanorod CeO_2, nanocube, and nano octahedral

CeO_2 exhibited an overall increase in the ORR activity with octahedral CeO_2 recording the highest power output (483.4 $mW.cm^{-2}$). Furthermore, cerium oxide nanocube additive-based electrodes exhibited an impressive durability retaining up to 80.3% of its initial maximum power density.

.

ÖZET

PEM YAKIT HÜCRESİ ELECTROLARI: NANOFİBER BAZLI HİBRİT VE CeO_2 İCEREN YÜKSEK PERFORMANSLI ELECTROLAR

BILAL ISKANDARANI

Malzeme Bilimi ve Mühendislik , Doktora Tezi, Aralık 2022

Danışman: Prof. Dr. Selmiye Alkan Gürsel

Eş-danışman: Dr. Begüm Yarar Kaplan

Anahtar Kelimeler: PEM yakıt hücreleri, elektrotlar, lifler, sülfonlanmış silika, seryum oksit

PEM yakıt hücreleri, özellikle son on yılda pek çok uygulama alanında kullanılabiliyor olmalarıyla dikkat çekti. Bununla birlikte, ne yazık ki PEM yakıt hücrelerinin birtakım dezavantajları mevcuttur. Örneğin, elektrotlar içinde yüksek platin ve Nafion® kullanımı PEM yakıt hücrelerinin maliyetini ciddi ölçüde arttırmaktadır. Ayrıca PEM yakıt hücreleri çalışma sırasında, katalizör katmanının zamanla bozulmasına ve performans kaybına neden olan bir takım yan işlemlerden geçer. Bu sorunlara bir çözüm bulmak adına, elektrospinning yöntemi kullanılarak fiber bazlı elektrotlar üretilmiş, katalizör olarak Pt/C, proton ileten iyonomer olarak sülfonatlı silika ve taşıyıcı polimer olarak poli (viniliden florür-trifloroetilen) P(VDF-TrFE) kullanılmıştır. Üretilen bu elektrotlar, konvansiyonel olarak püskürtme yöntemiyle üretilen elektrotlara karşı işlevsel ve Nafion® içermeyen uygun maliyetli bir alternatif olabileceğini kanıtlamış; 417.7 $mW.cm^{-2}$ maksimum güç yoğunluğuna ulaşarak püskürtme yöntemiyle üretilen elektrotları ve Nafion® kullanan fiber bazlı elektrotları geride bırakmış ve üstün bir performans sergilemiştir. Ayrıca üretilen bu elektrotlar, platin çözümesine karşı etkili bir dayanım göstermiş, ilk performansının %86,5'ini korumuş ve C-korozyonu AST testinde %2,6'lık performans artışı sağlamıştır. Tezin ikinci bölümünde ise, CeO_2 bazlı katkı malzemeleri kullanarak oksijen indirgenme tepkimesinin kinetiğinin geliştirilmesi incelenmiştir. NrGO takviyeli Nanoçubuk CeO_2, saf nanoçubuk, nanoküp, ve nanooktahedral CeO_2,

ORR aktivitesini artış sağlamış, bu malzemelerden en yuksek güç çıkışını oktahedral CeO_2 göstermiştir (483.4 $mW.cm^{-2}$). Buna ek olarak, CeO_2 nanoküp katkı malzemeli elektrotlar, başlangıçtaki maksimum güç yoğunluğunun %80,3'ünü muhafaza ederek üstün bir dayanıklılık göstermiştir.

Acknowledgements

I would like to thank my advisor Prof. Dr. Selmiye Alkan Gürsel and my co-advisor Dr, Begüm Yarar Kaplan for their constant support during my PhD. Furthermore, I would like to thank Assoc. Prof. Dr. Alp Yürüm for his kind mentoring and supervision in a number of projects. I was pleased to have Alp Yürüm around to take his advice and discuss my results and future projects. I have learned from all three of my supervisors a lot. I can now say that the "Bilal" that once joined the energy storage and conversion research group is not the one who is now at the cliff of graduation. They have given me numerous opportunities to evolve and sculpture my background, knowledge, and technical experience. Furthermore, they were in the front supporting lines throughout my PhD journey. For that, I cannot find a word meaningful enough to express my gratitude for their effort and patience during my entire journey in ECS group.

Of course, the journey of PhD student is not only summarized within his relationship with his supervisors. I was lucky to have my support system with me all along. Those people supported me on a professional, personal, and even emotional level. I do not remember them turning me down once. Those are the members of the ESC group. I would like to thank them all for their constant valuable support. This gratitude goes in particular to Ali Ansari Hamedani, Vahid Charkhesht, Adnan Taşdemir, Mohammad Zabara, Naeimeh Rajabalizadeh, Ahmet Can Kırlıoğlu, Navid Haghmoradi, Burak, Buse, Hamed, and Aysu. Outside the group, I would like to thank my friends whom I met at or outside Sabanci University and who accompanied me throughout my entire journey. In particular, I would like to thank my friend Dr. Bilal El khatib for being a friend and for the numerous times I learned from him.

I would also like to thank my city, Beirut. The city that I was raised in. The city where I have been taught my morals that still to date are impressive wherever I go. This city is

indeed not going through its best days. But the city was always giving us a reason to love it. The righteous people I met over there are one of the reasons for my love towards this city. Tough days or not, I love you Beirut.

A family can be one's shield against hardships. For me, my family was one of the major reasons behind my success. I can still see flashbacks of my mother waking me up for school every morning. I can still recall the memory of how she was striving to make me a better person. My father, who till date still works despite his old age. Throughout the struggles and hardships, he was always a role model for us in endurance. He, along my mother raised me properly to strive behind what I want and endure the hardships. Then comes my siblings who all gave me support each in his/her way. Ghina, Fuad, Mohammad, and Hiba, despite being far away in separate countries, they never failed to make me feel that I have a family. In the days when family values are diminishing and strong ties are breaking, thank you all for preserving this one important unit in my life.

I hope I can make all proud in my next chapters and steps.

Bilal Iskandarani

Table of Content

List of Figures

List of Tables

CHAPTER 1: INTRODUCTION

1.1. Background and Motivation

In the scope of fossil fuels reserve decline and the shift in strategy towards renewable energy resources, fuel cells are becoming famously utilized in a significant number of applications. Fuel cells are energy conversion units which convert chemical energy into electrical energy. Like all electrochemical systems, they are composed of a negative (anode) and a positive (cathode) electrode sandwiching a separating membrane. However, in fuel cells, hydrogen and oxygen gases are fed into the anode and the cathode, respectively. But, regardless of the great success fuel cell has achieved throughout time, several shortcomings slowed down its vast introduction into the market. For instance, the quantity of noble metal Pt and Nafion® required to maintain a reasonable performance and durability within the electrode poses a cost burden. Several electrode fabrication methods were utilized in quest of morphology that boosts the utilization of Pt within the electrode. However, electrospinning stands out as one of the most promising methods. Obtaining a fibrous architecture through electrospinning provides many advantages. First, it provides better exposure of the catalyst surface. Second, the fibrous morphology enhances the in/out diffusion of reactant gases and produced water in the electrode, respectively.

Of equal importance, Nafion® ionomer is extensively used in both PEM fuel cell membranes and electrode. Within the electrode, Nafion® serves in conducting protons into the electrochemical active center (Pt). However, and in addition to the high cost of Nafion®, its proton conduction declines dramatically in partially humidified conditions. In parallel, Sulfonated silica (S-SiO_2) emerged as a successful alternative to Nafion®. Unlike Nafion®, the hydroscopic backbone of sulfonated silica allows it to maintain adequate performance at flexible humidity conditions. Furthermore, in comparison to Nafion®, the smaller size of sulfonated silica enables it to reach Pt particles embedded within the electrode interior provoking better Pt utilization.

In parallel, catalyst enhancing electrode additive development and usage has been on a rise lately. Those additives serve in providing a favorable environment to alleviate the sluggish kinetics of the oxygen reduction reaction occurring in the cathode. On the other hand, Cerium oxide (Ceria; CeO_2) is well known as an oxygen buffer. Therefore, incorporating CeO_2 or CeO_2-based materials as additives in the electrode can serve in enhancing the oxygen gas accessibility to the electrochemical active centers and thereby boost its ORR kinetics.

1.2. Dissertation Objectives

This study is designed to answer a number of questions within the area of PEMFC electrode design. With that being said, the ultimate goal of the studies conducted is to enhance both the performance and durability of PEMFC cathodes. In parallel, performance and durability enhancement are made while selecting cost effective components that can replace their expensive alternative. Therefore, the 1st objective was to fabricate a fiber-based cathodes using different hydrophobic carrier polymers (PVDF and P(VDF-TrfE)). Those electrodes are expected to not only utilize the fibrous structure of the electrode to boost its performance through better Pt exposure and mass transfer, but to utilize the hydrophobic nature of the carrier polymer to manage the water content in the electrode compartment and reduce the risk of performance fading. The 2nd objective in quest of enhancing the cathodes performance

and durability was to use a cost-effective, chemically stable, and hygroscopic inorganic proton conducting component within the cathode as an alternative to the expensive and hydrophobic Nafion® alternative. Therefore, the effect of introducing sulfonated silica (S-SiO_2) into the fiber-based cathode is to be investigated in depth to investigate its viability as an alternative to Nafion®. Finally, the 3rd objective is to investigate the effect of inorganic ceria (CeO_2)-based additives on the performance and durability of the cathode. Furthermore, it is intended to investigate the effect of the CeO_2 particle morphology on both the ORR reaction, PEMFC performance and durability.

1.3. Roadmap of Chapters

The current dissertation is designed to highlight the impact of electrospinning, sulfonated silica, and CeO_2/NrGO on both the performance and durability of a PEMFC cathode. Therefore, it starts with a general dissertation introduction in Chapter 1 including the motivation behind this work and the followed methodology defining PEM fuel cell electrodes and the importance of its different components, and electrospinning. Also, Chapter 1 surveys the use of Nafion® ionomer alternatives in the electrode with greater emphasis of inorganic based materials, and electrode additives. Chapter 2 defines and discusses the different characterization tools. Chapter 3 explains the fabrication of fibrous Pt/C/S-SiO_2/P(VDF-TrFE), and Pt/C/S-SiO_2/PVDF and their use as PEMFC electrode. Chapter 4 discusses the synthesis of CeO_2/NrGO and CeO_2 and their role as additives in PEMFC electrodes. Chapter 5 is a continuation of the previous chapter in which the effect of CeO_2 morphology on the performance and durability of PEMFC cathodes was investigated. Finally, Chapter 6 provides a summary, suggestions, and future work.

1.4. Principle of Polymer Electrolyte Fuel cells (PEMFCs)

Polymer electrolyte fuel cells (PEMFCs) are energy conversion devices which utilize chemical energy and convert it into electrical work. In the process, H_2 and O_2 gases are both fed into the cell to produce electrical work, heat energy, and water (Figure 1). PEMFC operates at relatively low temperatures (80-110^oC) compared to other fuel cell types. Therefore, PEMFC is regarded as low temperature fuel cell. This allows PEMFCs to have fast startup times and thus be used in a broad scope of applications, especially in mobile applications. Therefore, automobile manufacturers started introducing fuel cell vehicles (FCV) into the market starting from the year of 2014 when Hyundai Tucson was introduced with a 426 km range. Soon after, other automobile manufacturers like Honda and Toyota followed through the Honda clarity and Toyota Mirai, respectively.

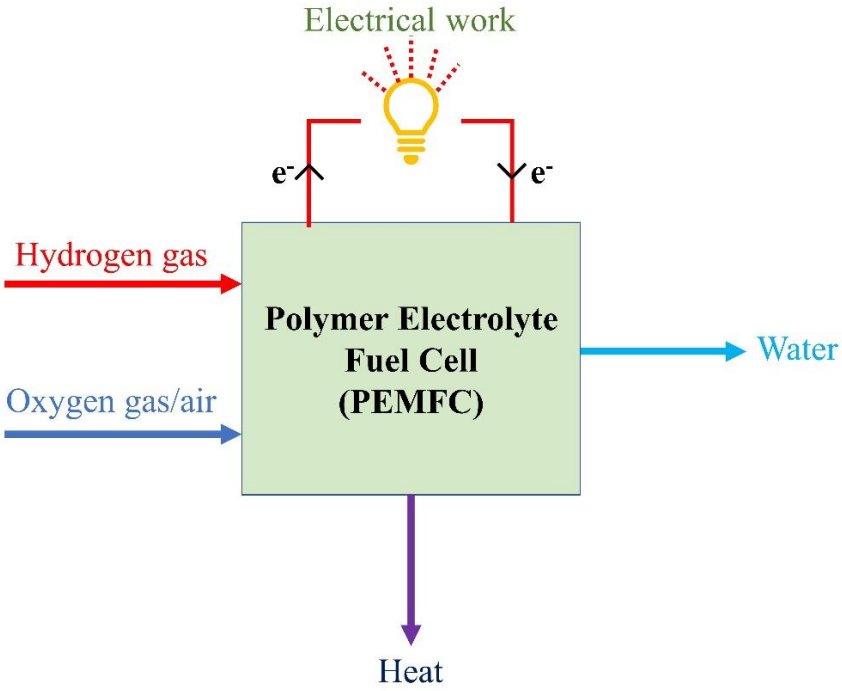

Figure 1: Polymer Electrolyte Membrane fuel cell (PEMFC) Schematic

Like any other electrochemical system, PEMFCs contain a cathode, and an anode brought together but separated using a proton conducting membrane. When assembled, the membrane electrode assembly (MEA) is regarded as the central component of PEMFCs. That is because electrochemical reaction occurs within the MEA. Hydrogen is mainly supplied to

the anode and undergoes oxidation producing protons and electrons. On the other hand, Oxygen gas fed to the cathode is reduced to water. The redox reaction happening within the MEA enables electrical current to pass through an external circuit and protons through the separating membrane (Figure 2). The electrochemical reactions happening on both electrodes are as follows:

Hydrogen oxidation reaction (HOR) (Anode):

$$2H_{2(g)} \rightarrow 4H^{+}_{(aq)} + 4e^{-} \quad (1.1)$$

Oxygen reduction reaction (ORR) (Cathode):

$$O_{2(g)} + 4H^{+}_{(aq)} + 4e^{-} \rightarrow 2H_2O_{(l)} \quad (1.2)$$

Overall redox reaction:

$$2H_{2(g)} + O_{2(g)} \rightarrow 2H_2O_{(l)} \quad (1.3)$$

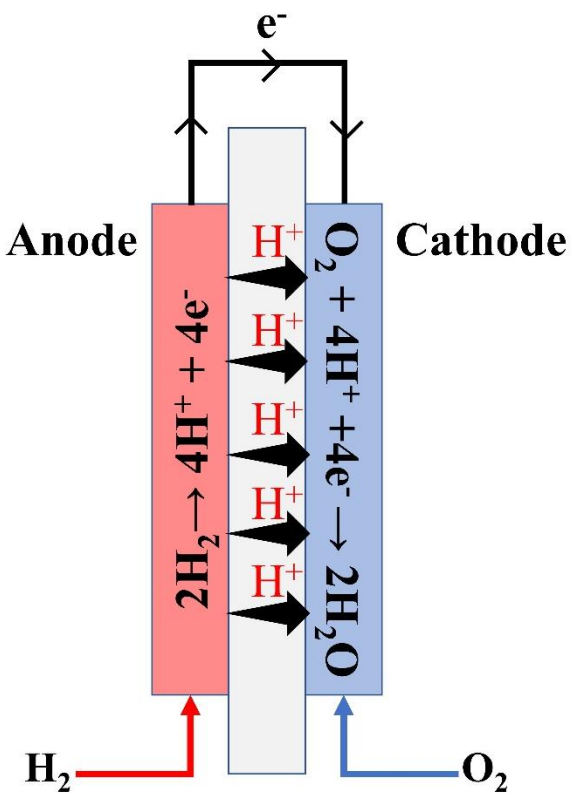

Figure 2: a Schematic representation of the MEA with reactions occurring on the Anode and the Cathode

1.5. Overpotential

When PEMFC MEA operates and star producing current, it shifts from its equilibrium condition. That is because of a number of processes occurring within the MEA causing a decline in voltage. As mentioned earlier in section 2.3, the voltage losses can be depicted by the following equation:

$$E_{cell} = E_{OCV}^{T,P} - \eta_{activation} - \eta_{ohmic} - \eta_{mass\ trasport} \quad (1.7)$$

Where E_{cell} is the voltage of the cell at a particular temperature, pressure, feed nature and rate, $E_{OCV}^{T,P}$ depicts the open circuit voltage at a particular temperature and pressure, and $\eta_{activation}$, η_{ohmic} ,and $\eta_{mass\ trasport}$ represent the activation, ohmic , and mass transport overpotentials , respectively. The mentioned overpotentials can be controlled by the set of parameters as shown in the following equation:

$$E_{cell} = E_{OCV}^{T,P} - \frac{RT}{aF}\ln\left(\frac{i}{i_0}\right) - i\,R_i - \frac{RT}{nF}\ln\left(\frac{i_L}{i_L - i}\right) \quad (1.8)$$

Where, in the activation potential, i is the current density expressed in mA/cm^2, R is the gas constant equal to 8.314 $J.mol^{-1}K^{-1}$, α is the transfer coefficient, F is Faraday's constant, i_0 is the exchange current density. The ohmic overpotential is depicted in a linear relation where R_i is the overall resistance of the MEA. In the mass transfer overpotential, i_L is the limiting current density. It is worth noting that both the activation and the mass transfer overpotential originate from Nernst equations.

Based on equation 1.8, we can notice that activation losses mainly contribute to overall overpotential at low current densities while mass transfer losses is the main contributor at high current density [2]. Therefore, subregions can be identified within the polarization curve as shown in Figure 3.

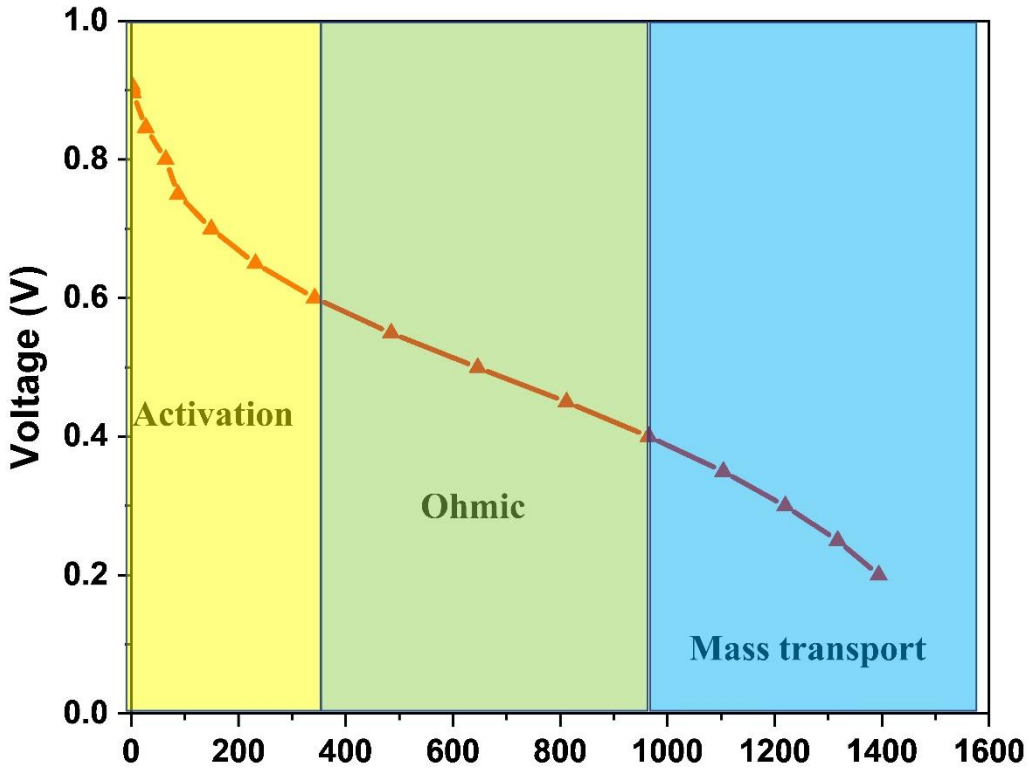

Figure 3: Polymer Electrolyte Membrane Fuel Cell polarization curve

1.6. The Cathode

In every electrochemical system, the cathode is the site accompanied by a reduction process. In the case of PEMFCs, oxygen gas is reduced at the cathode and the reduction product combines with the incoming protons to form a water molecule. The cathode is generally composed of a catalyst layer. In turn, the catalyst layer is turn composed of a catalyst representing the electrochemical sites connected with a network of ion conducting ionomer. Since the ORR is characterized by its slow kinetics, most research mainly focuses on

improving its performance through improving its components or the overall geometry of the fabricated cathode.

1.6.1. The Catalyst

Within the MEA, the cathode is where oxygen reduction occurs. In order for ORR, oxygen gas, protons, and electrons are required. Therefore, in order to maintain the supply of those three components, cathodes are generally composed of a catalyst, a proton conducting ionomer, and an electron conducting support.

Platinum (Pt); a noble metal; is widely known to be the most efficient ORR catalyst. It is known to exhibit acceptable performance and durability withstanding the harsh acidic conditions within the MEA during operation. The ORR reaction stems from the adsorption of oxygen onto the catalyst surface by which it interacts with electrons and protons to produce water [3]. Therefore, the optimal binding energy between the catalyst and the oxygen moieties is crucial for faster ORR. Some metals (example Ni) show a more negative binding energy than Pt. This higher binding energy alters the proton transfer step resulting in slowing down the ORR. On the other hand, loosely bounded oxygen moieties on metals exhibited a more positive binding energy than Pt result in the total disruption of proton conduction into oxygen [4].

Since the ORR is a surface phenomenon, nano sized Pt catalyst particles are generally used as a catalyst for PEM fuel cell. That is, the smaller size of the particle provides a larger area of interaction called the electrochemical surface area (ECSA) is directly correlated to the mass activity of the catalyst. However, some studies suggested that reducing the Pt particle size can have a negative effect. That is , upon that, the edges which constitute much of the Pt surface area show high binding energy towards Oxygen which can hinder the ORR [5, 6]. Therefore, Pt particles with optimal ORR activity were optimally exhibited by particles 2-4 nm in size.

In order to increase the ECSA of the Pt catalyst, Pt particles are loaded onto a high surface area supports such as carbon black, graphene, and carbon nanotubes. The broad surface areas, and high electrical conductivities exhibited by those supports serves in further enhancing the ORR kinetics [7]. That is, the high electrical conductivity characteristic of

carbon support serves in electron accumulation onto the surface of the Pt catalyst resulting in the accelerating the ORR [8]. In this sense, it has been manifested that Pt catalysts loaded onto electronically conductive carbon support show better performance. Furthermore, the carbon support serves in protecting the Pt particles from detachment, dissolution, Ostwald ripening, and agglomeration during operation. As it is during operation, weak Pt-support interaction could lead to the disintegration of the Pt from its corresponding support. Also, particles with close proximities can agglomerate or Ostwald ripening can occur resulting in diminishing the ECSA of the electrode. The occurrence of any of the three phenomena can result in the deterioration in the overall performance of the electrode.

1.6.2. The Proton Conducting Ionomer

The proton conducting ionomer plays a significant role within the electrode. As the name suggests, the ionomer facilitates proton transport into the electrochemical active centers. Nafion®; a sulfonated tetrafluoroethylene-based fluoropolymer-copolymer; developed by Dupont in the 1960s, is a widely used ionomer in PEMFCs (Figure 4). The wide utilization of Nafion® is attributed to the high exhibited proton conduction. In addition to that, Nafion® functions as a binder within the electrode preventing the formation of cracks during operation. Generally, Nafion® forms a thin film over the catalyst layer permitting the passage of the incoming H^+ towards the Nafion®/Pt interface [9, 10]. In addition, it permits the passage of dissolved oxygen [11]. The thickness of the Nafion® contributes significantly to the permittance or alteration of the performance of the MEA. A low amount of Nafion® within the electrode results in low conductivity, while very high Nafion® loading leads into the formation of thick films impeding the gas passage [12] . The studies have shown that a weight percent (%wt) of 30% is optimal for maximum performance [13]. That is, excess Nafion® content impedes the passage of oxygen into the electrochemical active centers.

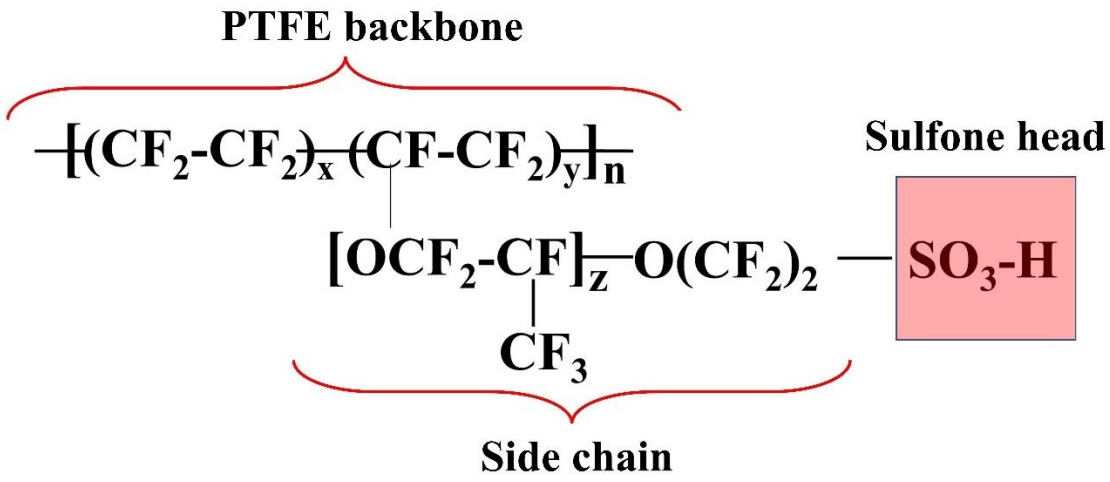

Figure 4: Nafion® Structure

In spite of the high proton conductivity exhibited by Nafion®, it can be only obtained when Nafion® is sufficiently hydrated. In fact, the proton conductivity of Nafion® drops dramatically in low humidity conditions [9]. This can be related to the hydrophobic nature of both the PTFE backbone and its side chain causing the collapse of the hydrophilic domains. Which means that Nafion® behaves as raw PTFE at low humidity conditions resulting in a decrease in its overall proton conductivity. In this sense, the conductivity of Nafion® can be tailored through controlling the equivalent weight (EW) of the PTFE backbone. The acidic site concentration increases upon decreasing the EW of PTFE backbone resulting in promoting the overall proton conductivity. Furthermore, it serves in thinning of Nafion® at the Pt interface serving in better O_2 permeation. On the other hand, varying the EW of the side chain has an implication on suppressing Pt surface poisoning through the Nafion® sulfone groups. For instance, the increase of the side chain EW is correlated with an increase in Pt surface poisoning [14].

1.7. The Triple Phase Boundary (TPB)

Protons and electrons produced at the anode and driven into the cathode through both the internal and external circuits, respectively. In parallel, oxygen diffuses within the free space. All three components require a common and simultaneous meeting point in the

electrode for the ORR reaction to occur. However, protons are ionically conducted through the proton conducting ionomer, electrons through the electrically conductive catalyst, and oxygen diffuses within the empty pores of the electrode. Therefore, the boundary between the catalyst, proton conducting ionomer, and air phases regarded as the triple phase boundary is where most of the ORR reaction occurs (Figure 5).

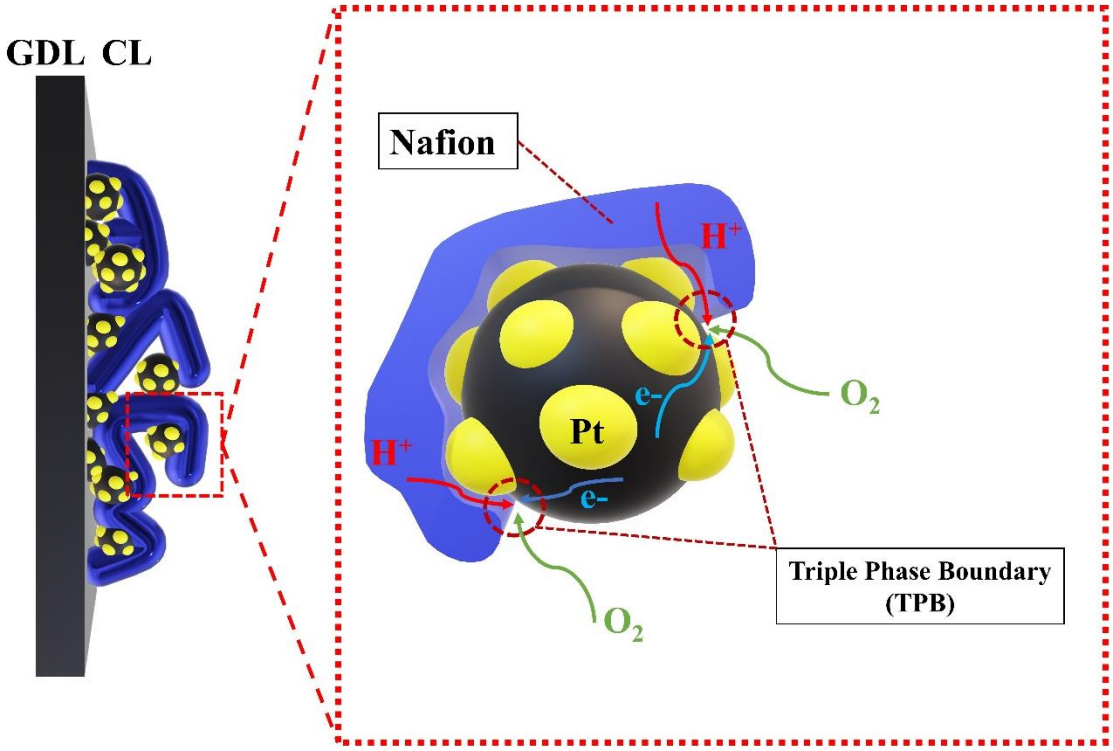

Figure 5: Schematic Representation of the triple phase boundary within the catalyst layer (CL)

1.8. Utilization of Sulfonated Silica (S-SiO_2) in PEMFC Electrodes

Substituting Nafion® as an ionomer within the electrode for a cheaper and similarly functional alternative has been in quest. Numerous hydrocarbon-based ionomers were investigated for that purpose such as sulfonated poly (ether ether) ketone (SPEEK) [15, 16], polyamides [17], polyphosphazene [18], and polysulfones [19]. However, despite their promising impact, their high boiling points and their miscibility in aprotic solvents were problematic [20, 21]. Those unevaporated liquid droplets can then deposit on the Pt surface

resulting in reducing its activity [22]. In this regard, inorganic-based proton conductive ionomers were introduced and heavily investigated as a suitable cheaper and good alternative for Nafion®. Namely, sulfonated silica (S-SiO_2) was one of the promising candidates. This is due the fact that sulfonated silica is expected to be multifunctional serving simultaneously in multiple processes. First, like Nafion®, the sulfone groups serve in conducting protons within the membrane. Second, unlike Nafion®, the hygroscopic nature of the silica backbone serves in water modulation within electrode. That was investigated by Eastcot and Easton. Here, although electrodes containing Nafion® were superior to S-SiO_2 electrodes in terms of performance in fully humidified conditions, the latter has shown a promising performance in dry conditions (20% RH) surpassing Nafion®. The hygroscopic effect of S-SiO_2 serves in the retention of water within the electrode and enhances the back-diffusion of water from the cathode into the membrane resulting in better membrane hydration during dry operation [23]. To compare electrochemical performance between S-SiO_2 and Nafion® within the MEA, Eastscot et al. investigated which included comparing the overpotentials and electrochemical impedance spectroscopy results of both MEAs in different humidity conditions. The EIS results showed a better proton conductivity and ionic resistance for the S-SiO_2 compared to Nafion®. On the other hand, upon testing the performance of both MEAs under 75% RH, S-SiO_2 containing MEA showed a limitation in the mass transport region compared to Nafion®. However, unlike Nafion®, this limitation was mitigated upon decreasing the % RH leading to an increase in performance. Furthermore, Nafion® containing MEAs recorded a lower ohmic overpotential compared to S-SiO_2 containing MEAs. This can be related to the enhanced interfacial resistance between the used Nafion® membrane and the Nafion® present in the electrode. However, that was not the case in dry conditions where S-SiO_2 containing MEAs recorded lower ohmic overpotential due to water back diffusion from the cathode. Likewise, S-SiO_2 containing cathodes recorded lower mass transport resistance in lower %RH [24]. In another study, Sulfonated silica was deposited onto Pt/C using a hydrothermal process. The produced catalyst was then sprayed onto a GDL and compared with Nafion® containing MEAs. Similar to the previous studies, the S-SiO_2 containing electrodes has suffered from mass transport limitations. In this study, the rising mass transport resistance is correlated with the higher porosity of S-SiO_2 resulting in the formation of thicker membranes [25]. The durability of S-SiO_2 containing cathodes was investigated and

compared with Nafion® containing cathodes. The former lost only 26 % of its initial ECSA after AST compared to 93% for that of Nafion® containing electrodes. This can originate from the positive electronic interaction between S-SiO_2 and the Pt catalyst resulting in minimal agglomeration and Ostwald ripening. This is due to the optimal distribution of S-

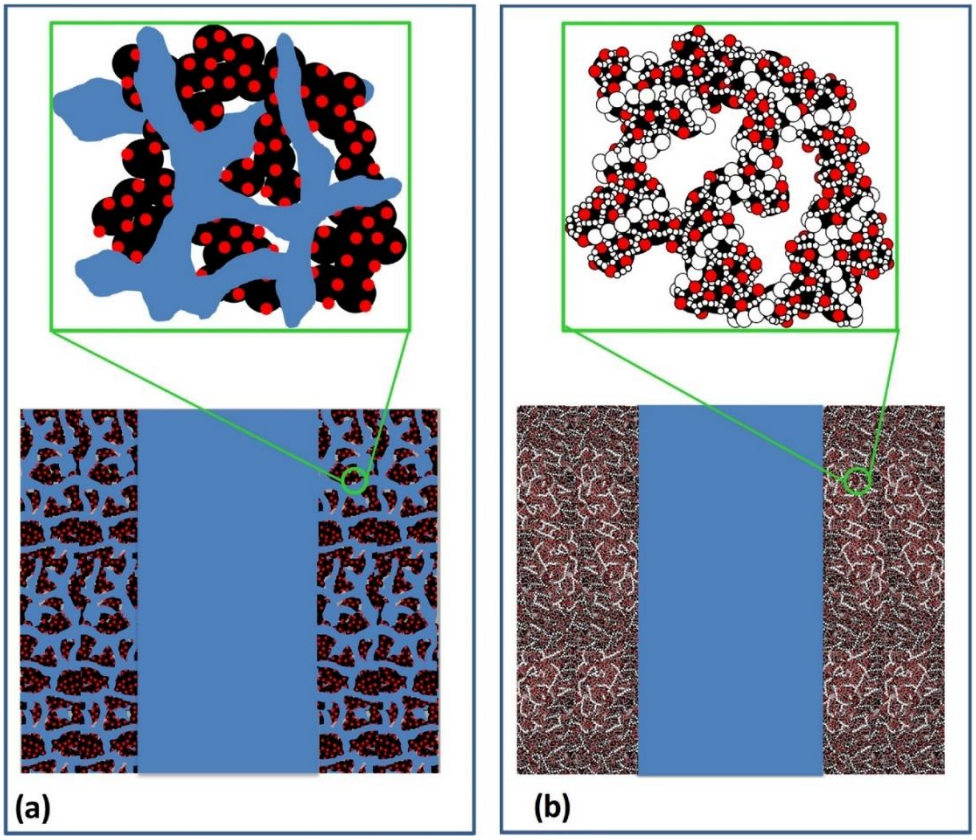

Figure 6:The catalyst layer microstructure of a) Nafion® and b) S-SiO_2 containing electrodes [1]

SiO_2 around the Pt catalyst and the interaction through the hydroxyl moieties of S-SiO_2 and Pt (Figure 6). As a result of that, Pt particles are stabilized, and particle growth is altered during operation. Therefore, S-SiO_2 was postulated to play multiple roles within the cathode [1]. Besides proton conduction, it serves in the retention of water within the electrode, and in stabilizing the Pt catalyst against agglomeration and Ostwald ripening.

1.9. Membrane-Electrode-Assembly (MEA) Preparation

In general, MEA can be assembled by two approaches. The 1st approach consists of applying the catalyst layer onto the gas diffusion layer (GDL) forming the gas diffusion

electrode (GDE). Afterwards, the Nafion® membrane is added on the GDE for the full MEA. The 2nd approach consists of applying the electrode material directly on the membrane resulting in a catalyst-coated membrane (CCM). This is followed by the addition of the GDL for the full MEA fabrication (Figure 7).

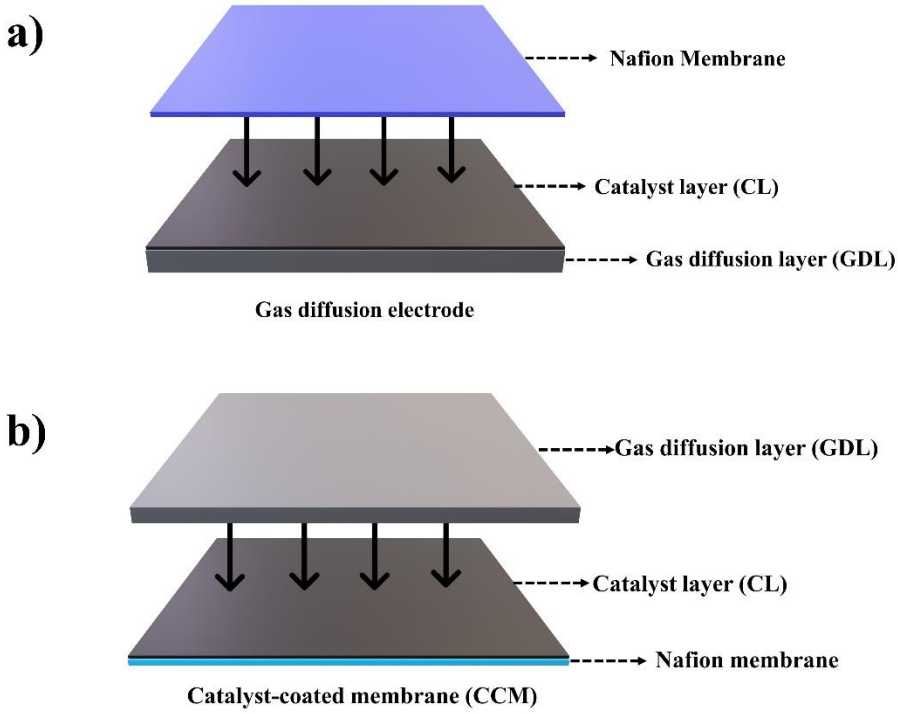

Figure 7: MEA modes of fabrication

1.9.1. Electrode Fabrication

Several fabrication techniques were suggested and performed to promote the MEA performance and durability. Techniques like spreading, spraying, decaling, impregnation, evaporation, and deposition all had their advantages and drawbacks on the efficiency of the electrode.

- Spreading: includes the preparation of a Pt/C and PTFE dough. This is followed by pressing the dough using a stainless-steel plate on top a carbon GDL resulting in a catalyst

layer of controllable thickness. The Pt loading can be estimated through measuring the thickness of the catalyst layer [26].

- Spraying: a solution of Pt/C, PTFE, and an alcoholic solvent is prepared. The solution is then sprayed repeatedly on top of carbon GDL. The GDL is dried after each spraying round [26].
- Catalyst Powder deposition: Vulcan XC-72, Pt/C and PTFE are blended in a knife mill under high milling speed followed by its application onto a carbon cloth. A PTFE/carbon layer can be applied to eliminate the roughness of the electrode [27].
- Electro-deposition: In the electro-deposition technique, a mixture of ionomer and cationic Pt complex is prepared and then deposited onto a carbon support [28].
- Impregnation reduction: The membrane is ion exchanged with Na^+ followed by an equilibration process against a Pt solution ($(NH_3)_4PtCl_2$) using a methanol/water mixture as solvent. This is followed by the exposure of one side the membrane with $NaBH_4$ reducing agent resulting in the reduction of Pt [29].
- Evaporative deposition: onto a membrane a $(NH_3)_4PtCl_3$ solution is deposited through evaporation. The membrane is dipped into a $NaBH_4$ solution for Pt reduction. This method is used to obtain low Pt loaded membranes (< 0.1 mg.cm^{-2}) [30].
- Dry spraying: using a knife mill, a solid solution of Pt/C, PTFE, PFSA (or a filler material) is prepared. Then, onto a membrane, the solution is sprayed (after being atomized) using a nitrogen purged nozzle [31].
- Catalyst decaling: an ink is prepared containing Pt/C and protonated PFSA. The ink is then applied by means of painting onto a PFSA plate. The PFSA plate is hot-pressed with the membrane. After hot-pressing, the PFSA layer is peeled leaving behind a thin catalyst layer on the membrane. The newly prepared membrane is then dehydrated and protonated though immersing it in a boiling sulfuric acid solution [32, 33].
- Painting: A Pt/C/PFSA ink is prepared similar as in the decaling method. However, the ink is directly painted onto the membrane. After drying, the pained membranes are dehydrated and protonated through immersing them in hot sulfuric acid solution [34].

The performance of MEA relies on a number of parameters that can be controlled through selecting and optimizing the mode of MEA fabrication. This stems from the fact that

ORR mainly takes place at the triple phase boundary between Pt, the incoming Oxygen, and the ionomer.

1.10. Electrode Performance

The PEMFC MEA performance depends on a combinatory effect of several parameters. Those parameters primarily affect three phenomena occurring within the MEA which are the ORR, the mass transfer, the cross over resistance, and the interfacial compatibility between the different MEA components. Therefore, MEA components are tailored to go in line with enhancing any of the mentioned processes.

Operational Polarization effect: PEMFC bridges the conversion of chemical energy to generate electrical work. Ideally, the process happens with a change of 237.1 $kJ.mol^{-1}$ in Gibbs free energy (available as electrical work), and a 285.8 $kJ.mol^{-1}$ change in enthalpy (as heat energy) at 298 K temperature and 1 atm pressure . Therefore, the ideal thermal efficiency of a fuel cell operating under H_2/O_2 feeds can be calculated through the following:

$$\eta_{ideal} = \frac{\Delta G_{idael}}{\Delta H_{ideal}} = \frac{237.1}{258.8} = 0.83 \quad (1.4)$$

However, the actual cells efficiency can be calculated through:

$$\eta = \frac{0.83\, V_{actual}}{E_{ideal}} \quad (1.5)$$

Here, the actual voltage (V_{actual}) is lower than the ideal potential $E_{ideal.}$ That is due to the polarization losses experienced during operation of the cell. These polarizations are mainly regarded as kinetic, ohmic, and concentration polarizations. The actual voltage of the cell can be depicted using the proceding equation:

$$E = E_{OCV} - E_{iR} - E_a - E_c = E^o - E_l - E_k - E_M - E_{diff} \quad (1.6)$$

E_{OCV} is the potential at the open circuit voltage (OCV) which is usually lower than the standard voltage (E^o=1.25V) due to fuel leakage (E_l). E_{iR} represents the ohmic voltage

losses which are mainly due to proton conduction. Although both the electrode and the membrane contain a proton conducting moiety (Nafion®), the majority of the ohmic losses originate from the membrane. Therefore, ohmic losses caused in the electrode is neglected, ohmic losses is represented for the membrane as E_M. E_a and E_c represent the kinetic losses occurring within the catalyst layer on both electrodes. They are combined as E_k representing the kinetic losses caused by the slow steps occurring on either electrode. Finally, E_{diff} represents the resistance impeding the transport of matter into and out of the electrochemical active centers [35].

The catalyst surface area: Since the ORR is a surface phenomenon, the available catalyst surface is one of its most critical factors that alters its kinetics. The available surface area is denoted as the electrochemical surface area (ECSA). It is a measurement expressing the catalyst's accessible surface area in meter squared (m^2) normalized to the total mass of the loaded Pt.

Ionomer type and content with the catalyst layer: The ionomer type and content can affect several processes occurring within the catalyst layer. That is, through applying the variations, the catalytic activity, the gas diffusivity, and the ionic conductivity vary simultaneously. Therefore, the ionomer content within the electrode can impose drastic change in the performance of the electrode. This is because, the proton conducting ionomer serves in the development of triple phase boundaries (TPB) on which the majority of reactions occur [13, 36].

Operating conditions: The nature of the feeding gas and its feeding rate in addition to the PEMFC operating conditions (temperature, humidity, and pressure) can have a huge effect on its performance. Generally, cells perform better under higher temperatures. That is because higher temperature accelerates proton conduction and mass diffusion. This in turn alleviates both the ohmic and the mass transfer resistances, both resulting in an overall enhancement in the MEA performance. Also, higher humidity operational levels are favored for better performance. Proton conduction especially heavily relies on the availability of water. Similarly, high pressure enhances the gas diffusion throughout the electrode resulting in better catalyst accessibility [37].

1.11. Catalyst Layer Durability

Much attention was given to the durability of the MEA during operation. However, several durability concerns have risen questioning the feasibility of PEMFCs usage in various applications. Often, the expected lifetime for PEMFCs is 5000 hours for automotive applications and up till 40000 hours for stationary applications [38]. Therefore, the catalyst layer's stability is of importance for extended lifetime of PEMFC. For that reason, understanding the mechanism behind the decline in performance over time enables the researchers to tackle the problems and enhance the PEMFC durability. Within the Pt/C catalyst, changes might occur to both Pt and the carbon support components.

1.11.1. Pt Durability

Loss of Pt represents one of the most common forms causing the decline of the MEA performance over time. During operation, the MEA is subjected to a harsh medium condition of low pH and the excessive abundance of oxygen gas. Therefore, under certain applied voltage, Pt active surface area loss occurs over numerous cycles. This results in a decline in the overall performance of the MEA. However, Pt surface area loss occurs through a number of mechanisms, dissolution, agglomeration, and Ostwald ripening.

1.11.1.1. Pt Dissolution and Ostwald Ripening

In acidic medium and under certain voltage loa, Pt can be dissolute to form Pt^{2+} and Pt^{4+} ions. This results in the loss of Pt activity and the ECSA resulting in an overall drop in performance. Generally, Pt-dissolution is accelerated in an electrode within a voltage window of 0.85-0.95V according to the following reaction:

$$Pt \rightarrow Pt^{2+} + 2e^{-} \quad E^{0} = 1.118\ vs\ RHE \tag{1.7}$$

It is worthy to note that not Pt^{2+} ions are formed during the dissolution process, but Pt^{4+} are also produced. The dissolved ions can migrate towards the negative electrode (anode). However, they can replace H^+ ions within the membrane causing Pt-ion deposition yielding an increase in the proton conduction resistance. The dissolved Pt-ions can also deposit on other Pt particles forming larger particles. This phenomenon is an example of Ostwald ripening which can result in a decline in the ECSA, finally leading to a deterioration in the MEA performance. It was noticed that increasing the hydration level within the MEA as well as the applied voltage accelerates Pt dissolution. This in turn facilitates the kinetics of Ostwald ripening and particles growth [39, 40].

1.11.1.2. Particle Migration and Detachment

Particle migration stems from the movement of Pt particles on the carbon support where they agglomerate upon meeting leading to particle growth and a drop in ECSA. On the other hand, particle detachment from the carbon support often happens in parallel with carbon corrosion. Similarly, this entails a drop in ECSA to an extent mainly based on the interaction between the Pt particle and the carbon support, the graphitization degree within the carbon support. However, since carbon corrosion is negligible at low applied voltages, particle detachment is prominent at voltages above 1.1V [39, 40].

1.11.2. Carbon Corrosion

Generally, noble metal catalysts are supported on high surface area carbon supports. The graphitized carbon support provides electrical conduction, and stability to the noble metal anchored to its surface. Therefore, the degradation occurring in the carbon support serves in decreasing the ECSA leading to an overall downfall in MEA performance. Furthermore, it increases the hydrophilicity in the MEA resulting in an effect on the overall performance. Also, carbon corrosion accompanies a change in the thickness of the electrode

which imposes a change in the ohmic resistance [41].Thermodynamically, Carbon corrosion occurs through the oxidation of carbon according to the following reaction[42]:

$$C + H_2O \rightarrow CO_2 + 4H^+ + 4e^- \qquad E^0 = -2.07\,V\ vs\ RHE \qquad (1.8)$$

Within PEMFCs operating condition, carbon corrosion occurs at voltages above 1.1V vs RHE. Furthermore, as equation 2.8 suggests, carbon corrosion accelerates in the presence in humidified conditions. Therefore, feeding the cell with humidified air results in a more severe carbon oxidation [39].

1.12. Electrospinning

1.12.1. Principle of Electrospinning

Electrospinning is a process involving electrohydrodynamic in which an electric field is applied onto a liquid droplet causing it to form a jet leading to the elongation of the viscous droplet to form a fiber. The components of this facile process include a high voltage power supply, a bluntly cut stainless-steel needle, a syringe pump, and an electrically conductive fiber collector (Figure 8).

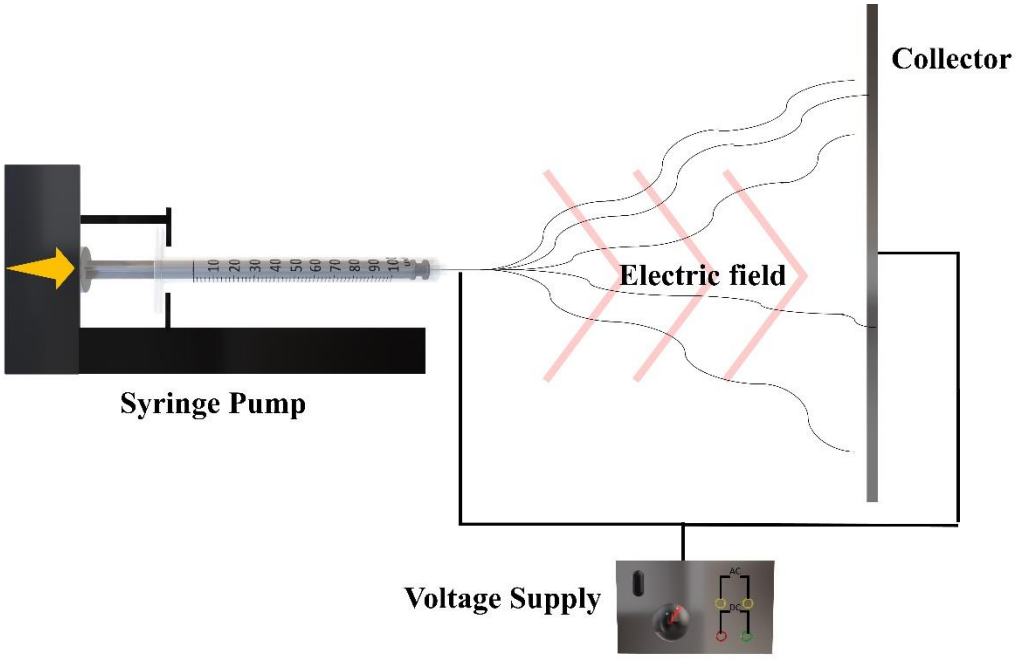

Figure 8: Schematic describing the electrospinning setup and principle

In detail, upon applying voltage onto the incoming ink through the metallic needle, instability occurs within. Therefore, the polymer flows in the direction of the electric field formed. Eventually, as an effect of the rising electrical field, a droplet forms at the tip of the needle which forms a conical shape called the "Tailor cone". From the tailor cone fibers emerge, stretches, and dry while being collected on the grounded collector [43].

1.12.2. Electrospinning Parameters

Obtaining fibers with a desired morphology through electrospinning heavily relies on several parameters. Those parameters can be classified into solution and electrospinning parameters. Solution parameters include concentration of the polymer solution and the overall viscosity of the ink, ink conductivity, and solvent nature and characteristics. On the other hand, electrospinning parameters within the electrospinning chamber include the applied voltage, relative humidity, and ink flowrate

1.12.2.1. Applied Voltage

The critical voltage applied onto the needle required to form the tailor cone varies from one polymer to another. However, upon increasing the applied voltage, the charges within the polymer repel causing a further stretching in the polymer jet. This issues the formation of fibers with smaller diameter. On the other hand, if the applied voltage increases surpassing a certain limit, it results in narrowing the tailor cone and thus the formation of beads in the fiber mat [44].

1.12.2.2. Flow rate

The produced fibers' morphology can be controlled through adjusting the flow rate of the electrospinning ink in the metallic needle. Optimizing the flow rate during the process results in the formation of continuous fibers free of beads. Increasing the flow rate gives rise to the formation of porous, and high diameter fibers. However, in parallel, beads can be formed due to the insufficient drying of the fibers before collection. Therefore, once obtaining the desired pore and fiber diameter, it is advised to maintain a low flow rate to avoid the formation of beads. Furthermore, it ensures the formation of a continuous jet necessary for neat fiber formation [45].

1.12.2.3. Relative Humidity and Temperature

In parallel with the chemical nature of the electrospinning ink components, the humidity conditions maintained within the electrospinning chamber can cause a change in the diameter of the obtained fibers. That is because varying the humidity level can affect the solidification of the fiber during its flying time. On the other hand, temperature has a double effect on the electrospinning ink. On one hand, elevated temperatures cause a faster solvent evaporation. While at the same time, they affect the viscosity of the ink. Both mechanisms ensue the formation of fibers with finer diameters [46].

1.12.3. Solution Parameters

1.12.3.1. Polymer Concentration and Ink Viscosity

Since electrospinning is basically a process of extension of a polarized jet, the concentration of polymer within the ink plays an important role. Electrospinning an ink with low polymer content, the applied voltage causes the early fragmentation of the fiber due to low polymer entanglements. Thereby, fragmentation proceeds the formation of beads within the fiber. However, increasing the polymer concentration enhances entanglements within the polymer chains leading to increasing the viscosity of the solution. The entangled polymer chains can withstand the surface tension imposed by the applied voltage delaying fragmentation and resulting in formation of fiber on the collector surface. However, excessive increase in the polymer concentration within the ink results in over viscosity altering the solution flow through the needle and early drying of the fibers. This can emanate the formation of beads or truncated fibers [47, 48].

1.12.3.2. Ink Conductivity

The electrospinning concept relies on the coulombic interaction between the charges at the surface of the fluid ink and the electrostatic force generated by the applied voltage. This interaction leads to the deformation of the ink droplet to establish the tailor cone. Therefore, solutions with low conductivity will not have enough charges to interact with the imposed force to form the tailor cone ultimately resulting in no fiber formation. On the other hand, increasing the conductivity will favor the formation of the Taylor cone, and causes the formation of finer fibers. The conductivity of the ink can be controlled through using conductive polymers, or the addition of salts. The latter increases the charge density (ions) at the surface of the fluid. Therefore, the solution becomes more responsive to the applied electrical force [49].

1.12.3.3. The Solvent

The selection of the appropriate solvent for the electrospinning process is considered as one of the most important steps. 1st, the solvent is required to accommodate the polymer. In other words, the polymer is required to be completely soluble within the selected solvent.2nd, the solvent needs to be of moderate boiling point. The fast evaporation of volatile solvents can cause the solution to dry and solid accumulation at the tip of the needle resulting in its blockage. On the other hand, the slow evaporation of solvents of high boiling point results in bead formation due to the collection of the fibers in their wet state. Therefore, using solvents of moderate boiling points is recommended for electrospinning. In addition, the suitable selection of the solvent system can have a significant effect on the morphology of the obtained fibers. For instance, using a dual solvent system consisting of main solvents and a volatile sacrificial solvent can result in the formation of fibers with controlled porosity. That is, the sacrificial solvent is generally a volatile solvent that can evaporate faster than the main solvent. This result in phase separation during electrospinning and thus the formation of voids [44, 50].

1.12.4. Electrospun PEMFC Electrodes

Electrospinning has been proven to be facile and an important method in fabricating a self-standing, and highly active electrodes for PEMFCs. Electrospinning and ink parameters can be varied to obtain the desired fiber morphology. For those reasons, electrospinning has been used frequently in recent days to fabricate high-performing electrodes with low catalyst loadings. Kotera et al was the first to suggest the usage of spun fibers for PEMFC electrodes. In the study, fiber-based cathodes were fabricated using electrospinning with optimal ionic and electronic conductivity. Using Polyethylene oxide (PEO) as a carrier polymer with 42 % wt Pt alloy and 28% Flemion ionomer, fibrous mats were obtained in a double and triple nozzle co-axial electrospinning. Upon comparing the fibrous electrodes with conventionally sprayed electrodes, the former has shown a 10 times

greater gas permeability. This can be attributed to both the inter and intra-fiber pores within the fiber mats enabling the passage of gases. Furthermore, upon assembling an MEA with the fibrous cathode and comparing them to MEA containing sprayed cathodes, the latter showed an obvious decline in the mass transfer losses. This can be correlated with the high gas permeability exhibited by the fibrous electrodes. As a result, MEAs employing fibrous electrodes recorded a 445 $mW.cm^{-2}$ maximum power density compared to 350 $mW.cm^{-2}$ for that of slurry based electrode containing MEA at testing conditions of fully humidified H_2/air feed, 95ºC, and 150 kPa back pressure [51]. Kotera's work was followed by several detailed studies conducted by Pintauro's research group about electrospun fibrous electrodes. In his 1st study, nanofiber mats containing 40% Pt/C, Nafion®, and polyacrylic acid (PAA) as carrier polymer were fabricated using electrospinning. The resulting nanofibers of 470 nm average diameter appeared to have a rough surface due to the alignment Pt/C particles on the PAA fibers. This uniform alignment ensures continuous proton and electron conductivity throughout the fiber. This In turn serves in enhancing the Pt utilization and the useful electrochemical surface area. MEAs were prepared with a cathode Pt loading of 0.1,0.2 and 0.4 $mg.cm^{-2}$ against a decal anode of 0.4 $mg.cm^{-2}$ loading and were compared to a 0.4 $mg.cm^{-2}$ symmetrical decal electrode containing MEA. The polarization curve showed that even the 0.1 $mg.cm^{-2}$ electrospun electrode performed slightly better (0.873 $A.cm^{-2}$) compared to the control MEA (0.524 $A.cm^{-2}$) at 0.6 V. In parallel, the electrochemical surface area recorded for fiber-based electrodes was 114 $m^2.g^{-1}_{pt}$ compared to only 60 $m^2.g^{-1}_{pt}$ for the decal electrode. This demonstrates the superiority of the fibrous architecture in increasing the Pt utilization, and therefore maintain a significant power output while decreasing the Pt loading by 4 folds. This can be related to the better interfacial and mass transfer resistance shown by the fibrous electrode. Furthermore, the durability of the decal cathode suffered a 75 % loss in its ECSA upon cycling it between 0.6 and 1.2 V in H_2/N_2 atmosphere and 80ºC. on the other hand, the fiber-based (0.4 $mg.cm^{-2}$) cathode lost only 46.4% of its initial ECSA after 1200 cycles [52]. In a similar study, ultralow Pt loaded Pt/C/Nafion® fibrous electrodes with PAA as carrier polymer was investigated and compared to decal-based electrodes. The results showed that electropun electrodes showed better ECSA and Pt utilization compared to the decal electrode. This is due to the better Pt distribution and exposure within the fibrous architecture. This resulted in a highly efficient fibrous electrode with 0.065 $mg.cm^{-2}$ Pt

surpassing that of 0.104 mg.cm^{-2} Pt loaded decal electrode. The results have also suggested that fiber-based electrodes with lower Pt-loading (i.e: thinner mats) exhibit better Pt utilization. This can be related to the reduced O_2 pathways, and ohmic resistances exhibited by thinner mats [53]. Unlike conventional electrodes [13], fiber-based electrodes were not affected by varying the Pt/Nafion® content. Furthermore, their performance was found independent of the fiber diameter. On the other hand, increasing the PAA content in the fiber was found to have a negative effect on the overall performance. It was thought that PAA impedes the conduction of protons through Nafion® resulting in an overall halt in the MEA performance [54, 55]. This was further investigated by Neyerlin where he found that increasing the PAA content result in the isolation of Pt particles in the interior of the fiber [56]. However, the hydrophilic nature of PAA in a fibrous array enabled the electrode to withstand dry operating conditions. It was reported that fibrous electrodes containing PAA recorded a power output double of that of painted electrodes [57] . Similar to the previous studies, the fiber-based electrodes exhibited low to no performance loss after Pt-dissolution AST, and less severe loss after C-corrosion AST. Upon comparing the fibrous electrodes and sprayed electrodes, the fibrous structure of the former enhances the water expulsion from the electrode preventing water flooding. On the other hand, sprayed electrodes show electrode thinning accompanied by pore blockage resulting in probable water flooding and electrochemical processes disruption [58-60].

Despite the impressive Pt-dissolution durability shown by the aforementioned electrodes, the results showed that they suffered from severe carbon corrosion. The extreme conditions within the MEA such as low pH and oxidizing mediums serve in deteriorating the electrode. However, it was found that excess water has a notceable impact on the corrosion of the carbon support. This was evident upon performing the carbon corrosion AST for fibrous Pt/C/Nafion®/PAA electrode in dry operating conditions (40% RH).it has been shown that the electrode has experienced lower carbon corrosion in dry conditions marking the role of water in accelerating the process [55]. For that reason, Pt/Nafion® fibers were fabricated using electrospinning but via Polyvinylidene (PVDF) hydrophobic carrier polymer [61].However, PVDF suffers from low proton conductivity and oxygen permeability [62]. Nevertheless, its low wettability can be utilized in the expulsion of water and designing a carbon corrosion tolerant electrode. On the performance level, fibrous Pt/C/Nafion®/PVDF-

based electrodes have surpassed that of Pt/C/Nafion®/PAA-based electrodes at low voltages lying in the mass transfer region. This can be correlated with the better water expulsion provoked by the increasing hydrophobic medium in the PVDF employing electrode. Conversely, the later electrode reigned superior at high voltages lying in the kinetic region suggesting better ORR kinetics due to the abundance of water. As a result, Pt/C/Nafion®/PVDF-based electrodes recorded a maximum power density of 545 $mW.cm^{-2}$, 13% higher than that of the PAA employing electrode. Pt/C/Nafion®/PVDF-based electrodes showed a promising carbon corrosion tolerance, especially for high PVDF containing electrodes. This is attributed to the favorable hydrophilic domain growth associated with carbon corrosion leading to a rise in performance. In addition, through visualizing the electrodes before and after carbon corrosion AST, it was found that PVDF helps stabilize the porous architecture of the electrode. Thus, a retention in the overall electrode thickness during operation. Thereby, resulting in minimal decline in the power output of the MEA [63]. Therefore, generally, fibrous electrodes have shown lower loss than the conventional electrodes. However, it was reported that electrodes recording the highest power density suffered the highest power loss after durability cycling [64].

The performance and durability of Pt-alloy catalysts and Pt-free catalysts in a fibrous architecture have been investigated. Nanofiber-based PtCo/C/Nafion® was fabricated using electrospinning using PAA as carrier polymer with a 0.1 $mg.cm^{-2}$ catalyst loading. The electrodes were tested in a H_2/O_2 fully humidified environment and under 80°C temperature and 200 kPa backpressure. Again, the results showed the superiority of electrospun fibrous electrode over conventional painted electrodes. MEAs containing Fibrous PtCo/C/Nafion® cathodes recorded 1045 $mW.cm^{-2}$ maximum power density against 869 $mW.cm^{-2}$ for the PtCo/C/Nafion® painted electrode containing MEAs. Like the previous results, the Nanofiber electrode lost only 8% of its initial performance after Pt-dissolution AST compared to 32% loss for that of the painted electrode. This was again attributed to both the inter and intra-fiber porosities both exhibited by the fibrous architecture serving in better mass transfer [65]. In another study, a non-Pt group metal (PGM) MOF-derived Fe-N-C catalyst was electrospun with Nafion® ionomer and PVDF carrier polymer. The as prepared electrode (1.5 $mg.cm^{-2}$ Pt loading) was incorporated into a MEA and compared with a sprayed electrode at 80°C, H_2/air fully humidified feed, and 1 atm backpressure. The nanofiber-based electrode recorded 150

$mW.cm^{-2}$ maximum power density. Furthermore, it showed a 20.7% increase in maximum power density after 50 carbon corrosion AST cycles followed 43% loss after 500 cycles [66]. In another study, Pd/C was electrospun then a Pt skin was pulse deposited on the Pd surface to form a self-standing fibrous electrode with 19 $\mu g.cm^{-2}$ Pt loading. The electrode delivered a maximum power density of 620 $mW.cm^{-2}$ in H_2/air feeding medium. The recorded power density was 5 folds higher than that of the conventional electrode. The high-power density can be attributed to the synergetic effect between Pd core and Pt skin. Furthermore, the even distribution of catalyst and Nafion® particles throughout the fiber enhanced the formation of TPB resulting in enhanced performance. Also, The synergistic effect between Pd and Pt, and PAA carrier polymer and the carbon support stabilized the electrode resulting in a 4.8 drop in performance after 30000 AST cycles [67].

1.13. Cerium Oxide (CeO_2) Additive in PEMFCs

1.13.1. CeO_2 Characteristics

Cerium oxide (Ceria: CeO_2) is gaining a lot of fame in numerous applications due to its remarkable catalytic activity. CeO adopts the fluorite crystal structure consisting of a face centered cubic unit cell where the cations occupy the FCC positions while the anions are in tetrahedral sites. Therefore, each cerium ion is joined via coordination bonds to eight oxygen anions which are in turn coordinated with another four cerium cations [68]. CeO_2 is characterized by its accommodation of high oxygen vacancies which results in high oxygen conductivities. Those oxygen vacancies play a crucial role in the activity of CeO_2 where the boosted catalytic activity is termed as the oxygen storage capacity (OSC). The change in the oxidation state majorly controls the OSC of CeO_2. That is, the close energy levels of 4f and 5d orbitals within the electronic structure of CeO_2 results in a minimal energy barrier for oxidation/reduction possibility of the cerium ion. As a result, CeO_2 is generally composed by a combination between the Ce^{3+} and Ce^{4+} ions. The decline in the oxygen content of CeO_2 results in the formation of oxygen vacancies. In this state, the cerium ions are reduced into the Ce^{3+} state to achieve electroneutrality [69-72]. This results in the increase in the $Ce^{3+}/(Ce^{3+}+Ce^{4+})$ ratio. This leads CeO_2 to become an excellent oxygen buffer. The formation of

oxygen vacancies within CeO_2 is dynamic and can be triggered by several conditions mainly the temperature and the partial pressure of oxygen [73, 74].

The density of oxygen defects in CeO_2 can be controlled through controlling its particle size. That's because upon changing the particle size, the grain boundaries increase dramatically [75], increase the surface area of interaction. Furthermore, it is thought that lowering the particle size results in the decrease of energy required to obtain oxygen vacancies [71]. This in turn results in the dramatic increase in the particle reactivity even at low temperature [76]. With that being said. nano-CeO_2 usage surged in several applications due to their remarkable catalytic and physical features they possess. Furthermore, it was found that densifying specific crystal planes within the CeO_2 particle promotes a particular catalytic activity. For instance, introducing the serve in increasing the reactivity of CeO_2 towards the oxidation of carbon monoxide. That is because, certain planes are characterized by a lower activation energy to generate the oxygen vacancies and thereby increase its reactivity [77, 78].

1.13.2. The Use of CeO_2 in PEMFC Electrodes

Due to the oxygen storing advantage exhibited by CeO_2, attempts were made to enhance the Pt catalyst kinetics at the cathode favoring a boosted overall performance. In this regard, Pt and CeO_2 nanoparticles were evenly impregnated on top of a carbon support via a hydrothermal process followed by a sodium borohydride-based reduction. The as synthesized catalyst was tested both using ex-situ and in-situ analysis and compared to conventional Pt/C catalyst. The ex-situ analysis was done through linear sweep voltammetry where the ORR activity was evaluated. The results show that Pt-CeO_2/C catalysts showed a half wave potential of 0.78V higher than that of Pt/C (0.73V) entailing better ORR activity. This was correlated with the lower overpotentials exhibited by Pt-CeO_2/C containing cathodes in the MEA in-situ testing. The better ORR activity and performance are attributed to the oxygen storage ability of CeO_2 serving in increasing the oxygen concentration [79]. In another study, it was suggested that the electronic interaction between Pt and CeO_2 decreases the electron

density on the surface of the Pt. Thereby, it enhances the ORR kinetics. It was also suggested that oxygen was stored in the form of oxide in the CeO_2 lattice, and the ORR occurred at the TPB between Pt-CeO_2/C, O^{2-}, and protons diffusing from the anode [80]. In another study, Pt-CeO_x/C and PtCo-CeO_x/C were synthesized using a colloidal method. X-ray photoelectron spectroscopy (XPS) characterization has shown that CeO_x is composed of a CeO_2 shell while Ce_2O_3 resides in the core of the particle. This feature has shown an impressive oxygen exchange ability within. Therefore, the catalyst layer exhibited an enhanced ORR kinetics compared to Pt/C catalyst. Furthermore, The I-V curve of the MEAs containing PtCo-CeO_x/C and Pt-CeO_x/C at the cathode have shown an overall higher voltages for all current densities compared to Pt/C containing MEAs [81]. Similar results were reported by Lim et al. He stated that in order for CeO_2 to enhance the ORR kinetics at the surface of Pt, there needs to be a broad interface between both. This can be promoted through the usage of particles of small size and good distribution throughout the electrode. There at the interface, CeO_2 releases the stored oxygen to the neighboring Pt followed by its reduction to Ce_2O_3. After the change in the local oxygen concentration Ce_2O_3 oxidizes back to CeO_2 (Figure 9). Therefore, the oxidation/reduction reactions happening between Ce^{3+} and Ce^{4+} constitutes the origin of the oxygen buffering feature exhibited by CeO_2 according to the following reaction [82]:

$$CeO_2 \leftrightarrow CeO_{2-x} + \frac{x}{2}O_2 \ (0 \ \leq x \ \leq 0.5) \tag{1.9}$$

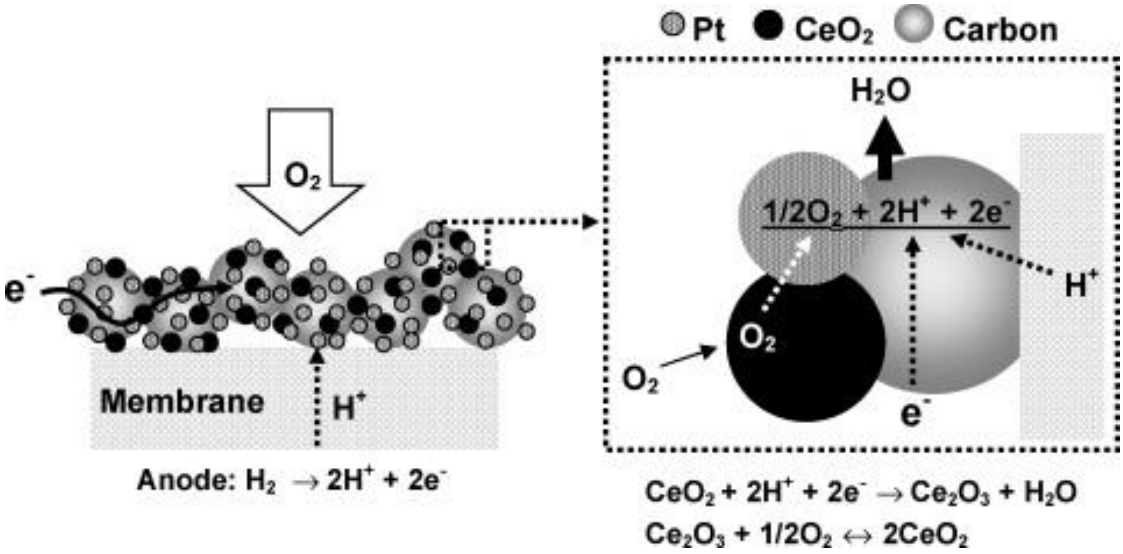

Figure 9: Proposed mechanism for the buffering effect of CeO_2 in PEMFC cathode [83]

The durability of the Pt-CeO_2/C catalyst was evaluated through cycling between 0 and 1.2V in sulfuric acid and comparing it with the conventional Pt/C catalyst. Evaluation was done through obtaining the ECSA after 1000 cycles. The results obtained show a remarkable retention in the ECSA for Pt-CeO_2/C (11.9% loss) compared to a fast decline in Pt/C ECSA (33.3% loss). This can be attributed to the stabilizing effect of CeO_2 limiting Pt dissolution and agglomeration and carbon oxidation. Similar results were obtained upon comparing the ORR activities after cycling. Pt/C showed an anodic shift at $E_{1/2}$ of 72 mV which is due to the decline in the Pt surface area compared to a minimal shift of 20 mV for Pt-CeO_2/C. The transmission electron microscopy (TEM) images before and after cycling have a shown a minimal Pt particle growth in Pt-CeO_2/C electrodes compared to Pt/C assuring that the cause of performance decline is the agglomeration of Pt particles [83]. In another study, Pt-CeO_x/C was prepared via a hot precipitation and impregnation method. However, upon conditioning the catalyst with 0.1 M H_2SO_4, it was realized that much of the CeO_x has dissolved in the solution. Furthermore, the remaining amount was observed to form a thin Ce_2O_3 film on the surface of Pt. Compared to the conventional Pt/C electrode, the amorphous Ce_2O_3 coated Pt/C-based electrode has shown an enhanced ORR activity. Furthermore, it was found that the amorphous layer alters Pt oxidation and dissolution serving in further enhancing its performance and durability [84]. Furthermore, CeO_2 and doped CeO_2 additives were to have a MEA life prolonging effect through depressing catalyst corrosion. That is, CeO_2 is known to be a radical scavenger. Therefore, upon scavenging the radical produced during PEMFC process, it stabilizes the catalyst layer extending its lifetime [85]. On the other hand, this radical scavenging activity of CeO_2 serves in prolonging the membranes lifetime and suppressing its early degradation [86]. Furthermore, cubic CeO_2/Graphene oxide nanocomposite was prepared through microwave assisted polyol synthesis and used in an electrode to scavenge the radical attack on the different components of the MEA. The results have shown that an 8% addition of the composite served in expanding the ECSA. Furthermore, it helped the MEA retain 69% of its catalytic performance after 5000 cycles within a 0.8-1.23 V window [87].

CHAPTER 2: CHARACTERIZATION METHODS

This chapter is dedicated to briefly introducing the operating principles for the characterization tools used during the study. First, the material characterization is described followed by the electrochemical characterization.

2.1. Material Characterization Methods

2.1.1. Field Emission Scanning Electron Microscopy (FE-SEM)

FE-SEM is used for the visualization of the surface morphology of a material. The operating principle behind this phenomenon is the conversion of electron beams into narrow areas using electromagnetic lenses. The interaction between matter and the focused beam can result in a number of outcomes which can be used in order to have a deeper insight on the scanned surface. The incident beam of sufficient energy interacts with a valence electron at the outer shell of the atom. The interaction can result in knocking out an accelerated electron with a definite energy which is collected by a collector. The electrons collected through this process are called the secondary electrons. Secondary electrons are characterized to have a relatively low energy. Therefore, only electrons emitted from the surface are of energy sufficient to be collected by the secondary electron detector. Therefore, visualizing using secondary electrons majorly reveals the surface morphology and texture. Besides secondary electrons, back scattered electrons are used to identify the composing elements within the

sample. The backscattered electrons are the scattered electrons formed upon the elastic reflection of electrons. The extent of reflection from the sample depends on the electronic structure of the atoms present. Heavier elements entail a larger number of electrons in their electronic shells. Therefore, more electrons will scatter from such elements. This phenomenon results in a contrast between the different elements present regarded as the Z-contrast. In other words, heavier elements (high Z value) will scatter more electrons and thus will appear as brighter spots. In contrast, lighter elements (low Z value) will scatter less electrons and thus will appear darker [88].

As mentioned earlier, an incident electron can detach an electron from the valence shell of an atom. However, in parallel, electrons from the inner shells can be excited by the incoming electrons resulting in their detachment. The detachment of inner electrons results in the relaxation of an electron from the valence shell and the release of x-ray. Since the electronic structure of each element characterizes it, the emitted x-ray is characteristic of each element. From here, energy dispersive spectroscopy is used in order to identify elements within a scanned area [88].

In this dissertation, SEM images were obtained using Zeiss LEO-Supra 35 VP FE-SEM. Using the secondary electron mode, topological images were obtained to visualize the morphology of the scanned samples. Therefore, the obtained images were scanned at a low bias voltage of 3-5 kV. However, the color contrast within the image can be related to the generation of a mixture of secondary and backscattered electrons.

2.1.2. Transmission Electron Microscopy (TEM)

Transmission electron microscopy is a vital tool to visualize material at a tiny scale. Within, the sample is bombarded by an electron beam of 150-200 keV. The high energy of the beam enables it to transmit through the sample. From there, the instrument gained the name of “Transmission electron microscopy”. As the high energy beam moves through the sample, it gets scattered upon an electronic interaction with the atoms within the sample. Based on the thickness of the sample, and more importantly the atomic mass of the sample atoms, the incident beam scatters proportionally. After adjustments, the scattered electrons

can form an image on the final screen visualizing the particles at a nano-meter scale. The generated image is attributed by both mass contrast due to the existing atoms, and dimensional contrast controlled by the thickness of the sample. Furthermore, the generated x-rays due to the interaction between the incident electrons and the electrons can be collected through a x-ray detector for energy dispersion x-ray studies and mapping. The high energy of the electron beams utilized in TEM enables the generation of both high-resolution images and EDS mappings [89].

In the current dissertation, TEM was used to visualize electrospun fibers and the nano-rod CeO_2 at nanoscale. The images enable the investigation of the intra-fibrous porosities. Furthermore, they allow a precise measurement of the average fiber diameter. Finally, TEM-EDS was performed in order to generate a distribution image of the different particles on fibers allowing us to comment on the uniformity of particle distribution. This was performed using a STEM, JEOL JEM-ARM200CF, operated at 200 kV with a probe size of *ca.* 1 Å. While EDS was performed using JEOL Centurio system mounted on the STEM.

2.1.3. X-Ray Diffraction Spectroscopy (XRD)

The crystalline structure of the synthesized material was studied using X-ray diffraction spectroscopy. Upon exposing the sample with a certain crystallographic structure to x-rays, they scatter elastically upon interacting with the existing electrons. The result of x-ray scattering are waves which build up through constructive interference or cancel through destructive interference. Constructive interference occurs only at certain angles characteristic of a material called the Bragg angles. In other words, upon bombarding a certain crystallographic plane with a characteristic ionic structure, x-ray scatter back. Only when the resulting scattered waves are in phase, do the waves constructively interfere. This happens when the path difference crossed by the beam (AB+ AC) is equal to the wavelength ($\lambda_{x\text{-}ray}$) of the x-ray beam multiplied with an integer n (Figure 10) [90]. This relation is known as Bragg's law:

$$Path\ length\ difference = AB + AC = 2dsin\theta = n\lambda \quad (2.1)$$

As a result, a set of peaks each corresponding to the constructive interference of scattered beam from a crystallographic plane collected at a certain diffraction angle (Bragg's angle). Furthermore, the crystallite size can be estimated through tracking the broadening in the diffraction peaks. The crystallite size can be estimated using Scherrer's equation[90]:

$$L = \frac{K\lambda}{\beta cos\theta} \tag{2.2}$$

Where, L is the estimated crystallite size, K is shape factor taken as 0.89, λ is the wavelength of x-rays equal 1.54060 Å, β is the half width of the maximum of the peak, and θ is the Bragg's angle.

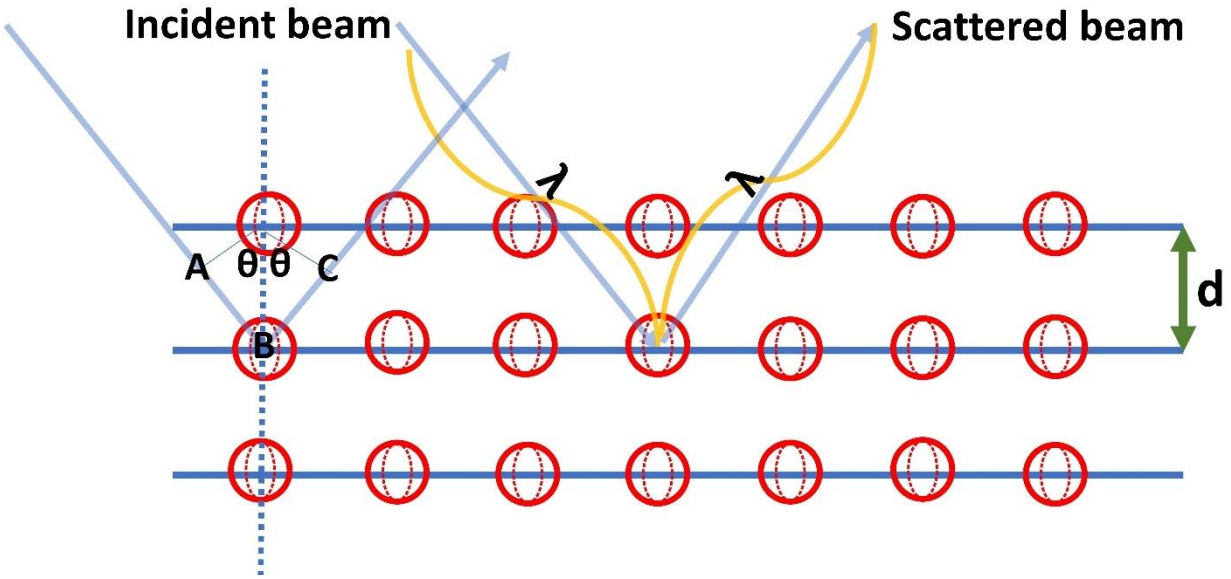

Figure 10: Scattering of X-ray off crystalline solid atomic planes

In this dissertation, X-ray diffraction spectrums were collected using Bruker D2 Phaser Diffractometer composed of a X-ray Copper radiation source and a X-ray detector. The samples were analyzed within a 2θ window of 5-90° and a step size of 0.02°/sec. The resulting spectra were analyzed using DIFFRAC.EVA from Bruker and were compared with other results obtained from the literature.

2.1.4. Specific Area Through Brunauer, Emmett and Teller (BET) Theory

The materials' surface area can be estimated through the adsorption of a gas on the entire surface. Brunauer, Emmett and Teller theory is a method which was 1st designed to estimate the monolayer coverage of adsorbed gas. This theory was later modified to study the multilayer gas adsorption on the surface of a material:

$$\frac{1}{V_a(\frac{P_0}{P}-1)} = \frac{C-1}{V_m C}\frac{P}{P_0} + \frac{1}{V_m C} \quad (2.4)$$

Where, P and P_0 represent the partial pressure and the pressure of saturation of the gas used during the measurement, Va is the room temperature volume of the gas adsorbed, V_m is the monolayer formation volume requirement of the used gas, and C is the constant representing the enthalpy of the adsorption of the gas. Equation 4.4 can be then used through plotting $\frac{1}{V_a(\frac{P_0}{P}-1)}$ vs $\frac{P}{P_0}$. The linear plot of the aforementioned factors leaves us with V_m and C which can be estimated through the slope and the y-intercept of the linear plot. From here, the surface area of the sample can be estimated [91].

In the current dissertation, BET measurements were used to estimate the surface area of the samples. Furthermore, the pore size distribution was estimated and plotted using Micromeritics, 3Flex.

2.2. Electrochemical Characterization Methods

2.2.1. Polarization Curves

Polarization curves are generally collected via two modes: the steady state mode. In the steady state mode, the cell potential is recorded as a result of varying current. In this dissertation the polarization curves were collected to evaluate the performance of the MEA. Fully or partially humidified H_2 and air were fed to the anode and the cathode, respectively. The cell was kept at 80^{o}C and under 25 psi backpressure during data collection. Prior to collection, the MEA was condition through cycling via a square voltage wave (0.2 V and 0.6V) maintained consecutively for 1 min until obtaining a stable current density (Figure 11). Conditioning was performed in H_2/air atmosphere, 80^{o}C, and without any backpressure.

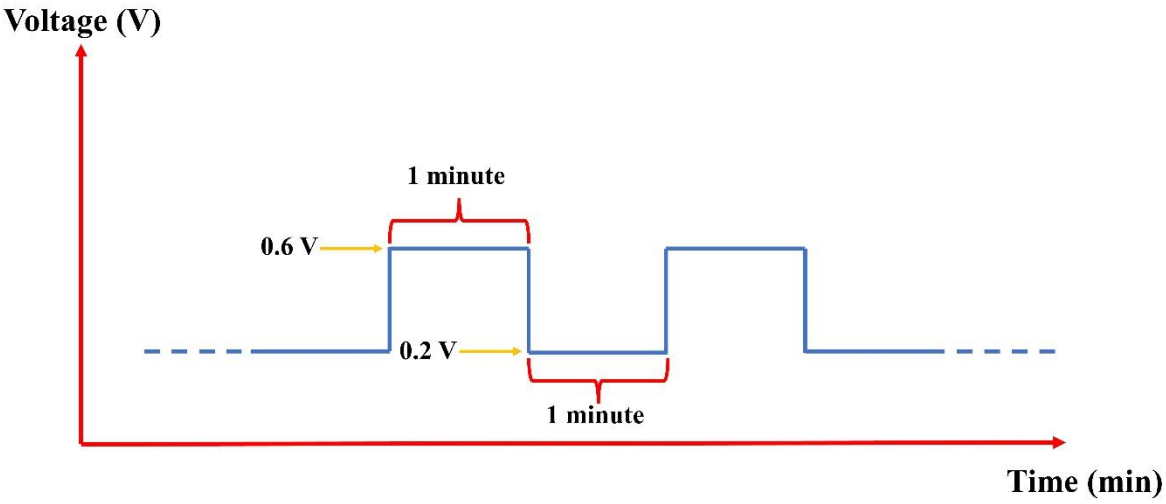

Figure 11: MEA conditioning

2.2.2. Electrochemical Impedance Spectroscopy (EIS)

\

Electrochemical impedance spectroscopy is an extremely useful tool when it comes to analyzing the different processes occurring within the MEA. For instance, EIS can provide valuable and detailed information about the charge transfer, mass transfer, electron and proton conduction within the electrode. Furthermore, with the help of other electrochemical and material characterization techniques, it can reveal the mechanisms underlying numerous phenomena. For that, EIS was considered to be a perfect candidate for several electrochemical systems such as batteries, fuel cells, and supercapacitors.

EIS is based on applying a low AC current wave onto an electrochemical system (MEA for our case) and obtaining a response from the MEA from this stimulus. The difference between the stimulus and the response can be measured as AC voltage/AC current. This difference between them is termed as the impedance of the system. Normally, the wave applied onto the system is done with various frequencies. Therefore, the impedance is measured throughout a frequency range (ex :0.1 Hz to 10000 Hz).

During PEMFC MEA operation, different electrochemical processes occur such as oxidation and reduction at the anode and cathode, respectively. Furthermore, mass transport such oxygen diffusion and proton conduction phenomena are observed. However, since the aforementioned processes each occur with a different time constant, those time constants can be transformed into frequency domains. Upon converting them into frequency domains, the different processes can each be visualized and traced using EIS. For instance, in the high frequency region, EIS measures the contact resistance at the interfaces and the resistance of the electrolyte. All of which is termed as the ohmic resistance R_e. This is followed by the measurement of the charge transfer resistance ($R_{ch,t}$) at lower frequencies. The charge transfer resistance depicts the electrochemical processes occurring within the electrodes (oxidation and/or reduction). At the lowest frequencies, the slowest processes can be tracked such mass transfer and diffusion like processes depicted by the mass transfer resistance (R_M). The EIS measurement is often represented using the Bode and the Nyquist plots (Figure 12). Since

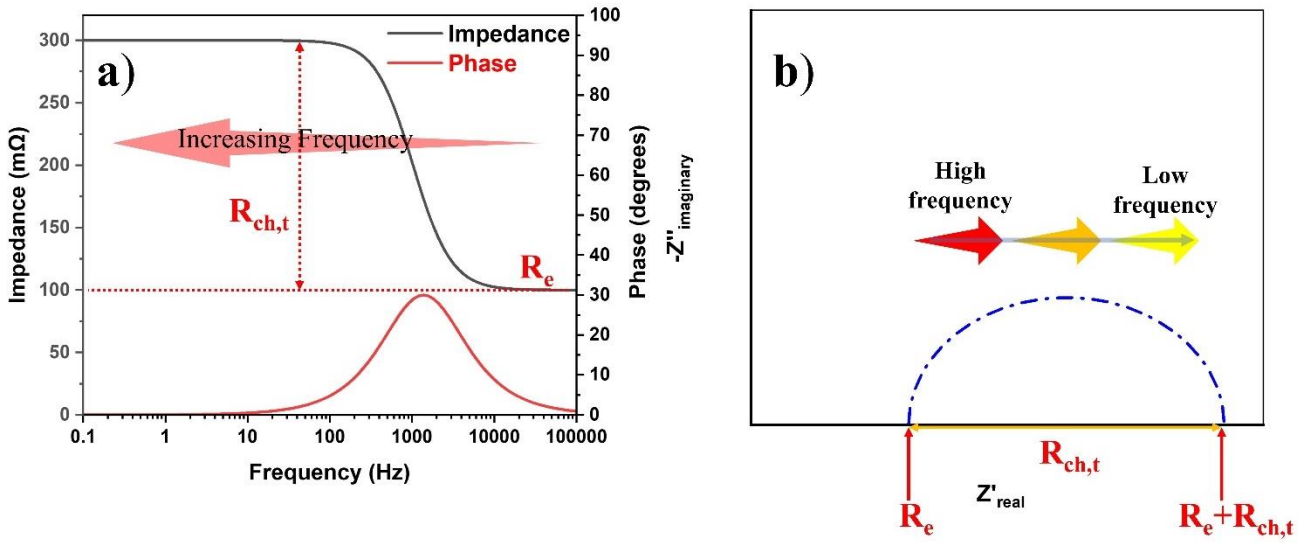

Figure 12: Electrochemical impedance spectroscopy (EIS) a) Bode and b) Nyquist representations

the ohmic resistance (R_e) occurs at the highest frequency, it is the intercept impedance at high frequencies in Bode plot, and the intersection with the Z_{real} axis in the high frequency region in Nyquist plot representations. The rise in impedance in the Bode plot accompanied a change in the phase shift signals charge transfer. The extent of charge transfer is depicted by a charge transfer resistance ($R_{ch,t}$) represented by the difference between the two intercepts at the high and low frequency domains. On the other hand, it is represented by the diameter of the semicircle in Nyquist plot representations [92, 93].

In this dissertation, electrochemical impedance spectroscopy measurements were performed in order to estimate the charge transfer, and the mass transfer resistances. During data collection, the system was set at 80^{o}C with no backpressure, and fed with H_2 and O_2. Therefore, due to the slower reaction rate possessed by the ORR compared to the HOR, the charge transfer resistance is assumed to be ORR resistance. The EIS was done in a galvanostatic mode with an AC amplitude of 10% DC and at 200 mA.cm^{-2} and 800 mA.cm^{-2} bias potentials. Unless otherwise specified, the data were represented using Nyquist plot and are modeled using the following equivalent circuit:

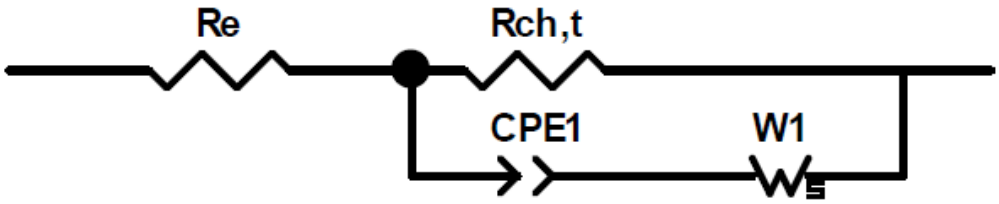

Figure 13: Equivalent circuit model

Where, R_e, and $R_{ch,t}$ represent the ohmic and the charge transfer resistances. CPE is a constant phase element representing the incomplete capacitive behavior on the surface of the catalyst. CPE was used due to the high porosity of the utilized electrodes and the emergence of depressed semicircles. W_s is a bounded Warburg element depicting mass transport within the electrode.

2.2.3. Cyclic Voltammetry (CV)

Cyclic voltammetry is a basic, yet very important electrochemical measurement utilized for a variety of electrochemical systems. It consists of cycling the system between two cut-off voltages in a triangular wave. In the meantime, the current is recorded to track any evolution of an electrochemical phenomenon. These phenomena are based on a movement of charge (electrons or ions) within the system. Cyclic Voltammetry can be performed both in-situ and ex-situ based on the purpose of the experiment. Ex-situ measurements are usually done to evaluate the characteristics of the catalyst in a standard 3-electrode system configuration. Within that configuration, a counter electrode is used such as Pt wire or graphite, and a reference electrode such as Ag/AgCl or Hg/Hg_2Cl_2 are used. The reference electrode ensures a Nernstian behavior of the redox reaction, it maintains a stable potential over time, and is durable. Within the system, an acidic solution providing proton conduction is used such as perchloric acid or sulfuric acid. This method is a swift technique used to study the relative activities of different catalysts in different conditions. In addition, in-situ measurement is widely employed in two-electrode configuration. Within this configuration, one of the electrodes serves as the working electrode while the other is regarded as the counter and a pseudo-reference electrode. Due the fact that the ORR activity is characterized by its sluggish kinetics, the working electrode is mostly referred to the cathode while the anode is used as a counter/reference electrode [94].

2.2.3.1. Electrochemical Surface Area (ECSA)

The electrochemical surface area is regarded as the total area accessible for the surface reactions (ORR and HOR) to occur. The ECSA is usually less than the theoretical surface area of the total Pt. That is because the accessible surface area for reaction depends on the suitable contact between Pt, and the proton conducting moieties (Triple phase boundary). Therefore, due to the poor contact between Pt and Nafion®, not all the Pt surface is employed for reaction. The ECSA is measured using cyclic voltammetry between 0.045V and 0.95V. During the forward increasing potential, hydrogen oxidizes to protons. The protons reduce back in the backward scan. The aforementioned phenomena occur in a voltage

window between 0.06V and 0.35V (Figure 14). Integrating the region below gives us an estimate of the total charge (q) which is normalized by the amount of Pt loaded within a particular electrode area according to the following equation:

$$ECSA\ (m^2.g^{-1}) = \frac{Q}{\theta \times m_{Pt}} \tag{2.7}$$

Where, Q is average charge corresponding to the average area integrated from the anodic and cathodic peaks, θ is the surface coverage of Pt equals to 0.21 mC.cm^{-2}, and m_{pt} is the mass loading of Pt with the electrode surface area measured in $mg_{pt}.cm^{-2}$ [94, 95].

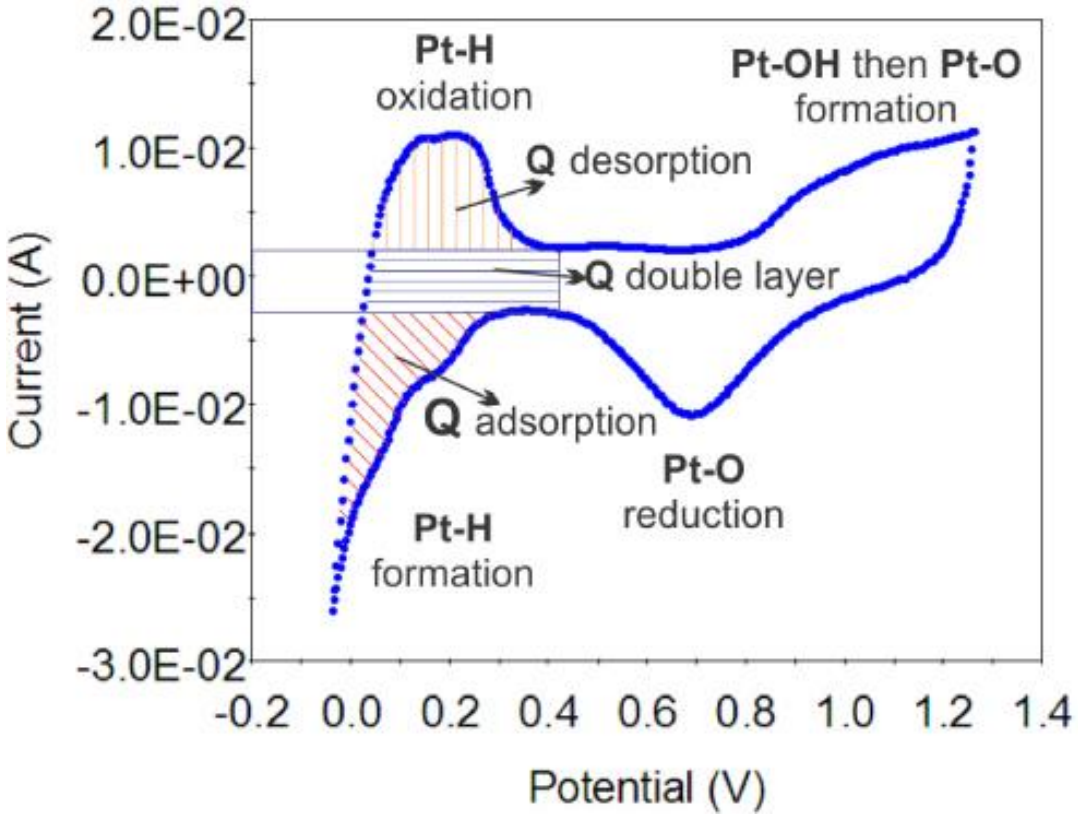

Figure 14: Typical cyclic voltammetry profile of an electrode tested in ex-situ mode [96]

In this dissertation, cyclic voltammetry is used both in-situ and ex-situ are utilized. In-situ measurements were used to evaluate the ECSA of the fibrous electrodes and the contact extent between Pt and S-SiO_2. Plus, it was used to track the dissolution of Pt and the corrosion of the carbon

support after AST. Ex-situ measurements were used to calculate the ECSA of Pt/C catalysts with Nanorod-CeO_2 and Nanorod-CeO_2/NrGO additives.

2.2.4. Linear Sweep Voltammetry (LSV)

2.2.4.1. Hydrogen Crossover

Ideally, polymer electrolyte fuel cell MEAs are supposed to have both electrodes separated. Only proton conduction happens between both while electrochemical reactions occurring on each. However, the reality is that hydrogen crosses over from the anode to the cathode causing a decrease in the overall potential of the MEA [97]. Although oxygen can also cross over from the cathode to the anode, the latter is more common due to hydrogen's faster diffusion. This phenomenon is called the hydrogen crossover. In addition to decreasing the local potential, when hydrogen crosses over and reacts with oxygen, the generated heat can cause the formation of pinholes within the membrane [98]. In order to monitor hydrogen crossover, linear sweep voltammetry is performed. While supplying the anode with hydrogen and the cathode with nitrogen, a voltage sweep is applied from low to high voltage. the current generated during the voltage sweep (Figure 15) is directly proportional to the extent of hydrogen crossover through the equation:

$$J_{crossover} = \frac{i_L}{nF} \tag{2.8}$$

Where, $J_{crossover}$ is the crossover flux, i_L is the current recorded during LSV, n is the number of moles of electrons per mole of hydrogen (equals to 2), and F is Faraday's constant [99].

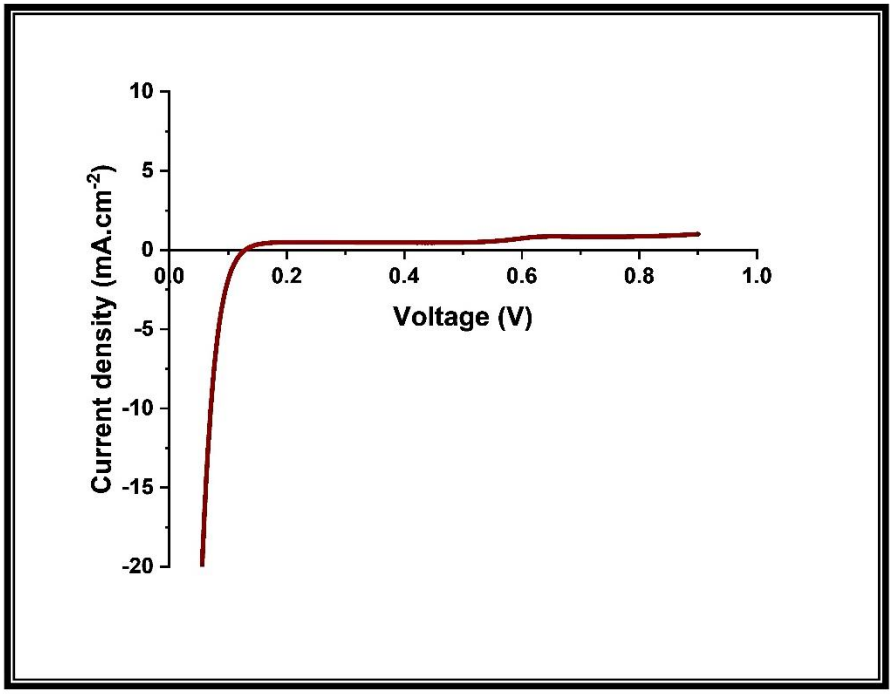

Figure 15: Typical linear sweep voltammetry (LSV) curve of a PEMFC MEA

2.2.4.2. ORR Performance

The electrocatalytic activity of the catalyst can be evaluated in ex-situ configuration using LSV. In a 3-electrode system and rotating disc electrode, the ORR performance can be tracked through tracking the voltage at half wave ($E_{1/2}$). The half-wave potential is the potential needed in order to reach half of the limiting current density recorded in LSV. $E_{1/2}$ gives an idea about the ORR performance of the electrocatalyst. Higher $E_{1/2}$ indicates that the ORR occurs with lower overpotential [100].

For this dissertation, LSV was performed in-situ for all samples using an external potentiostat. The system was fed with H_2 and N_2 on the cathode in fully humidified conditions. The voltage was swept from 0.04 V to 0.9V. All samples have shown minimal limiting current throughout the entire voltage range ($i < 3$ mA). For that reason, LSV crossover data were not shown. Furthermore, ex-situ LSV measurements were conducted

using a rotating disc electrode to evaluate Pt/C performance with nanorod-CeO_2 and nanorod-CeO_2/NrGO additives.

CHAPTER 3: ELECTROSPUN NANOFIBER ELECTRODES FOR BOOSTED PERFORMANCE AND DURABILITY AT LOWER HUMIDITY OPERATION OF PEM FUEL CELLS

The objective of this chapter is to fabricate self-standing Nafion®-free fibrous electrodes using electrospinning. As an alternative to Nafion®, sulfonated silica (S-SiO_2) is to be employed. In addition, the effect of the polymer nature, and the S-SiO_2/carrier polymer ratio on the morphology of the resulting mat is to be investigated. Then, the effect of the fibrous nature of the electrode, S-SiO_2 and their loaded quantities on the performance of the electrodes at different humidity conditions. This is done to investigate the impact of the incorporation of a hygroscopic proton conducting moiety instead of the hydrophobic Nafion®. Finally, the impact of the above parameters on the durability of the platinum and carbon support of the catalyst are studied.

3.1. Introduction

Fossil fuel depletion became a topic widely mentioned worldwide. Therefore, many efforts are being made in the quest of finding a suitable, high-performing, and cost-effective substitute. In this sense, several potential alternatives have emerged, such as Li-ion batteries [101], solar panels [102], and fuel cells for commercial use [103]. Among the various alternatives, fuel cells (FCs) recently gained great attention due to their high energy density and environmental friendliness [104, 105]. Among the various types of FCs, Polymer

electrolyte membrane fuel cells (PEMFCs) have grabbed attention in various applications, especially, in the automotive industry [106]. It comprises a membrane electrolyte assembly (MEA) which is composed of an anode, a cathode, and a proton-conducting polymer membrane between these two electrodes [10]. However, in spite of their several benefits, employing extensive amounts of Pt metal and Nafion® as ionomer presents a significant economic burden limiting their wide commercialization [107-109]. In addition, Nafion® poses restrictions on the PEMFC's operational conditions due to its strong dependence on relative humidity to achieve high proton conductivity [110, 111]. Aside from that, the current potential applications of PEM fuel cells require them to have long lifetimes of 8000 hours for automotive, 20000 hours for busses, and up to 30000 hours for heavy-duty trucks, as prescribed by the US Department of Energy (DoE) [112-114]. To overcome the obstacles and meet the market demands, extensive research has been done in improving the performance and durability of the MEA. Specifically, numerous studies focused on improving the cathode performance and durability, while simultaneously reducing Pt catalyst and Nafion® ionomer contents [115-117]. In this sense, numerous fabrication techniques were developed in favor of enhancing Pt utilization within the electrode such as decal transfer [118], brushing [119], and spraying [120]. However, the aforementioned methods present numerous drawbacks such as pore blockage and non-uniformity in particle distribution [121, 122]. Alternatively, electrospinning emerged as a versatile tool for the fabrication of fiber-based catalyst layer posing many advantages over the other conventional techniques [52, 123]. Thus, higher Pt utilization caused by the even distribution along with the fiber results in high performing low Pt loading PEM fuel cell electrode. Furthermore, electrospinning allows sculpturing electrodes with tailored porous network allowing better mass transfer into and out of the electrode. This was first demonstrated by Kotera in which a self-standing cathode of Pt/C, Flemion™ ionomer, and PEO carrier polymer was fabricated using electrospinning. As a result, the fibrous electrodes outperformed the classical electrodes exhibiting ten times more porosity and gas permeability. This was reflected in lower mass transfer losses during fuel cell operation under 100% RH , 95^{o}C , and 150 kPa backpressure [51]. Shaojing Hong et al. fabricated the electrode with an ultralow Pt loading (0.087 $mg_{Pt.}cm^{-2}$), poly (acrylic acid) (PAA), and Nafion® with 5% PTFE additive with the maximum output of 0.692 $W.cm^{-2}$. The reported fiber-based electrode showed a 1.06 folds

higher performance than the decal electrode loading with 0.18 $mg_{Pt}.cm^{-2}$. It was also reported that fiber-based electrodes prepared using electrospinning conveyed better durability retaining 87.5 % of its initial power output compared to 76% for decal electrodes after 2000 accelerated stress test (AST) cycles. The prolonged durability was explained by the stabilizing effect of PAA on the catalyst through its intrinsic interaction with the carbon support [124]. Moreover, Shaojing Hong et al. later reported a peak performance of 0.62 $W.cm^{-2}$ for a palladium (Pd) deposited fiber-based electrode of 19 $\mu g_{Pt}.cm^{-2}$ loading. The studied electrode lost only 4.8% of its peak power out after AST of 30000 cycles [67]. In another study, MEA prepared by nanofiber PtCo/C/ Nafion®/PAA-based cathode showed 20% higher performance compared to the sprayed electrode both loaded with 0.1 $mg_{Pt}.cm^{-2}$. Here, due to the even distribution of particles along the fibers and inter/intra porous structure, better access to electrochemical sites was attained. Thus the developed MEA exhibited improved durability losing only 8% of its peak power output compared to 32% of the classical sprayed electrode [65]. Furthermore, Pt/C/ Nafion®/PAA fiber-based electrodes with ultralow Pt loading (0.065 $mg_{Pt}.cm^{-2}$) recorded a maximum power output of 360 $mW.cm^{-2}$ which was 29% higher than for decal electrodes with 0.104 $mg_{Pt}.cm^{-2}$ loading. In another study, Pt/C/ Nafion®/PVDF fiber-based electrodes with 0.1 $mg_{Pt}.cm^{-2}$ loading resulted in a 35% higher power density than the conventional sprayed electrode recording a peak power density of 545 $mW.cm^{-2}$ [61]. It is observed that PVDF-based fiber electrodes performed slightly lower than PAA-based fiber electrodes. The superior performance of PAA carrier-based fibrous electrodes can be attributed to the hydrophilic nature of the PAA compared to PVDF. However, and for the same reason, PVDF-based fiber electrodes showed better durability due to their water expulsion ability alleviating the electrode corrosion rate.[63] Recently, P(VDF-TrFE); a copolymer of PVDF; has drawn lots of attention in various applications such as self-charged supercapacitor separator membranes [125, 126], energy harvesting [127], pressure sensors [128], and tissue engineering applications [129]. This is due to the ferroelectric behavior and crystallinity which P(VDF-TrFE) copolymers exhibit.[129] In addition, our previous study demonstrated the superior water retention capability of P(VDF-TrFE)/sulfonated silica compared to that of PVDF/sulfonated silica-based electrospun membranes making them promising in PEMFC electrodes, especially at low humidity levels [130].

On the ionomer level, efforts are being made to develop high performing and cheaper alternative to Nafion®. For instance, hydrocarbon-based ionomers such as sulfonated poly (ether ether ketone) [15, 16], polyamides [17], polyphosphazene [18], and polysulfones have been extensively studied [19], However, hydrocarbon ionomers pose a series of problems including their ability to be dissolved in aprotic solvents of high boiling points [20, 21], Consequently, the unevaporated solvent deposits on the Pt catalyst confine its activity [22], In this sense, several studies reported the deposition of the aromatic ring of sulfonated hydrocarbon polymers on the Pt catalyst surface limiting its oxygen reduction reaction (ORR) activity [131]. Recently, inorganic-based proton conducting ionomers gained attention due to their good performance in dry conditions. Eastcott and Easton investigated the performance of MEA employing sulfonated silica (S-SiO_2) as a proton-conducting ionomer. Although Nafion®-based MEAs outperformed S-SiO_2-based MEAs in fully humidified conditions, S-SiO_2 showed promising performance in partially humidified conditions [23-25]. Nevertheless, in another study, the author suggests that S-SiO_2 stabilizes the Pt catalyst reducing the electrochemical surface area (ECSA) loss to 26% compared to 93% loss for those with Nafion® as ionomer after AST [1].

Herein, the incorporation of P(VDF-TrFE) carrier-polymer Pt/C/sulfonated silica (S-SiO_2) particles in fiber-based PEM fuel cell electrodes were investigated for the first time. Pt/C, S-SiO_2 particles along with a carrier polymer P(VDF-TrFE) were fabricated via electrospinning. Additionally, this study further discusses the effect of the S-SiO_2/polymer ratio on the morphology and performance of the electrodes. The fiber morphology and particle distribution along the fibers were investigated through scanning electron microscopy (SEM) and transmission electron microscopy (TEM). The porous characteristics of the fibrous catalyst layers were investigated by mercury intrusion porosimetry (MIP). Besides morphological analysis, PEM fuel cell performance and in-situ electrochemical impedance spectroscopy (EIS), and cyclic voltammetry (CV) analysis were performed to reveal a deeper insight into the impact of S-SiO_2/polymer ratio and the nature of the carrier polymer on the performance of the electrodes. Finally, both Pt dissolution and carbon corrosion accelerated stress durability tests (AST) were conducted in favor of studying the performance of the electrodes at extended operation times.

3.2. Experimental Section

3.2.1. Material

Cetyltrimethylammonium bromide (CTAB) and an aqueous solution of sodium silicate were purchased from AppliChem. Polyvinylidene fluoride (PVDF; Solef, MW: 380 000) and poly(vinylidene fluoride-*co*-trifluoroethylene) (70/30 mol) powders were purchased from Solvay and PolyK technologies, respectively. Dimethylformamide (DMF), acetone, tetrahydrofuran (THF), N,N-dimethylacetamide (DMAc), sulfuric acid (H_2SO_4), and 20 wt % Nafion® solutions were all obtained from Sigma-Aldrich. HiSPEC 40% Pt on carbon (HiSPEC 4000) and 30% Pt on Vulcan XC-72R were obtained from Fuel Cell Earth LCC.

3.2.2. Preparation of Electrospinning Inks

Prior to the electrospinning ink preparation, sulfonated silica particles were synthesized in accordance with a previously reported study[130]. In brief, 34 mL of sodium silicate was added dropwise into a 78 mL CTAB solution under continuous stirring at 40 °C for 1 h. The pH of the solution was then adjusted to 11 through the slow addition of 1 M hydrochloric acid (HCl) solution followed by stirring for an additional 1 h. The resulting silicate solution was moved into a Teflon-lined stainless-steel autoclave and heated up to 120 °C for 48 h. After separating the resulting silica and drying for 24 h at 60 °C, the obtained product was calcined at 550 °C under an air atmosphere for 14 h. Sulfonation of the as-prepared silica was performed by stirring it in concentrated sulfuric acid solution (H_2SO_4) for 30 min and then heating in the dispersion in an autoclave at 120 °C for 48 h. Finally, sulfonated silica was then obtained through filtration and dried overnight at 60 °C. Then, a polymer stock solution of 10% (wt %) was prepared in 7:3 DMAc/THF solvent mixture. Similarly, 20% Nafion® stock solution was prepared in DMF/acetone (7:3) solution. The electrospinning inks were generally composed of Pt/C, S-SiO_2, polymer solution, and DMF and acetone as solvents (Table 1). Ink preparation was as follows: (i) Pt/C was added into a vial. (ii) DMF was added. (iii) The solution was stirred for 2 min and bath sonicated for 30

min. (iv) Acetone was added, followed by ionomer (S-SiO_2 powder or 20% Nafion® solution). (v) The solution was again bath-sonicated with intermittent stirring for 60 min. (vi) The stock 10% polymer stock solution was added, and (vii) the ink was left to stir overnight at room temperature.

Table 1: Electrospun fibrous mat composition

Ink	Dry electrode composition (wt. %)	Solvent	Total solid ratio (%)
1	Pt/C: 65, PVDF: 17, S-SiO_2: 18	DMF/Acetone	13
2	Pt/C: 65, PVDF: 15, S-SiO_2: 20	DMF/Acetone	13
3	Pt/C: 65, PVDF: 13, S-SiO_2: 22	DMF/Acetone	13
4	Pt/C: 65, P(VDF-TrFE): 17, S-SiO_2: 18	DMF/Acetone	18
5	Pt/C: 65, P(VDF-TrFE): 15, S-SiO_2: 20	DMF/Acetone	18
6	Pt/C: 65, P(VDF-TrFE): 13, S-SiO_2: 22	DMF/Acetone	18
7	Pt/C: 65, PVDF: 15, Nafion®: 20	DMF/Acetone	15
8	Pt/C: 77, Nafion®: 23	Isopropyl alcohol	-

For simplicity, 18% S-SiO_2-T, 20% S-SiO_2-T, 22% S-SiO_2-T, 18% S-SiO_2-P, 20% S-SiO_2-P, 22% S-SiO_2-P, and 20% Naf-P will be used throughout the study to designate the nature of the ionomer, its amount (%), and the nature of the polymer (T for P(VDF-TrFE), and P for PVDF) in the electrode.

3.2.3. Electrospinning Parameters

Electrospinning was performed in a custom-made electrospinning chamber with controllable temperature, relative humidity (RH %), and a grounded rotating drum. The ink

was loaded into a 5 mL syringe and was electrospun using an 18-gauge stainless-steel needle spinneret (Figure 16a). In the process, high voltage was applied at the tip of the needle against a grounded stainless-steel drum wrapped with aluminum foil. All electrospinning processes were conducted with a flow rate range of 1–1.2 mL/h, 13 kV applied voltage, 60–70% relative humidity (% RH), and a 10 cm needle-to-collector distance. The collector drum was set to rotate at a speed of 200 rpm and oscillate horizontally for better uniformity.

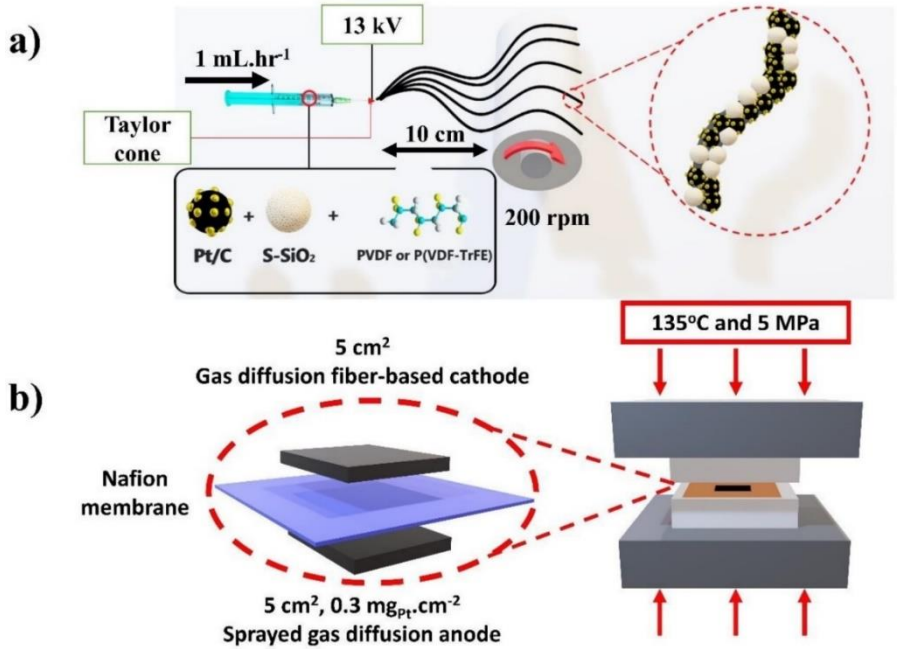

Figure 16: Schematic of (a) electrospinning process parameters and ink components and (b) MEA preparation procedure.

For the resulting fiber mat, the Pt-loading was estimated by taking a 5 cm^2 portion from the total mat, weighing it on a sensitive balance, and calculating the final Pt-loading using the following equation:

$$m_{Pt/cm^2} = \frac{m_{Pt/C} \times \%Pt\ in\ Pt/C \times m_{5cm^2 sample}}{m_{ink} \times \%\ solid\ weight\ ratio\ \times 5} \quad (3.1)$$

In which, $m_{Pt/C}$ is the mass of Pt/C used during the ink preparation, $m_{5cm^2 sample}$ is the mass of the obtained 5 cm^2 sample, m_{ink} is the total mass of the prepared electrospinning ink, and % solid weight ratio is the total solid amount per total solvent used during ink preparation.

3.2.4. Morphological Analysis

The surface morphology of the fibers was investigated using scanning electron microscopy (SEM) using a German Jeol JSM 6010 LV and Supra 35VP Leo. The fiber samples were coated with Au/Pt using a Cressington 108 sputter coater at 40 mA for 120 s. The images were taken with 3–5 kV accelerating voltage and an 8–9 mm working distance. The average fiber diameter and void spaces were estimated using ImageJ software by randomly selecting 30 fibers (or sites) for measurement. The morphology and elemental distribution across the fiber mats were investigated via transmission electron microscopy (TEM)/energy dispersive spectrometry (EDS) using a JEOL JEM 2000FX transmission electron microscope at an accelerating voltage of 200 kV. The porosity and the pore size distribution were traced using a Micromeritics AutoPore IV 9500 V1.09 mercury (Hg) porosimeter. Mercury of 485 dyn cm^{-1} surface tension forcefully penetrated the pores of the electrospun fibrous mat.

3.2.5. MEA Preparation

For the anode, gas diffusion electrodes (GDE) were prepared via airbrushing with a fixed Pt loading of 0.3 mg cm^{-2}. The inks were prepared in a vial by adding 0.15 g of 20% Nafion® solution onto 0.1 g of 30% Pt/C catalyst followed by the addition of 8 mL of isopropyl alcohol (IPA). The solution was then sonicated for 1 h and then stirred for another 2 h. The GDEs were fabricated by the spraying of Pt/C/ Nafion® inks onto a Sigracet 39 BC carbon paper gas diffusion layer (GDL). Spraying was repeated to obtain the desired Pt loading. Each spraying step was followed by drying at 60 °C for 10 min. From the electrospun fiber mat, a 5 cm^2 sample was taken and the Pt loading was calculated. The fibrous mat was then pressed as a cathode against a GDE anode and a Nafion® membrane in between. The MEA was first preheated for 10 min at 135 °C without applying any force, followed by another 5 min under 5 MPa (Figure 16b).

3.2.6. Contact Angle Measurement

In order to determine the hydrophobicity of the fiber based GDEs, water contact angle (WCA) measurements were performed using a KSV Attention T200 theta instrument. In the process, 5 μL of deionized water was dropped on top of the GDE using a syringe all at a fixed working distance and at room temperature. To obtain a statistically accurate contact angle, three trials were performed.

3.2.7. Fuel Cell Tests and in Situ Electrochemical Analyses

Fuel cell performance tests and in situ impedance analysis were conducted using a Scribner Series 850e with controlled back pressure, temperature, and humidity conditions. All tests were conducted on a single cell composed of 5 cm^2 MEA and with single serpentine hydrogen gas and airflow channels. Initially, the MEA was conditioned by alternatively subjecting it to cycling voltages of 0.2 and 0.6 V until a stable current density was obtained. Throughout the process, the cell temperature was maintained at 80 °C, and fully humidified hydrogen gas and air flows (0.125 L min^{-1} and 0.5 L min^{-1}, respectively) were fed at ambient pressure. Prior to fuel cell polarization curve data collection, the system was maintained at 0.2 V to condition and stabilize the MEA. Then, fuel cell polarization curves were collected between 0.2 V and the open-circuit voltage (OCV) under both fully humidified and 60% partially humidified conditions. The cell was fed with H_2 at the anode and air at the cathode at respective flow rates of 0.125 L min^{-1} and 0.5 L min^{-1} air with 25 psi of backpressure.

Electrochemical impedance spectrograms (EIS) were collected under fully humidified conditions. Hydrogen and oxygen gases were stoichiometrically (1:1 ratio) supplied to the anode and cathode, respectively with a flow rate maintained at 0.125 $L.min^{-1}$. The data were collected through a sweeping frequency in the range of 0.1-10000 Hz with an AC amplitude being set to 5% of the applied DC current with 20 points collected per decade. Prior to data collection, the system was maintained at the selected current density for a span of 10 minutes in favor of stabilizing the system. The linearity of the EIS data was validated using linear Kramers-Kronig validity test software developed by the Karlsruhe Institute of Technology [132]. Finally, the resulting Nyquist plots were fitted and analyzed using Zview software.

In-situ cyclic voltammetry (CV) was performed at 30 °C with a hydrogen flow of 0.1 L/min while no input was supplied to the cathode. After stabilizing the electrodes, cyclic voltammograms were collected at a 40 mV/sec scan rate within a voltage window of 0.045-0.9V. The area average area under both the adsorption and desorption peaks was estimated and the electrochemical surface area (ECSA) was calculated using:[133]

$$ECSA\ (m^2.g^{-1}) = \frac{Q}{\theta \times m_{Pt}} \quad (5.2)$$

Where Q is the average charge measured corresponding to the average area integrated with the anodic and cathodic peaks, θ is the surface coverage of hydrogen on Pt (0.21 $mC.cm^{-2}$) and m_{pt} is the mass loading of Pt within the electrode.

Pt-dissolution accelerated stress tests (AST) were conducted in fully humidified (100% RH) H_2(anode)/N_2(cathode) atmosphere with flow rates of 0.125 $mL.min^{-1}$ and 0.25 $mL.min^{-1}$, respectively. Using an external potentiostat, the MEA was cycled with a square wave in an alternating fashion at 0.6 V and 0.95V for 3 seconds each repeated 30000 times. It should be noted that before and after the AST test, all data relevant to fuel cell polarization curve, ECSA, and EIS were collected. In addition, SEM images were collected for the fibrous cathode before and after the durability tests.

Finally, a carbon corrosion stress test (AST) was conducted in accordance with the fuel cell commercialization conference in Japan and the DoE [134]. The MEA was set in a fully humidified H_2 (anode)/N_2 (cathode) atmosphere at 80ºC with flowrates of 0.125 $mL.min^{-1}$ and 0.25 $mL.min^{-1}$ respectively. Using an external potentiostat, a triangular wave was applied and repeated 1000 times between 1 and 1.5 V with a 500 mV/sec scan rate. fuel cell polarization curves, ECSA data, and SEM images were collected before (beginning of life (BOL)) and after the test (end of life (EOL)).

3.3. Results and Discussion

Continuous ionic and electronic conduction throughout the fiber structure necessitates a fine and even distribution of the particles throughout the fiber [135]. Therefore, SEM micrographs show S-SiO_2-T (Figure 17 a,b,c) and S-SiO_2-P (Figure 17d,e,f) with evenly distributed particles throughout the entire fiber with the absence of any noticeable beads. Upon increasing the S-SiO_2/polymer content, the average fiber diameter generally decreased

recording 0.9 μm, 0.77 μm, and 0.53 μm for 18% S-SiO_2-T, 20% S-SiO_2-T, and 22% S-SiO_2-T mats, respectively. Similarly, the average fiber diameter has decreased from 1 μm to 0.68 μm, and 0.62 μm for 18% S-SiO_2-P, 20% S-SiO_2-P, and 22% S-SiO_2-P, respectively. Furthermore, the average void space between the fibers shows an increase from 1.14μm for 18% S-SiO_2-T fiber-based mat to 2.46 μm for 22% S-SiO_2-T, and from 1.47 μm to 2.48 μm for 18% S-SiO_2-P and 22% S-SiO_2-P, respectively. The porous texture of the fiber mat was further revealed through MIP. The pore size distribution graph (PSD) (Figure 18) shows that the majority of the pore volume for fiber mats is mainly concentrated within the ≤100 μm range. However, compared to S-SiO_2-P, S-SiO_2-T fiber mats recorded a higher median pore diameter (volume) of 28.09 μm (15.35 μm for S-SiO_2-P). The higher median pore diameter possessed by P(VDF-TrFE)-based fiber mats is expected to affect the diffusion mechanism of O_2 and water expulsion within the electrode [136, 137]. In addition, PVDF and P(VDF-TrFE)-based fiber mats recorded 85.84% and 72.76% porosity and skeletal density of 1.24 g. mL^{-1} and 0.75 g.mL^{-1}, respectively. Consequently, the high porosity possessed by both mats enhances the tortuosity, and thus, oxygen diffusion and water expulsion within the electrode directly affect the performance of the PEMFC electrode [138-140]. Furthermore, intra-fiber pores can be readily observed within the fiber in the fiber transmission electron microscope (TEM) and darkfield images (Figure 19 a,b,e,f). Intra-fiber pores are expected to serve in increasing the Pt utilization within the bulk of the fiber. Enhanced Pt utilization can

be achieved through the adequate distribution of the ionomer being close to the electrochemical reaction centers [56].

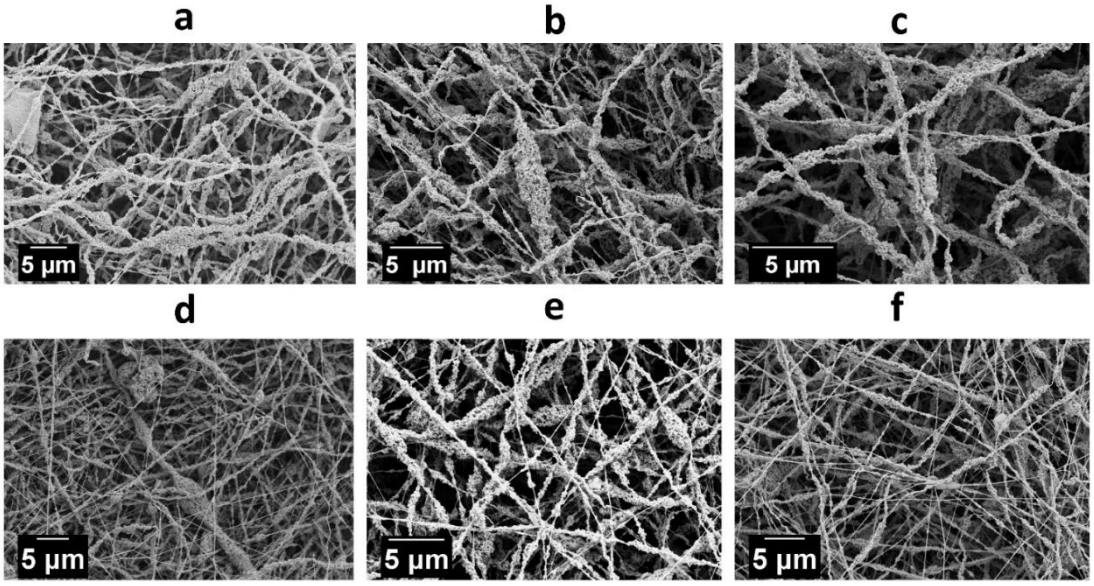

Figure 17:SEM images of a) 18% S-SiO_2-T, b) 20% S-SiO_2-T, c) 22% S-SiO_2-T, d) 18% S-SiO_2-P, e) 20 % S-SiO_2-P, and f) 22% S-SiO_2-P fiber mats

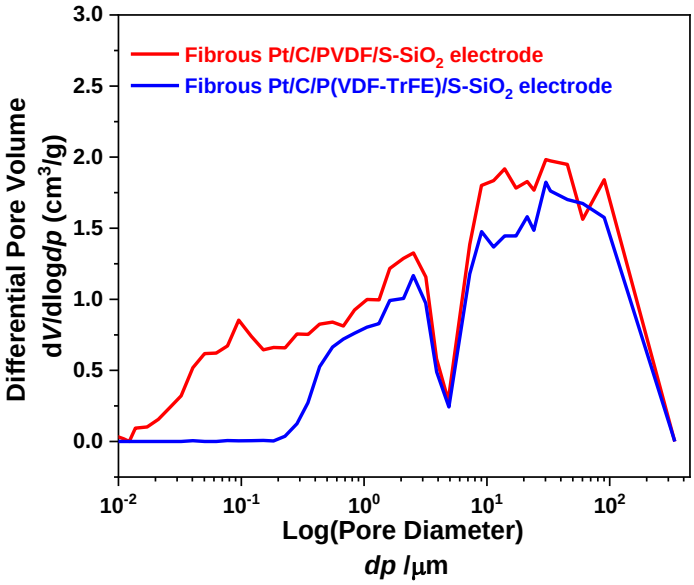

Figure 18:Pore size distribution graph (PSD) of electrospun PVDF and P(VDF-TrFE) based Pt/C/S-SiO_2 electrodes

EDS mapping of 18% S-SiO_2-T and 18% S-SiO_2-P (Figure 19 c,g) shows that both Pt with uniform distribution throughout the fiber. More importantly, Figure 19c,g,d, and h highlight an overlapping distribution for Pt and S-SiO_2 ensuring a proper contact and thus proton conduction into the Pt surface. The extent of proton conduction can be reflected through the ECSA obtained from the cyclic voltammograms of the respective MEAs (Figure 20a, Figure 21). The ECSA shows an abrupt increase upon increasing the S-SiO_2 loading from 18% to 22%, indicating an enhanced contact surface between S-SiO_2 and Pt (Figure 20a). In comparison with the other electrodes, S-SiO_2-T fibrous electrodes recorded a higher ECSA compared to the conventionally sprayed electrode (22.35 $m^2.g_{Pt}^{-1}$) underlining the impact of electrospinning in boosting the exposure of Pt surfaces. Similarly, ECSA of S-SiO_2-T fibrous electrodes exceeded that of 20% Naf-P fibrous electrodes (34.24 $m^2.g_{Pt}^{-1}$). This can be explained through the inability of Nafion® to penetrate the mesopores of the catalyst disrupting proton conduction into a significant portion of Pt [141].

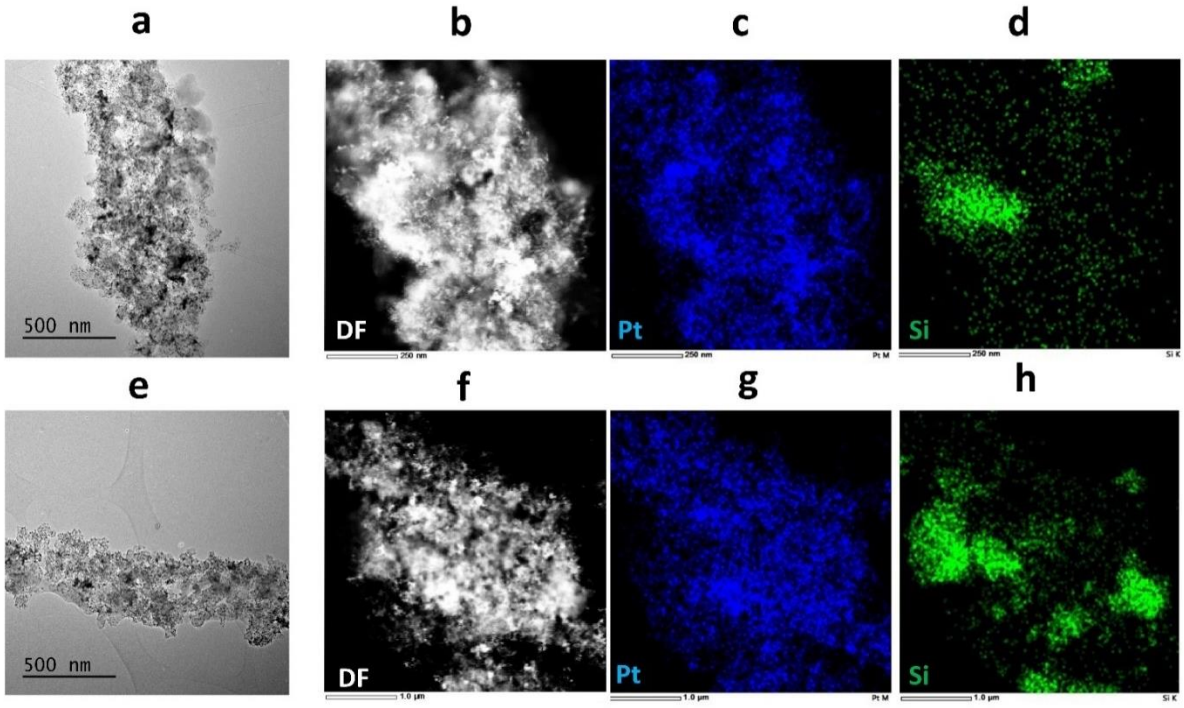

Figure 19:Transmission electron microscopy images of a,e) 18% S-SiO_2-T and 18% S-SiO_2-P, b,f) their dark field image, and their EDS elemental mapping of c,g) Pt, and d,h) Si, respectively.

PEM fuel cell performance tests (Figure 20b) reveal an explicit outperformance of fiber-based electrodes over the sprayed ones. The potential losses were evaluated at both low current density (400 $mA.cm^{-2}$); in which activation losses dominate; and high current density (1000 $mA.cm^{-2}$); in which concentration losses dominate. At low current density, fiber-based electrodes recorded lower potential losses (0.55V) as compared to the sprayed electrode (0.45V). The lower kinetic overpotential exhibited by the fibrous electrodes is a direct consequence of higher Pt utilization within the electrode, which in turn results in better contact between Pt and S-SiO_2. Likewise, the greater porosity exhibited by fibrous electrodes enables smoother passage of oxygen into and the expulsion of water from the reaction sites causing lower mass transfer overpotential. A similar outcome was obtained in a number of studies in which PVDF/Nafion®/Pt/C-based fibrous electrodes recorded a 35% increase in their peak power density as compared to the conventional sprayed electrodes [61].

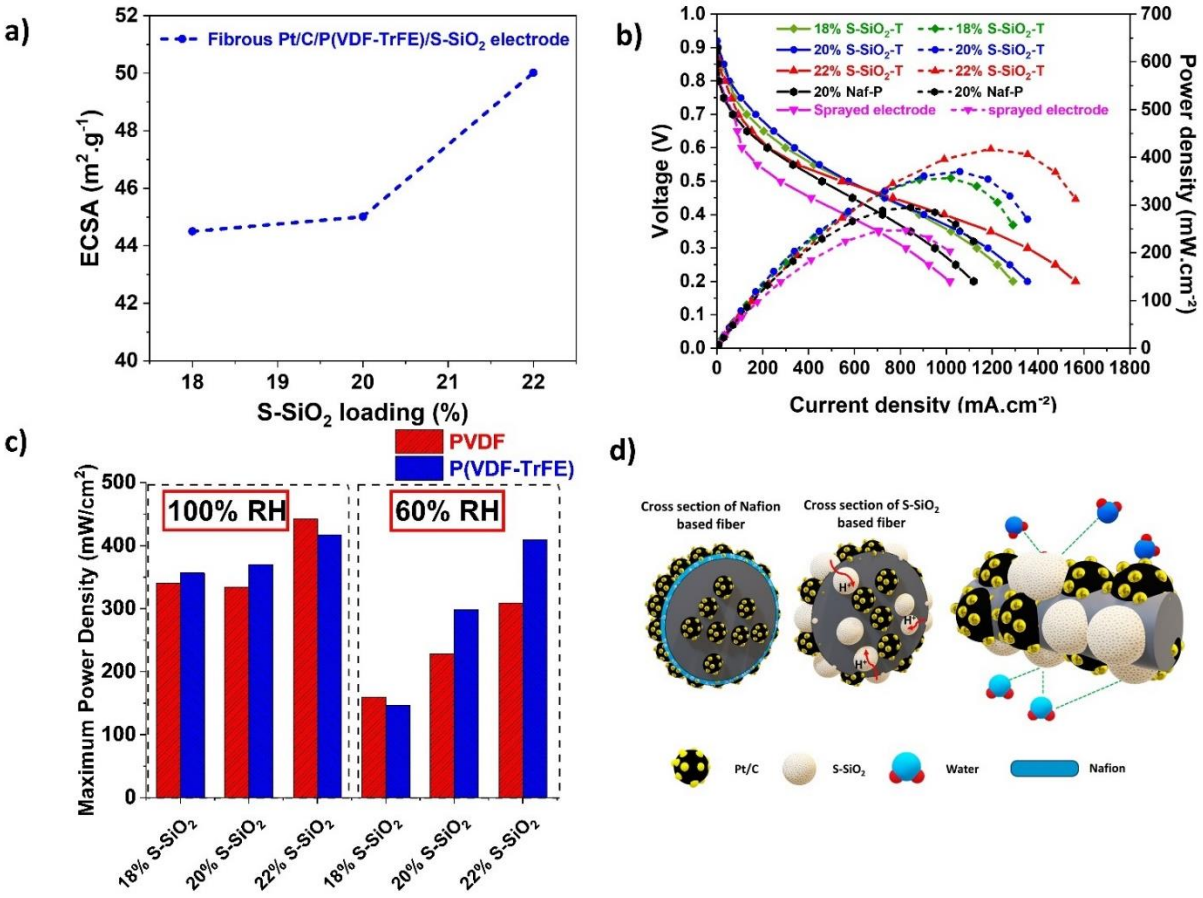

Figure 20: a) ECSA values of S-SiO_2-T electrodes with varying S-SiO_2 content,b) fuel cell polarization curves at fully humidified conditions, c) comparative bar graph of the fuel cell maximum power density recorded for S-SiO_2-T and S-SiO2-P electrodes with varying S-SiO_2 loadings at fully humidified (100%RH) and partially humidified (60% RH) conditions, and d) a schematic comparing the proton conduction mechanism in S-SiO_2 and Nafion® containing electrodes, and the water retention within the fibrous electrode.

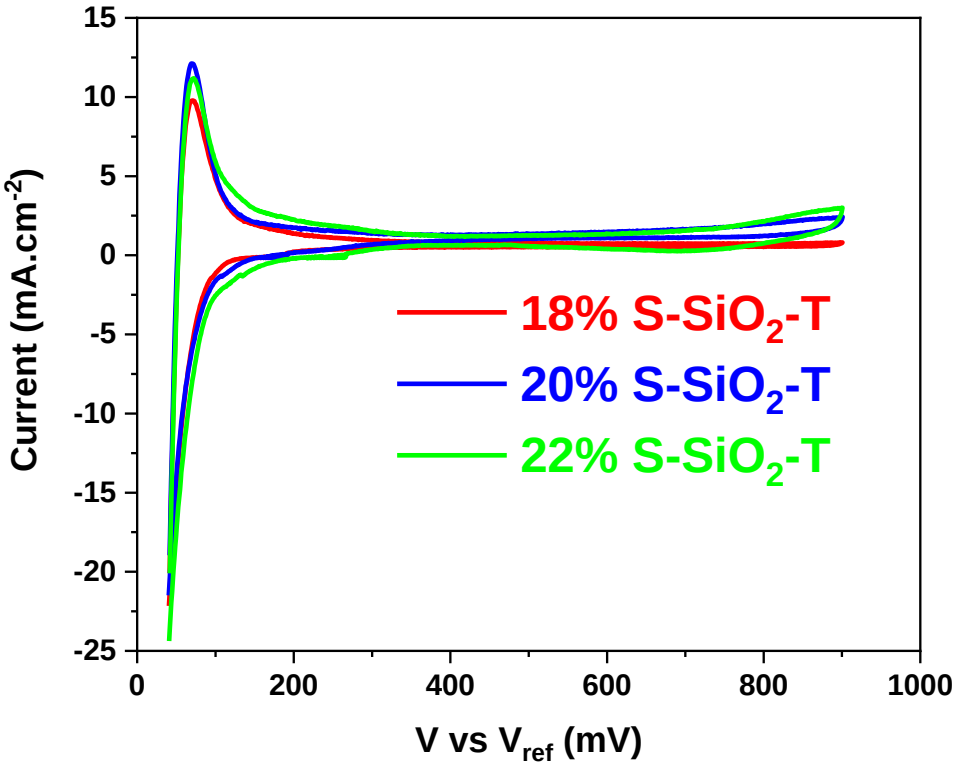

Figure 21: Cyclic voltammograms of 18% S-SiO_2-T, 20% S-SiO_2-T, and 22% S-SiO_2-T fiber-based electrodes at BOL obtained between 0.045V and 0.9V at 30°C in dry condition.

Increasing S-SiO_2 caused an overall enhancement in the performance of the fuel cell at all humidity levels. The maximum power output has increased from 356.5 $mW.cm^{-2}$ to 417.4 $mW.cm^{-2}$ (14.59 % increase) in fully humidified conditions as the S-SiO_2 loading was increased from 18% to 22%. The increase in performance was more noticeable in partially humidified conditions (60% RH) showing a 64.15% increase in maximum power performance (Figure 20c). The introduction of additional S-SiO_2 enhances proton conduction into the reaction center which results in a rise in the overall performance [142]. This was clearly seen upon comparing the performance of S-SiO_2-T electrodes in partially humidified conditions (60% RH) in which conduction is dominated by the S-SiO_2/Pt interface and partially excludes the water/Pt interface solidifying the findings obtained earlier in Figure 20a. To assess the ORR kinetics, EIS measurements were performed at 200 $mA.cm^{-2}$ where the kinetic losses prevail over the mass transfer and ohmic losses. Thus, the equivalent circuit proposed upon fitting represents all three processes. However, emphasis was given to the kinetic losses (ORR resistance) at the given current density. The Nyquist plots (Figure 22) and their corresponding fitting results (Table 2) indicate a drop in the charge transfer (ORR) resistance from 0.145 Ω to 0.114 Ω upon increasing the S-SiO_2 content from

18% to 22%. Increasing the S-SiO_2 loading results in enhanced surface contact with the electroactive centers leading to better accessibility resulting in enhanced ORR activity. Furthermore, unlike Nafion®, S-SiO_2 does not form a thin film on the surface but is able to penetrate the nanofibers through its pores, providing enhanced contact with Pt particles buried within resulting in enhanced Pt utilization (Figure 20d) [56]. This was shown through the higher ECSA values of S-SiO_2-containing electrodes compared to their Nafion® counterpart (34.24 m^2. g^{-1}). Meanwhile, the high inter-fiber porosity possessed by S-SiO_2-T electrodes with higher S-SiO_2P(VDF-TrFE) ratios has shown lower mass transfer resistance component values (W_R) in the Nyquist plots collected at high current density (800 $mA.cm^{-2}$). This can originate from the hygroscopic nature of S-SiO_2 combined with the hydrophobic P(VDF-TrFE) serving in maintaining adequate water level within the electrode (Figure 20d) [143-145].

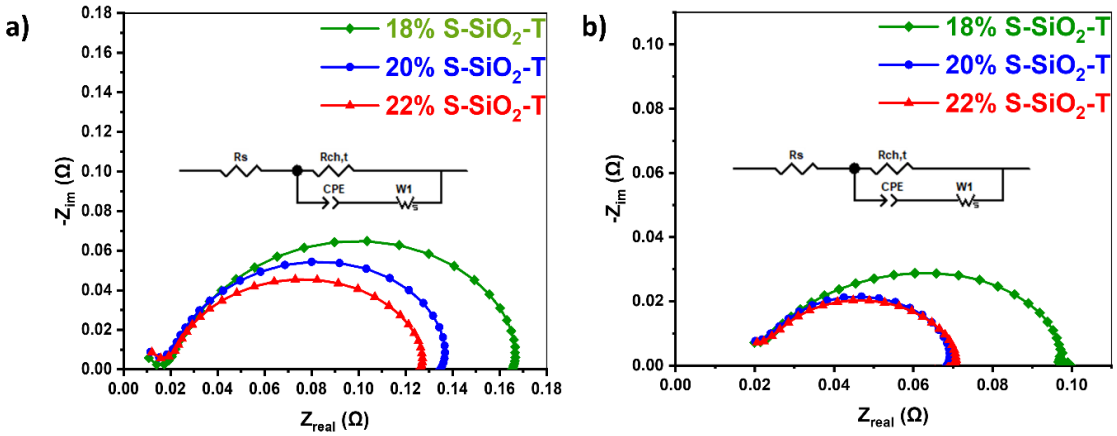

Figure 22: Nyquist plots of 18 % S-SiO_2-T, 20 % S-SiO_2-T, and 22 % S-SiO_2-T fibrous electrodes at fully humidified (100% RH) condition recorded a) 200 $mA.cm^{-2}$ and b) 800 $mA.cm^{-2}$ and their corresponding equivalent circuit. R_e corresponds to the bulk resistance, $R_{ch,t}$ corresponds to the charge transfer resistance and W_R corresponds to the mass transfer resistance

Table 2: Maximum power output and EIS fitting results P(VDF-TrFE)- based fibrous electrodes obtained at 100% RH. R_e, $R_{ch,t}$, and W_R represent the ohmic, charge transfer, and mass transfer resistance, respectively.

Electrode	**R_e (Ω)**	**$R_{ch,t}$(Ω)[a]**	**W_R(Ω)[b]**	**Maximum Power Density ($mW.cm^{-2}$)**

18% S-SiO_2-T	0.015	0.145	0.084	356.5
20% S-SiO_2-T	0.014	0.115	0.036	370.1
22% S-SiO_2-T	0.015	0.106	0.027	417.4

(a)Obtained at 200 mA.cm^{-2}

(b)Obtained at 800 mA.cm^{-2}

The distinction in fiber morphology was evident upon comparing S-SiO_2-P and S-SiO_2-T electrodes in the different process-dominated regions of the polarization curve (Figure 23). S-SiO_2-T electrodes have noticeably shown better performance in the mass transfer region which can be attributed to the wider pore diameter exhibited by S-SiO_2-T electrodes. The wider pore diameter exhibited by P(VDF-TrFE)-based electrodes (28.09 μm) permits a less resistive passage of oxygen and water into and outward of the electrochemical active centers. On the other hand, S-SiO_2-T fibrous electrodes exhibited remarkable retention in power output at lower humidity levels. This can be mainly due to the dual function of S-SiO_2 in providing proton conduction pathways on one hand and preserving an adequate water level within the electrode. The latter can be attributed to the hygroscopic nature of S-SiO_2 [23]. This can be clearly observed in Figure 5c in which S-SiO_2-T electrodes retained 41.2%, 80.6%, and 98.2% of their maximum power densities upon increasing the S-SiO_2 loading from 18% to 20%, and 22% S-SiO_2, respectively. Likewise, PVDF-based electrodes retained 46.8% ,68.3% and 69.9% for 18%, 20%, and 22% S-SiO_2 loadings, respectively (Figure 23). Furthermore, the polarization curves for both electrode types have shown a clear potential drop in the kinetic region at low current densities for S-SiO_2 compared with that of S-SiO_2-T electrodes. This can be partially related to the high-water uptake possessed by P(VDF-TrFE) compared to PVDF which serves in further lubrication of the electrode in a dry medium. As a result, higher maximum power density retention was interestingly recorded for P(VDF-TrFE)-based fibrous electrodes at partially humidified (60% RH) conditions and thus outperforming PVDF-based fibrous electrodes.

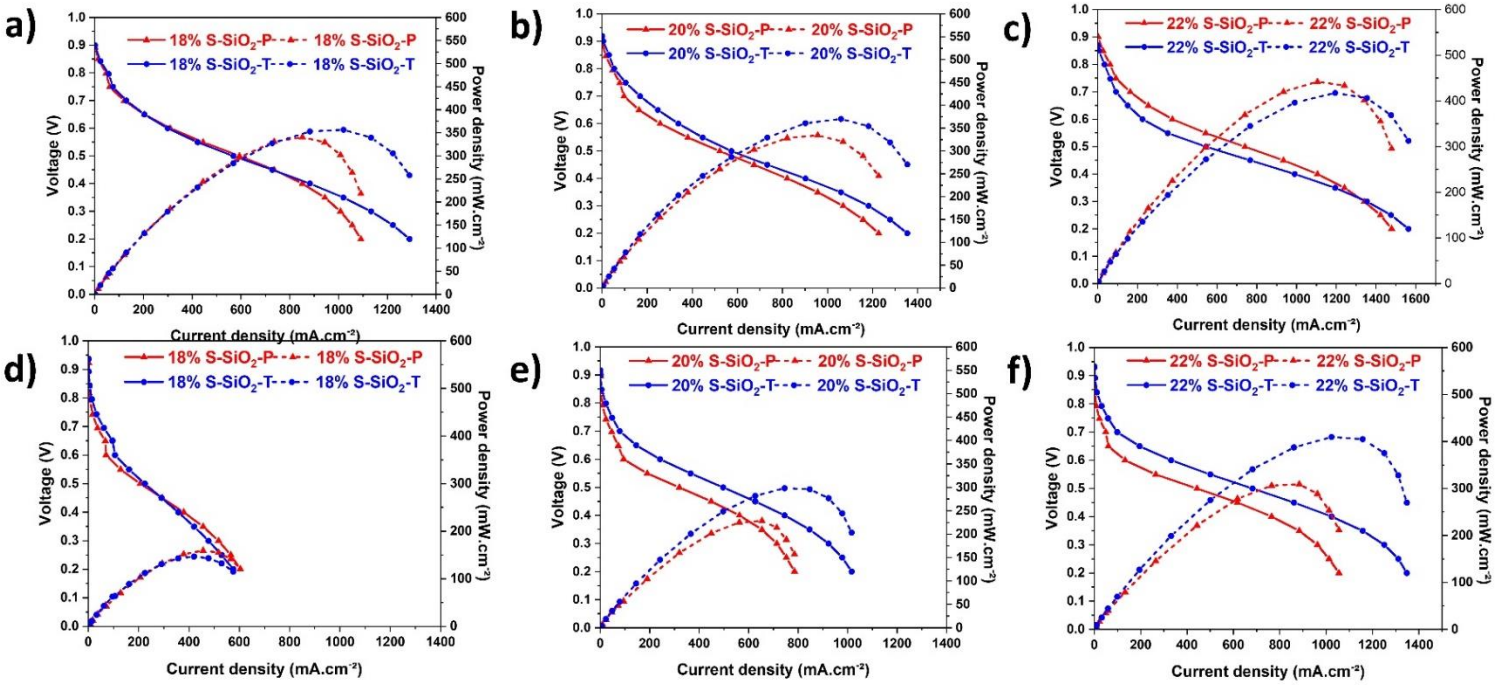

Figure 23: Polarization curves of MEAs containing a) 18% S-SiO_2-P and 18% S-SiO_2-T , b) 20% S-SiO_2-P and 20% S-SiO_2-T, and c) 22% S-SiO_2-P and 22% S-SiO_2-T at 100% RH , and d) 18% S-SiO_2-P and 18% S-SiO_2-T , e) 20% S-SiO_2-P and 20% S-SiO_2-T, and f) 18% S-SiO_2-P

Pt dissolution AST of 20% Naf-P and S-SiO_2-T fibrous electrodes are shown in Figure 24a, and Figure 24b, c, and d, respectively. The open-circuit voltage (OCV) has shown an increase for all electrodes after cycling. The rise in OCV was of more significance for electrodes of higher S-SiO_2/P(VDF-TrFE) recording a 9.47% increase for 22% S-SiO_2-T compared to a 3.15% increase for 18% S-SiO_2-T fibrous electrodes (Figure 24b, c, d, and Table 3). In turn, this has resulted in a general increase in performance in the low to mid-current density regions. In contrast, all electrodes exhibit a decrease in overpotential at low current densities. In this regard, it is not feasible to compare the ORR kinetics after cycling. Therefore, to have a closer look at the evolution of the different processes. Expectedly, the Nyquist plot 20% Naf-P shows an increase in the charge transfer resistance ($R_{ch,t}$) at 200 $mA.cm^{-2}$ (Figure 24e). However, 18% S-SiO_2 and 20% S-SiO_2 electrodes (Figure 24f, g) have shown a drop in the charge transfer resistance ($R_{ch,t}$) of 33.79%, 22.09% marking an enhancement of ORR kinetics while no significant change was observed for 22% S-SiO_2-T (Figure 24h). At first glance, the drop in $R_{ch,t}$ seems to be unlikely since generally, water build-up in the electrode serves in accelerating Pt dissolution/agglomeration, thereby increasing the size of Pt particles. Therefore, proton conduction is altered due to the reduction

in Pt/S-SiO_2 contact area [146]. Especially that, the ECSA measurements collected before and after cycling (Table 3) show an overall decline indicating a reduction in the Pt/S-SiO_2 interface. However, it is worth noting the reduction in the Pt/S-SiO_2 interface resulting from Pt dissolution/agglomeration occurs in parallel to an expansion in the Pt/water interface due to the degradation of the carrier polymer. The latter stems from the better proton conductivity resulting in enhanced ORR kinetics as discussed in a number of studies [61, 141]. This was especially clear upon comparing S-SiO_2-T electrodes with 20% Naf-P which has shown a 15.07% increase in $R_{ch,t}$ after 30000 cycles. Furthermore, the water contact angle measurement (WCA) at the surface of the fiber-based GDEs further solidifies the claim (Figure 23) where electrodes with higher S-SiO_2 showed a lower average contact angle. This implies that greater hydrophilicity imposed by greater S-SiO_2 loadings provides additional proton conduction pathways through the Pt/water interface. On the contrary, electrodes with excessive hydrophilicity are more prone to water flooding leading to deterioration in performance at high current densities. That is, during cycling, the oxidative stress and radical formation provoke a probable degradation in the hydrophobic P(VDF-TrFE) subjecting the electrode to greater water retention, especially in electrodes with high S-SiO_2 loadings [147]. This was evident upon comparing 22% S-SiO_2-T with 20% S-SiO_2-T in which the former lags behind the latter in the high current density region. To track the P(VDF-TrFE) degradation during cycling, SEM micrographs were collected for each electrode before and after performing the Pt dissolution AST, respectively (Figure 26). As expected, carrier polymer degradation was evident through the drop in fiber diameter for all three electrodes after 30000 cycles. In addition, a significant inter-fiber pore collapse was observed after Pt dissolution AST. The collapse of the pore structure mitigates water expulsion resulting in electrode flooding which is accompanied by an apparent drop in performance at higher current densities [148]. In addition, the dramatic increase in the mass transfer overpotential after 30000 cycles at elevated S-SiO_2 loadings draws our attention to the significance of S-SiO_2 migration throughout the process. The migrating S-SiO_2 can interact with the carbon support through covalent bonding with the carbon surface as stated by Bradley et al [1]. Therefore, although the agglomerating S-SiO_2 stabilizes both Pt and the carbon support but can block oxygen access and water expulsion pathways resulting in further resistive mass

transport. As an overall performance, the electrodes recorded promising retention in maximum power density up to 86.5% after 30000 cycles of Pt dissolution AST.

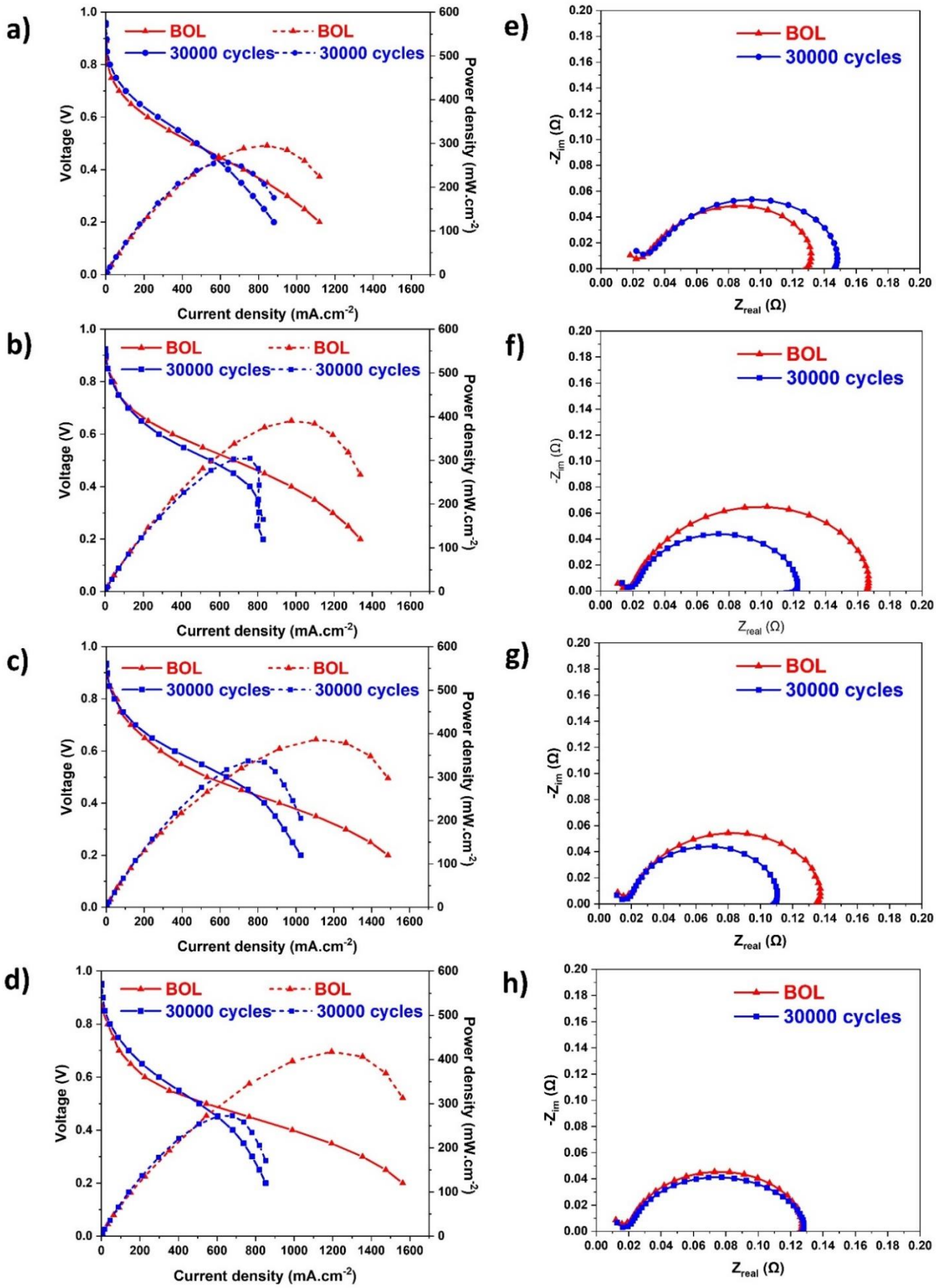

Figure 24: Fuel cell polarization curves and Nyquist plots collected at 200 mA.cm^{-2} current density of a,e) 20% Naf-P b,f) 18% S-SiO_2-T, c,g) 20% S-SiO_2-T, and d,h) 22% S-SiO_2-T at beginning of life (BOL), and after 30000 cycles of a Pt dissolution, AST performed at fully humidified conditions (100%RH).

Table 3: The open-circuit voltage (OCV), electrochemical surface area (ECSA), and the maximum power output of S-SiO_2-T of different S-SiO_2/P(VDF-TrFE) content at BOL and EOL of the electrode via Pt dissolution accelerated stress test.

Electrode	**BOL**			**30000 cycles**		
	OCV (V)	**ECSA ($m^2.g_{Pt}^{-1}$)**	**Maximum power density ($mW.cm^{-2}$)**	**OCV (V)**	**ECSA ($m^2.g_{Pt}^{-1}$)**	**Maximum power density ($mW.cm^{-2}$)**
18% S-SiO_2-T	0.889	44.5	390.64	0.917	32.3	304.16
20% S-SiO_2-T	0.890	49.95	386.47	0.930	45.3	334.40
22% S-SiO_2-T	0.866	52.61	417.43	0.948	47.8	272.76

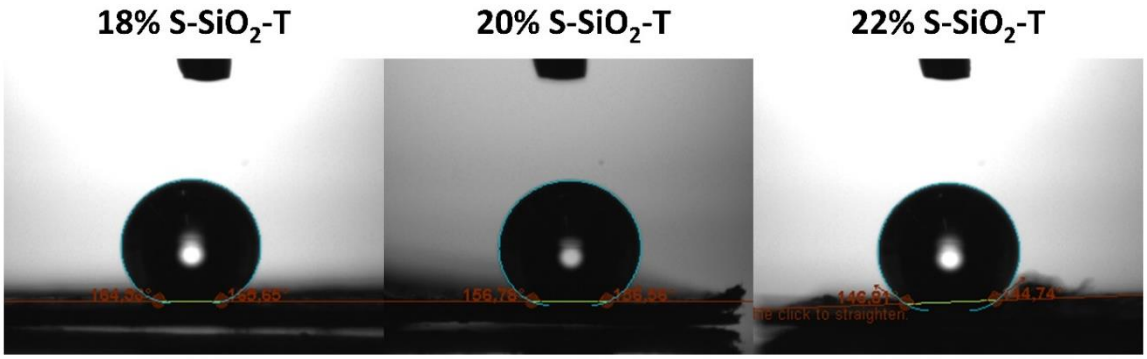

Figure 25: Contact angle measurement of 18% S-SiO_2-T, 20% S-SiO_2-T, and 22% S-SiO_2-T electrodes at BOL.

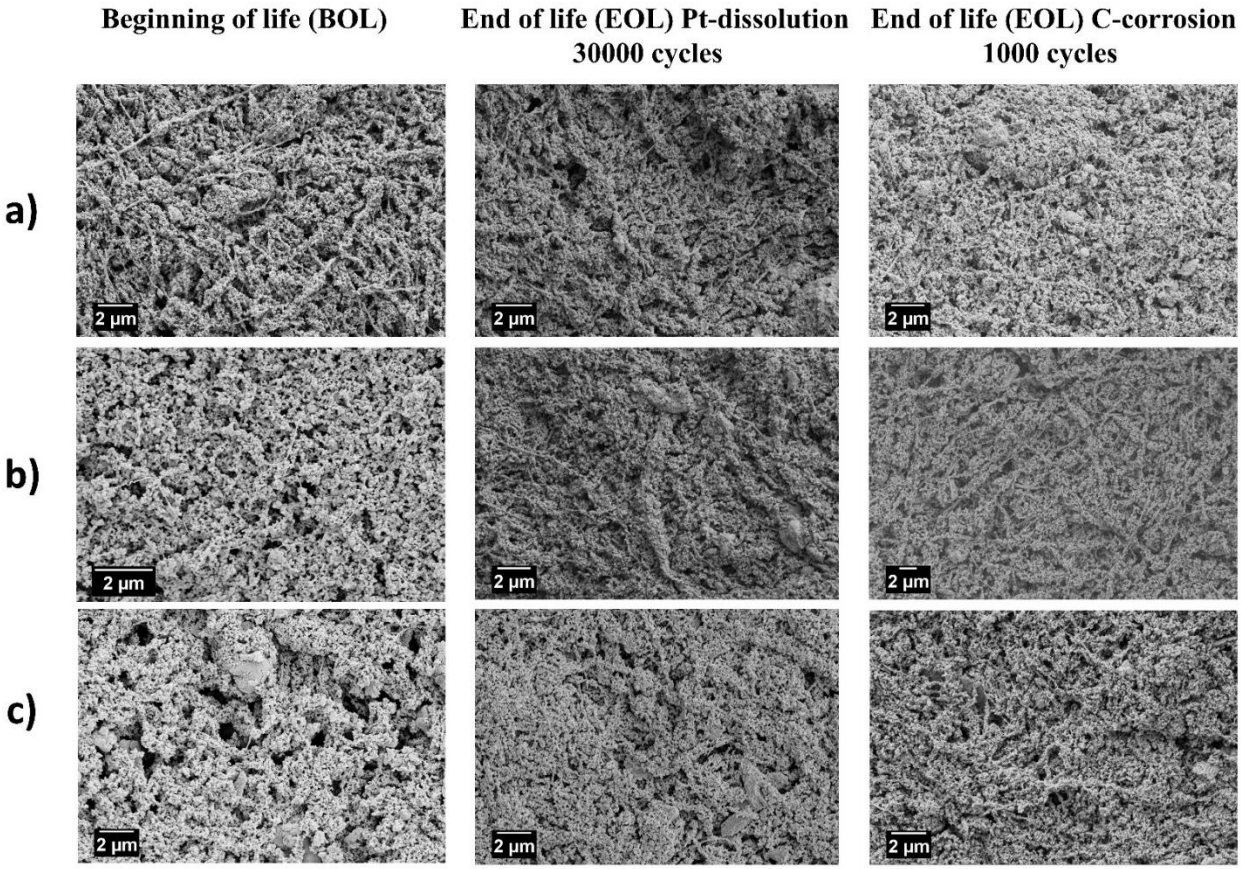

Figure 26: SEM images of a) 18% S-SiO_2-T b) 20% S-SiO_2-T and c) 20% S-SiO_2-T at (BOL), (EOL) after Pt dissolution and carbon corrosion AST.

Carbon corrosion ASTs were conducted for S-SiO_2-T electrodes of different S-SiO_2/P(VDF-TrFE) content to investigate the carbon support corrosion and its impact on the activation overpotential and the performance of the MEA. The MEA was cycled in the 1.0-1.5V (Figure 8). Within the selected voltage window, all Pt surface is fully oxidized, and thus, Pt dissolution contributes minimally to the loss in performance.[141] Again, an increase in OCV values hid the activation overpotential loss at the low current density region (Figure 27a,b,c) leading to an increase in performance at voltages below 0.5V. On the other hand, a significant drop in performance was evident in the high current density regions. However, it is observed that the extent to which the electrode shows a decline in performance in the mass transfer region varies on the variation of the S-SiO_2/P(VDF-TrFE) content. 18% S-SiO_2-T and 20% S-SiO_2-T electrodes present a steep drop in their performance curve in the high current density region. Consequently, the SEM images of the respective electrodes at both

BOL and EOL show a general decrease in the fiber diameter, and a partial collapse in the pore structure of the electrode (Figure 26a,b,c). Concurrently, an overpotential drop in the low current density region can again be directly correlated to the degradation of polymer content in the electrode leading to the building up of water on the surface of the catalyst. As a consequence, electrodes with higher hydrophilic S-SiO_2 content experienced a lower voltage loss in the low current density region. In addition, within the current cycling conditions, oxide groups form on the surface of the carbon support causing further hydration [61, 149]. The water buildup on the catalyst surface can hinder oxygen from reaching the active sites. On the catalyst level, the electrochemical surface area (ECSA) performed in dry conditions has shown a decline for all electrodes. Noticeably, electrodes with the highest S-SiO_2/P(VDF-TrFE) ratio suffered the most severe loss of 11.46 $m^2.g_{Pt}^{-1}$ compared to 9.13 $m^2.g_{Pt}^{-1}$ of 20% S-SiO_2-T and 2.93 $m^2.g_{Pt}^{-1}$ for 65% 18% S-SiO_2-T (Table 4). This can originate from the intrinsic interaction occurring between P(VDF-TrFE) carrier polymer and the carbon support. Therefore, the interaction partially inhibits carbon oxidation resulting in prolonging the lifetime of the electrode. [124] All in all, 18% S-SiO_2-T and 20% S-SiO_2-T electrodes demonstrated a respective decrease of 7.89 % and 5.34% in their maximum power output. However, remarkably, 22% S-SiO_2-T electrode exhibited a 2.70 % increase in its maximum power output after carbon corrosion AST.

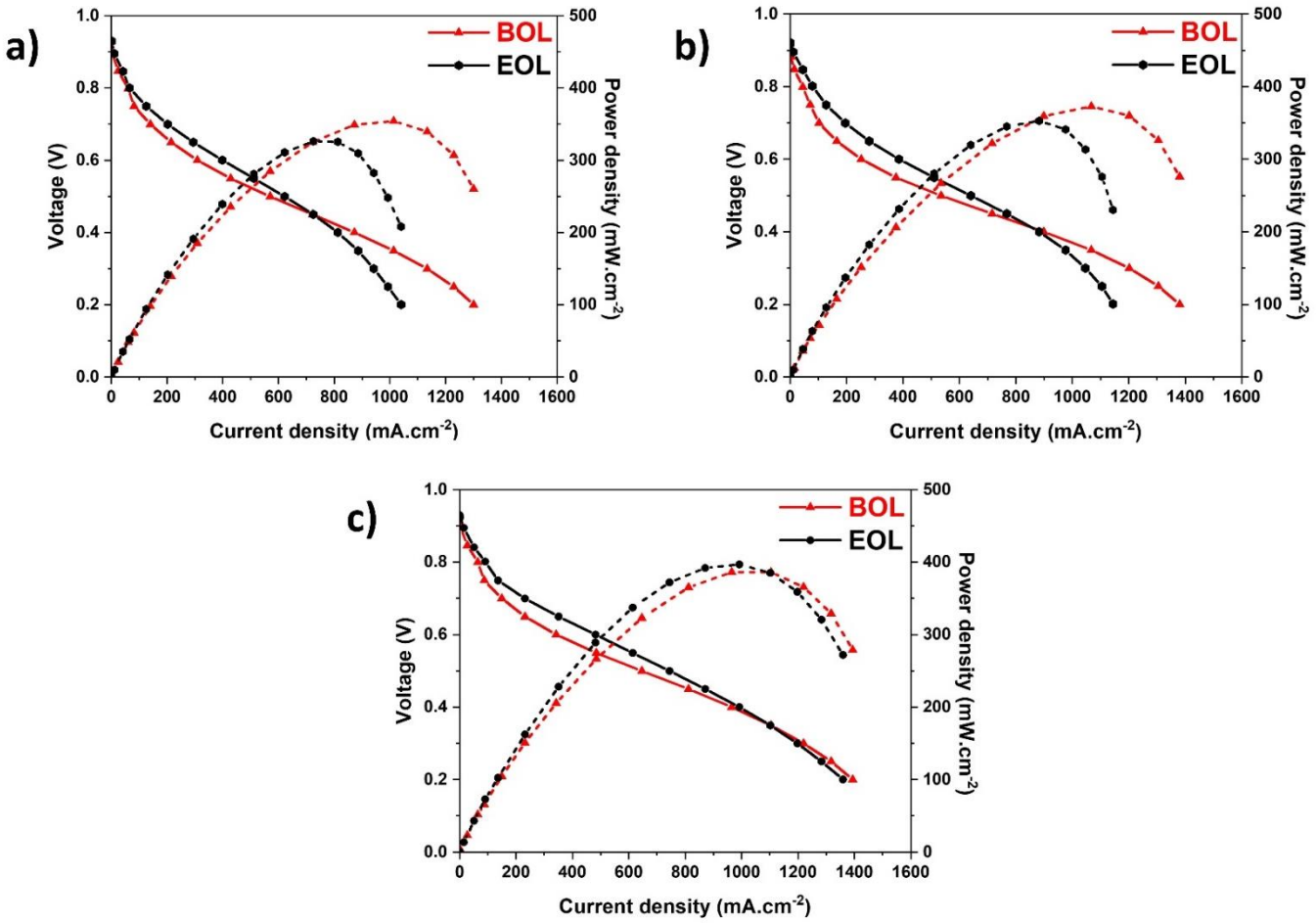

Figure 27: Fuel cell polarization curves a) 18% S-SiO_2-T, b) 20% S-SiO_2-T, and c) 22% S-SiO_2-T fibrous electrodes at beginning of life (BOL) and end of life (EOL) of carbon corrosion stress test performed at fully humidified conditions (100%RH).

Table 4: The open-circuit voltage (OCV), electrochemical surface area (ECSA), and the maximum power output of S-SiO_2-T of different S-SiO_2/P(VDF-TrFE) content at BOL and after 1000 cycles of carbon corrosion accelerated stress test.

Electrode	**BOL**			**1000 cycles**		
	OCV (V)	**ECSA ($m^2.g_{Pt}^{-1}$)**	**Maximum power density ($mW.cm^{-2}$)**	**OCV (V)**	**ECSA ($m^2.g_{Pt}^{-1}$)**	**Maximum power density ($mW.cm^{-2}$)**
18% S-SiO_2-T	0.899	42.92	354.18	0.928	41.57	326.22

20% S-SiO_2-T	0.882	44.93	372.82	0.919	35.80	352.89
22% S-SiO_2-T	0.900	52.61	386.1	0.921	41.15	396.82

3.4. Conclusions

The present study introduced the fabrication of novel electrospun S-SiO_2-T electrodes via electrospinning technique, and the detailed analysis of their physical/electrochemical characteristics, fuel cell performance, and durability. The morphology of P(VDF-TrFE) Pt/C/S-SiO_2 fiber electrodes (S-SiO_2-T) has shown the impact of electrospinning on attaining a porous structure on both the intra-fiber and the inter-fiber level of the catalyst layers. In addition, TEM and EDS mapping results have shown the homogeneous distribution of both Pt and S-SiO_2 particles along the fibers. Moreover, S-SiO_2-T fiber-based electrodes have shown highly porous morphologies reaching 72.76%. The fuel cell performance test of S-SiO_2-T fibrous electrodes (417.4 $mW.cm^{-2}$) has significantly overcome the conventional sprayed electrode (246.3 $mW.cm^{-2}$) shedding light on the impact of the fibrous architecture on the performance of the electrode. Furthermore, the electrodes have shown comparable power output to that of Nafion®-based fibrous electrode (Naf-P) (427.2 $mW.cm^{-2}$). Markedly, S-SiO_2-T fibrous electrodes have shown better performance, especially at partially humidified (60 % RH) conditions compared to S-SiO_2-P fibrous electrodes. Moreover, S-SiO_2-T electrodes have shown a maximum power density retention reaching 86.5 % comparable to fiber-based electrodes employing Nafion® (86.9 %) after 30000 Pt-dissolution AST cycles. Furthermore, the S-SiO_2-T fibrous electrodes have shown almost insignificant carbon corrosion resulting in an overall enhancement in performance after 1000 cycles of carbon AST for the aforementioned electrode. In conclusion, very promising fiber structure and fuel cell performance and durability were achieved for the first time in literature after combining P(VDF-TrFE) and S-SiO_2 particles in a fibrous electrode via electrospinning. This study shows that sulfonated silica is a better alternative to Nafion®, especially when working under partially humidified fuel cell testing conditions.

CHAPTER 4: CEO_2 NANOROD DECORATED NrGO ADDITIVES FOR BOOSTING PEMFC PERFORMANCE

The objective of this chapter is to synthesize nanorod-CeO_2 and nanorod-CeO_2/NrGO hybrid and to characterize them fully chemically and morphologically. Furthermore, it is intended to study the effect of nanorod-CeO_2 and nanorod-CeO_2/NrGO hybrid on both the ORR activity and the overall fuel cell performance of the cathode.

4.1. Introduction

Ceria (CeO_2) has been partaking in numerous catalytic applications due to its excellent redox property, providing the ability to easily shift Ce^{4+} to Ce^{3+}. This leads to a change in oxidation states and the number of oxygen vacancy defects by minimal activation energy. The catalytic property of CeO_2 is directly related to its oxygen storage capacity (OSC) which stands for the quantity of oxygen vacancies that a crystal structure is capable to host [150]. In this sense, multiple and different morphologies of CeO_2 (octahedra, microplates, nanorod, nanotubes, and nano cubes) have been synthesized [151],[152],[78]. CeO_2 nanoparticles usually accommodate octahedral morphology consisting of (111) crystal planes to minimize its surface energy. On the other hand, CeO_2 nanorods and nanocubes are enclosed by (110) and (100) planes [153]. The catalytic activity is mainly determined by the crystalline morphology. Therefore, different coordination and oxygen mobility possessed by each crystal plane dictates the activation energy for oxygen vacancy formation. For instance,

less activation energy is required for the formation of oxygen vacancies on the (110) plane compared to that of (100) planes. Furthermore, the (111) crystal plane comprises the highest oxygen vacancy formation activation energy [77]. Nanorods comprise the highest oxygen vacancy sites among other morphologies that leads to a significant enhancement in the catalytic activity of the material without involving any change in its composition. According to Wu et al. [154], nanorods exhibit more oxygen vacancies than nanocubes, which could be a proof that CeO_2 nanorods might be a promissing choice for catalytic activities, among other CeO_2 nanostructures, for oxygen reduction reactions (ORR).

Carbonaceous materials have been widely utilized as the main support material for metal oxides and different types of catalysts. This is a consequence of their high specific surface area, porous structure, and electronic conductivity properties providing synergetic effect and better efficiency in redox reactions [[155], [156], [29], [157]]. In this regard, nitrogen-doped reduced graphene oxide (NrGO) has proven to improve the kinetic for oxygen reduction reaction (ORR), as reported by Ping Chen et al.[158, 159]. However, bare carbon materials tend to degrade the cathode and electrolyte by causing the formation of parasitic products which passivate the active catalytic sites. For that reason, carbon-free materials like metal oxide catalysts and their composites with carbon materials were studied to balance reaction kinetics and decrease the site reactions [160].

Transition metal oxides have shown to be promising additives enhancing ORR activity of the electrodes in PEM fuel cells [[161], [162], [163]]. Recently, CeO_2 is generally used as the catalyst support [87], additive [85, 164] and radical scavenger [86] for fuel cells. Ehlinger et al. studied modeling of PEMFC in which cerium ions were used to increase the lifetime of the MEA. Cerium ion scavenged radicals from gaseous reactants, reducing chemical degradation [165]. In another work, Ostroverkh et al. deposited a set of layered forms such as nitrogenated carbon, Pt, and CeO_2 on the gas diffusion layer (GDL) by sputtering. The resulting material showed an improved and stable fuel cell performance compared to bare Pt/C [166]. In order to prevent the chemical degradation within the MEA, Breitwieser et al. sprayed graphene oxide/CeO_2 (GO/CeO_2) composite powder in between Aquivion ionomer layers. As a result short circuits were eliminated, and the current density resulting from probable hydrogen crossover was reduced [167].

Lim et al. dispersed CeO_2 nanoparticles on commerical Pt/C catalyst, and their results exhibited a better performance compared to bare Pt/C owing to the fast transition between Ce^{3+} to Ce^{4+} and its high oxygen storage capacity [79]. Mori et al. proved that Pt activity was improved in Pt–CeO_x/C cathodes compared to Pt/C during ORR in PEMFC. It was suggested that the defect formation within the Pt–CeO_x interface enhanced the Pt catalytic activity in ORR [168]. A nitrogenated carbon (CN_x) layer was deposited on GD then Pt–CeO_y layer was additionally coated on the final layer by Nováková et al. Their results showed that the presence of a CN_x interlayer as a support to Pt–CeO_y yielded higher power density compared to a cathode without the CN_x layer [169]. Chourashiya et al. utilized a one-step solution combustion fabrication method to fabricate Pt/CeO_2 composites for a higher activity as ORR catalyst [170]. CeO_2 nanoparticles were embedded into MEAs by Pearman et al. [86] and resulted in a decrease in voltage decay by enhancing membrane stability with a stable hydrogen crossover, owing to the protecting and scavenging effect of CeO_2 in the membrane [86].

In this study, a thermal annealing method was used in favor of synthezing nitrogen-doped reduced graphene oxide (NrGO). This was performed by processing GO at high temperature in a continuous ammonia and argon gas flow. Then, CeO_2 nanorods were synthesized onto NrGO sheets with a facile hydrothermal synthesis step, and then mixed with a very low amount of commercial Pt/C (0.09 mg cm^{-1}). The final material was used as a hybrid catalyst structures for PEMFCs. By means of this approach, a promising fuel cell performance is targeted with low Pt loading in the catalyst layer. To the best of our knowledge, the designed hybrid catalyst (Pt/C–CeO_2/NrGO) in this study was employed as a PEM fuel cell catalyst for the first time in the literature.

4.2. Experimental Procedures

4.2.1. Materials

Natural graphite flakes (99%), potassium permanganate ($KMnO_4$, 99%), sulfuric acid (H_2SO_4, 98%), phosphoric acid (H_3PO_4), hydrogen peroxide(H_2O_2), hydrochloric acid (HCl,

37%) were purchased from Sigma–Aldrich to synthesize graphene oxide. Cerium (III) chloride heptahydrate ($CeCl_3.7H_2O$, 99.99%), sodium hydroxide (NaOH, ≥97%), ethanol (C_2H_6O), and N-methyl-2-pyrrolidone (NMP, 97%) were provided from Sigma–Aldrich as well for CeO_2 nanorod fabrication. Carbon paper (AvCarb MGL190), carbon black (Vulcan XC-72), and 40% Pt/Vulcan XC-72R were purchased from the Fuel Cell Store. Ultrapure 2-Propanol (≥99.5%) was purchased from Isolab chemicals. Analytical grade reagents were used as purchased without any further purification.

4.2.2. Graphene oxide (GO) synthesis

Graphene oxide was synthesized through Hummer's method. As a first step, a solution of Graphite flakes and $KMnO_4$ was prepared via mixing followed by the addition of H_2SO_4 and H_3PO_4. Under a reflux, the resulting mixture was kept for 24 hours under continuous stirring at 70 rpm and 50 °C temperature. After obtaining a brownish colored slurry, the solution was cooled down in an ice bath. Then, hydrogen peroxide (H_2O_2) and hydrochloric acid (HCl) were added in respective manner. The suspension was then diluted by adding DI water and kept for 48 h in the ice bath. As a result, A well dispersed, homogenous, yellowish, acidic suspension of GO was obtained. Multiple washing steps using water/ethanol were performed in order to neutralize the medium. Finally, GO flakes were obtained through freeze drying the solution.

4.2.3. Nitrogen-doped reduced graphene oxide (NrGO) synthesis

The synthesis of NrGO has undergone using an ammonia gas ambient atmosphere-based thermal annealing reported elsewhere in the literature [171]. In brief, the obtained GO was placed in a tube furnace and heated up to 900^{o}C under ammonia and argon purging atmosphere. Then, NrGO was collected after cooling the system to room temperature while maintaining a constant argon flow.

4.2.3.1. CeO_2 nanorod synthesis

CeO_2 nanorods were synthesized through a hydrothermal method. Initially, 5 mmol of cerium (III) chloride heptahydrate were added into an already prepared 9M NaOH solution in 100 mL of DI water and stirred constantly for 15 min. the solution heated in a 200 mL Teflon container tightly sealed in a stainless-steel autoclave at 100^oC for 48 hours. After cooling the solution, it was filtrated using a Buchner setup and washed with DI water to neutralize the ph. The obtained CeO_2 nanorods were left to dry for 12 h.

4.2.3.2. CeO_2/NrGO synthesis

Similarly, Nitrogen-doped reduced graphene oxide supported CeO_2 nanorods (CeO_2/NrGO) were prepared via hydrothermal method. Into a DI water/ethanol/ NMP solution NrGO and CeO_2 nanorod were added to prepare a 3 g/L and 4.5 g/L dispersions, respectively. This was followed by the addition of NaOH (4.5M) before moving the final suspension into a Teflon-lined stainless-steel autoclave at a temperature maintained at 100 °C for 12 h. After cooling, the product was washed with DI water, collected through centrifugation, and left to dry for 12 hours.

4.2.4. Preparation of membrane-electrode-assembly

Pt/C–CeO_2, Pt/C–CeO_2/NrGO, Pt/C were prepared by mixing Pt/C with the additive (CeO_2 and CeO_2/NrGO) into which 20% Nafion® solution was added followed ultrapure 2-propanol. The inks were sonicated in an ice water bath for 1 h and stirred for an additional 2 h. Electrodes (Table 5) were prepared by air spraying the inks onto a 5 cm^2 carbon paper and dried at 60 °C in an oven.

Table 5: Catalyst layer content of the as prepared electrodes

Electrodes	Pt content ($mg.cm^{-2}$)	CeO_2 nanorods content ($mg.cm^{-2}$)
1	0.09	0.2
2	0.09	0.2
3	0.09	_
4	0.3	_

4.2.5. MEA Preparation

The sprayed electrodes (electrodes 1, 2, and 3) were assembled in an MEA against an anode of 0.3 $mg_{Pt}.cm^{-2}$ (electrode 4) sandwiching a 221 Nafion® membrane. The assemblies were hot-pressed under a force of 0.5 tons and at 134 °C temperature.

4.2.6. Electrochemical Characterizations

A three-electrode electrochemical cell, which consisted of Pt/C, Pt/C–CeO_2 and, Pt/C–CeO_2/NrGO as working electrode (WE), Ag/AgCl as reference electrode (RE), and Pt wire as a counter electrode (CE), along with a rotating disc electrode (RDE) setup (Gamry Instruments Reference 3000 Potentiostat/Galvanostat/ZRA and Pine rotating control) were employed for electrochemical activity evaluations. An electrolyte solutions of 0.1 M $HClO_4$ were prepared and purged respectively with N_2-purged and O_2-purged for 30 min. Then, cyclic voltammetry (CV) and linear sweep voltammetry (LSV) data were collected. The ink was simply prepared by mixing a catalyst (Pt/C and Pt/C-additive (CeO_2 and CeO_2/NrGO), DMF:2-propanol (1:4 v/v) solution, and Nafion® solution (20%) (50:1 w/w) as previously reported in our studies [37,38]. Onto the surface of a previously polished glassy carbon electrode, dropwise addition of 10 μL of ink solution was done until obtaining 20 $\mu g_{Pt}\ cm^{-2}$ catalyst loading for each sample. All measurements were collected at room temperature. To prepare a homogenous ink, 10 μL of the resulted ink was drop cast onto glassy carbon electrodes, with the surface area of 0.19625 $cm^{2,}$ and then dried in an oven at

60 °C. For the cyclic voltammetry (CV) tests and ORR studies, the same experimental parameters were adopted as our previous studies [172-174]. All measured potentials in CV and LSV experiments were converted to the reversible hydrogen electrode (vs. RHE) scale in accordance with the Nernst equation.

Fuel cell performance and durability tests were performed using a Scribner 850e series with controlled temperature, input flow, and backpressure. MEAs of 5 cm^2 were first conditioned at a fixed cell temperature of 80 °C, and fully humidified hydrogen and air inputs of respective 0.125 mL/h and 0.5 mL/h flow rates. The performance of the cathode was examined by collecting the polarization curves at fully humidified conditions, fixed cell temperature of 80 °C and 25 psi backpressure

4.3. Results and Discussion

To evaluate the ORR performance of the samples, LSV tests were done by employing a rotating disc electrode (RDE) at 100, 400, 900, 1600 rpm, and 2500 rpm in all samples (Figure 28b, c, and d). Figure 28e, a mixed kinetic diffusion-controlled region appeared from

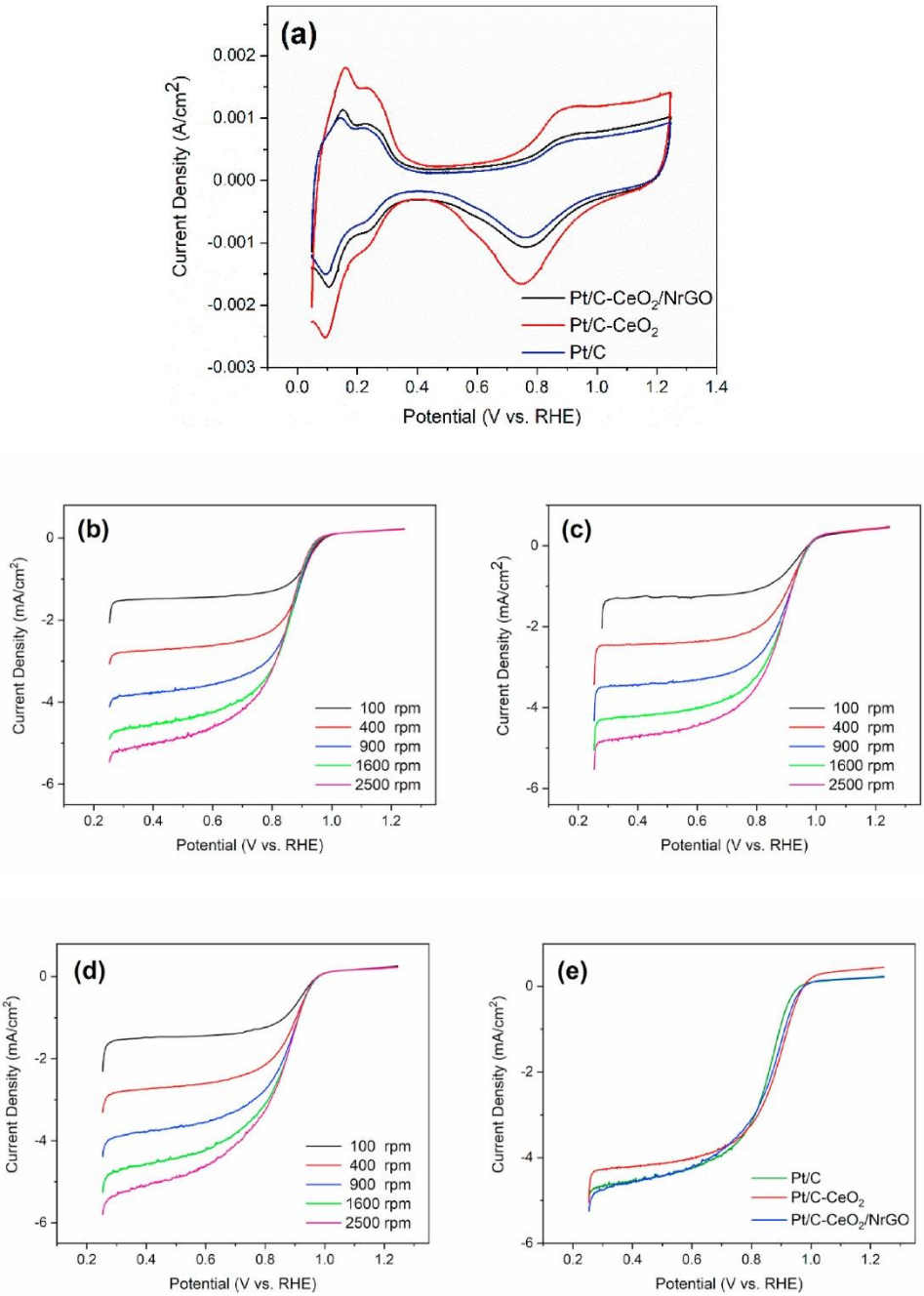

Figure 28:(a) Cyclic voltammetry of Pt/C, Pt/C–CeO_2 and Pt/C–CeO_2/NrGO, hydrodynamic voltammograms recorded between 100 and 2500 rpm with 10 mV/s scan rate of (b) Pt/C, (c) Pt/C–CeO_2, (d) Pt/C–CeO_2/NrGO, and (e) comparison graph at 1600 rpm.

0.8 V to 0.95 V. Therefore, the potential of 0.9 V was chosen to calculate the mass activity. Like the CV results, a difference between the samples' activity was observed (Figure 28e). The mass activity and half-wave potentials of the samples containing additives compared to commercial Pt/C catalyst showed a significant increase after CeO_2 addition. This improvement in ORR performance could be due to the introduction of local oxygen sites over the Pt surface. Besides, the half-wave potential ($E_{1/2}$) of Pt/C–CeO_2 is also obviously higher than that of Pt/C and Pt/C–CeO_2/NrGO (Table 6). This might be explained by the higher oxygen storage ability of CeO_2, that could also increase oxygen concentration over Pt surface [79, 150, 175-178]. These results might be attributed to a high level of oxygen vacancies which exist in CeO_2 nanorod.

Table 6: ECSA, half-wave potential ($\Delta E_{1/2}$), mass activity values of the Pt/C, Pt/C-CeO_2 and Pt/C-CeO_2-NrGO

Sample	**ECSA ($m^2.g^{-1}$)**	**Mass Activity @ 0.9 V ($A.mg^{-1}$)**	**$\Delta E_{1/2}$ @ 1600 rpm (V)**
Pt/C	82	0.044	0.871
Pt/C-CeO_2	141.0	0.107	0.898
Pt/C-CeO_2-NrGO	89	0.051	0.886

A closer look into the polarization curves of the three electrodes shows that Pt/C exhibited a more significant loss in the activation region (0.58 V at 200 $mA.cm^{-2}$) compared to the CeO_2/NrGO and CeO_2 CeO_2/NrGO (0.63 V and 0.65 V respectively at 200 $mA.cm^{-2}$) included electrodes (Figure 29). This can be attributed to a more sluggish ORR kinetics for the Pt/C electrode. In other words, the addition of a CeO_2-containing additive into the electrode composition serves in boosting the ORR kinetics. However, Pt/C–CeO_2/NrGO based electrode performed slightly better than the Pt/C–CeO_2 electrode. This can be related

to the additional electrical conductivity imposed by the NrGO substrate resulting in lower bulk resistance (R_e). The addition of the electrically insulating CeO_2 caused an increase in the bulk resistance (R_e) of the electrode. However, incorporating CeO_2 with a conductive substrate brought the bulk resistance back down, serving in boosting the performance of the electrode. Another noticeable feature is the better performance of Pt/C–CeO_2/NrGO at high current density (0.4V at 1000 mA.cm^{-2}) compared to Pt/C–CeO_2 (0.37 V at 1000 mA.cm^{-2}). Pt/C–CeO_2 showed a decline of voltage at high current densities due to the hydrophilic behavior of CeO_2, causing the accumulation of water in the electrode.

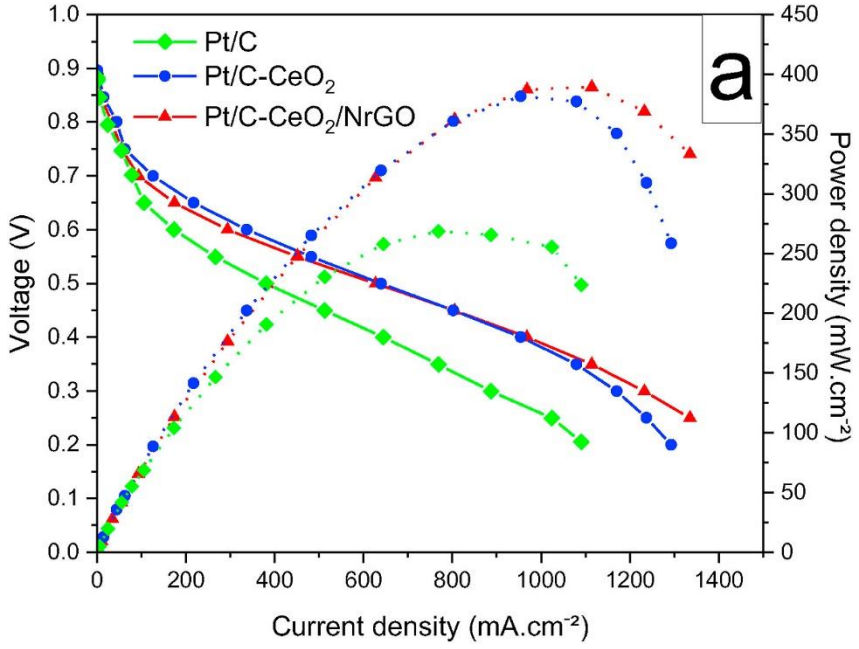

Figure 29: Fuel cell polarization curves and power output of Pt/C–CeO_2/NrGO, Pt/C–CeO_2, and Pt/C

4.4. Conclusions

In this work, we have reported the synthesis of new cathode additives for PEMFCs, CeO_2 nanorods and the CeO_2/NrGO composite and investigated their physical and electrochemical characteristics for the first time in literature. The CeO_2 and CeO_2/NrGO

composite material were mixed with ultra-low amount of commercial Pt/C (0.09 $mg.cm^{-1}$), and then, hybrid catalysts were used in PEMFC's cathode. Pt/C–CeO_2 and Pt/C–CeO_2/NrGO hybrid catalysts showed superior HOR, and ORR activity compared to the commercial Pt/C. The nanorod morphology of CeO enabled oxygen vacancies within its structure with a very low transition energy barrier between Ce^{3+} and Ce^{4+}. All evidence in this study pointed out that CeO_2 nanorods had a significant improvement on the ORR activity of the hybrid catalysts, as a result of the fast transition between the oxydation states. ORR activity is significantly higher for Pt/C–CeO_2 (mass activity: 0.107 $A.mg^{-1}$ at 0.9 V) compared to other samples due also to the excellent oxygen storage ability of CeO_2. It is therefore thought that the oxygen buffering ability of CeO_2 serves in enhancing the ORR kinetics on the surface of Pt. This in turn reflects better PEM fuel cell performance. This resulted in an overall improvement of the electrode in which the maximum output was recorded to 389 $mW.cm^{-2}$ as compared to 269 $mW.cm^{-2}$ for the conventional Pt/C based electrodes. CeO_2-based additives with nanorod morphology enriched the electron density to increase especially ORR activity of Pt catalyst so that very low amount of Pt loading yielded high power output.

CHAPTER 5: THE EFFECT OF CERIUM OXIDE PARTICLE MORPHOLOGY ON THE PERFORMANCE AND DURABILITY OF PEM FUEL CELL ELECTRODES

5.1. Introduction

In the previous chapter, nanorods of CeO_2 were investigated as electrode additives to boost the ORR kinetics. The results were no surprise as the introduction of CeO_2 nanorods doubled the ORR activity and thus the performance of the MEA. This was attributed to the oxygen buffering effect characteristic of CeO_2. However, the buffering effect and its accompanied oxygen capacity is subject to change with the change in crystallographic structure of the material. For instance, it was revealed that the [100] plane of CeO_2 nano cubes are characterized by enhanced oxygen buffering compared to [111]/ [100] of nanorods and polyhedral CeO_2 [179]. Therefore, the crystallographic structure of the added CeO_2 can affect the overall performance of the cathode. In this study, nano cubes of CeO_2 were prepared using a hydrothermal synthesis method. The nature of the CeO_2 was revealed using XRD while its adopted cubic morphology was visualized using SEM. In parallel, the surface area and the pore distribution was analyzed using BET. Gas diffusion cathodes were prepared via spraying with a fixed Pt loading (0.15 mg_{Pt}/cm^2) and a variable amount of CeO_2 nano cubes additive. The assembled MEA is tested to evaluate the impact of CeO_2 on the performance of the cathode. Furthermore, the stabilizing effect of CeO_2 nanocubes on Pt was investigated through performing a Pt-dissolution AST.

5.2. Materials

Cerium (III) nitrate hexahydrate ($Ce(NO_3)_3.6H_2O$, 99.99%), sodium hydroxide (NaOH, ≥97%),were purchased from Sigma–Aldrich. Carbon paper (AvCarb MGL190), carbon black (Vulcan XC-72), and 40% Pt/Vulcan XC-72R were purchased from the Fuel Cell Store. Ultrapure 2-Propanol (≥99.5%) was purchased from Isolab chemicals. Analytical grade reagents were used as purchased as received.

5.2.1. Cubic-CeO_2 Synthesis

Cubic-CeO_2 was synthesized through a hydrothermal process. First. 1.1 grams of Cerium (III) nitrate hexahydrate were added into a 40 mL solution of 6M sodium hydroxide and stirred for 1 hour. Then, the resulting solution was transferred into a 75 mL autoclave and heated for 24 hours (or 48 hours) at 200^{o}C. The resulting cubic-CeO_2 was washed and dried overnight at 60^{o}C.

5.2.2. Octahedral-CeO_2 Synthesis

In a typical hydrothermal process, 1 mmol of cerium nitrate ($Ce(NO_3)_3$) and 0.01 mmol of sodium phosphate (Na_3PO_4) were dissolved in 40 mL of distilled water and kept under constant stirring for 1 hour. The resulting solution is then moved into a sealed stainless-steel autoclave and kept under 170^{o}C for 12 hours. Finally, the produced octahedral-CeO_2 is washed multiple times with distilled water and kept drying overnight.

5.2.3. Morphological Analysis

The morphology of CeO_2 was visualized using scanning electron microscopy (SEM) using a German Jeol JSM 6010 LV and Supra 35VP Leo. The samples were coated with Au/Pt using a Cressington 108 sputter coater at 40 mA for 120 s. The images were taken with 3–5 kV accelerating voltage and an 8–9 mm working distance. Powder XRD analysis was performed using a Bruker D2 Phaser brand desktop X-ray diffractometer equipped with

copper radiation (Cu K_α = Kα λ = 1.540 Å). The diffraction patterns were obtained within 10–90° scanning range with 0.02° 2θ step size, and 1s for a single step. N_2 adsorption isotherm is collected at 77.3 K using a Micromeritics 3Flex Physisorption instrument to measure samples' specific surface areas and pore size distributions. Cubic-CeO_2 is degassed at 130 °C for 24 h preceding measurements. Measurements were done under an increasing Nitrogen gas relative pressure (0–0.99)

5.2.4. Membrane Electrode Assembly (MEA) Preparation

For the electrodes, gas diffusion electrodes (GDE) were prepared via air spraying with a fixed Pt loading of 0.3 mg cm^{-2} for the anode and 0.15 $mg.cm^{-2}$ for the cathode. For the anode, the inks were prepared in a vial by adding 0.15 g of 20% Nafion® solution onto 0.1 g of 30% Pt/C catalyst (40% Pt/C for the cathode) followed by the addition of 8 mL of isopropyl alcohol (IPA). For cathodes, cubic- CeO_2 was added with a variable ratio ($mCeO_2/m_{Pt/C}$). The solution was then sonicated for 1 h and then stirred for another 2 h. The GDEs were fabricated by the spraying of Pt/C/ Nafion® inks onto a Sigracet 39 BC carbon paper gas diffusion layer (GDL). Spraying was repeated to obtain the desired Pt loading. Each spraying step was followed by drying at 60 °C for 10 min. The anode, cathode, and a Nafion® membrane in between were then assembled. The MEA was first preheated for 10 min at 135 °C without applying any force, followed by another 5 min under 5 MPa.

5.2.5. Fuel Cell Tests and in Situ Electrochemical Analyses

Fuel cell performance tests and in situ impedance analysis were done using a Scribner Series 850e with controlled back pressure, temperature, and humidity conditions. All tests were conducted on a single cell composed of 5 cm^2 MEA and with single serpentine hydrogen gas and airflow channels. Initially, the MEA was conditioned by alternatively subjecting it to cycling voltages of 0.2 and 0.6 V until a stable current density was obtained. Throughout the process, an 80 °C cell temperature was maintained, and fully humidified hydrogen gas and air flows (0.125 L min^{-1} and 0.5 L min^{-1}, respectively) were fed at ambient

pressure. Prior to fuel cell polarization curve data collection, the system was maintained at 0.2 V to condition and stabilize the MEA. Then, fuel cell polarization curves were collected between 0.2 V and the open-circuit voltage (OCV) under fully humidified conditions. The cell was fed with H_2 at the anode and air at the cathode at respective flow rates of 0.125 L min^{-1} and 0.5 L min^{-1} air with 25 psi of backpressure.

Electrochemical impedance spectrograms (EIS) were collected under fully humidified conditions. Hydrogen and oxygen gases were stoichiometrically (1:1 ratio) supplied to the anode and cathode, respectively with a flow rate maintained at 0.125 $L.min^{-1}$. The data were collected through a sweeping frequency in the range of 0.1-10000 Hz with an AC amplitude being set to 40% of the applied DC current with 20 points collected per decade. Prior to data collection, the system was maintained at the selected current density for a span of 10 minutes in favor of stabilizing the system. Potentio-static EIS was performed at a fixed bias potential of 0.6V to evaluate the ORR resistance. The linearity of the EIS data was validated using linear Kramers-Kronig validity test software developed by the Karlsruhe Institute of Technology [132]. Finally, the resulting Nyquist plots were fitted and analyzed using Zview software.

Pt-dissolution accelerated stress tests (AST) were conducted in fully humidified (100% RH) H_2(anode)/N_2(cathode) atmosphere with flow rates of 0.125 $mL.min^{-1}$ and 0.25 $mL.min^{-1}$, respectively. Using an external potentiostat, the MEA was cycled with a square wave in an alternating fashion at 0.6 V and 0.95V for 3 seconds each repeated 30000 times. It should be noted that before and after the AST test, all data relevant to fuel cell polarization curves were collected.

5.3. Results and Discussion

The XRD pattern of the synthesized cubic-CeO_2 is shown in Figure 30. The main reference peaks at 28.68, 33.22,47.52, and 56.29^o corresponding respectively to the (111), (200), (220), and (311) planes match that of the obtained data. This indicates the successful synthesis of pure cubic phase CeO_2. Furthermore, the XRD data confirmed numerous similar studies further confirming the existence of cubic-CeO_2.

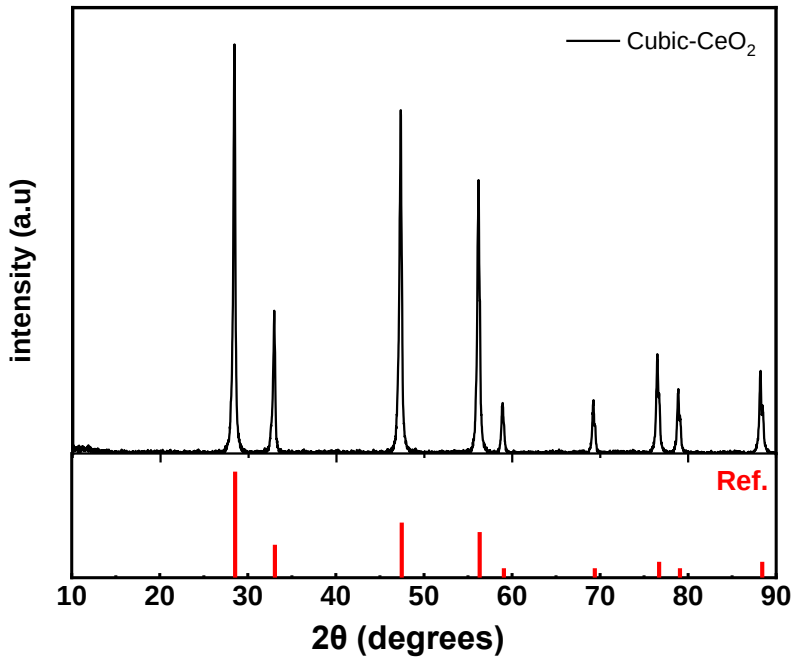

Figure 30: X-ray diffraction pattern of Cubic-CeO_2

The morphology of CeO_2 was visualized using SEM and shown in Figure 31. The SEM images show a clear formation of cubic nanoparticles. Despite the small size of the particles, the size distribution was not uniform. There exist smaller particles (in the 10-20 nm range) accompanied by larger particles (~ 50nm) (Figure 31a). The size of the particles presents crucial importance for the enhancement in the ORR activity. That is, smaller particles can exhibit a broader contact surface area with Pt. However, upon increasing the synthesis time, a growth in the cubic particles size was observed as shown in Figure 31b. The growth of the particles upon increasing the reaction time gives a clearer indication about the successful formation of cubic-CeO_2. In addition, octahedral-shaped CeO_2 were observed in Figure 31c within a 100-150 nm size range.

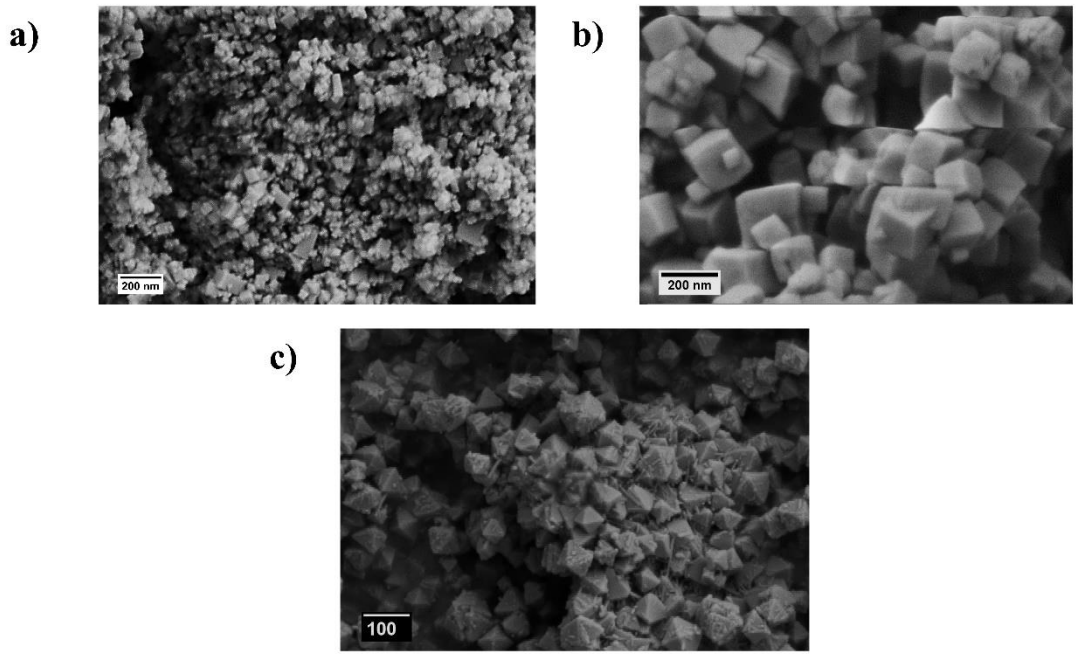

Figure 31: SEM images of cubic-CeO_2 synthesized for a) 24hours b) 48 hours and c) octahedral CeO_2

The surface area is considered one of the major parameters affecting the activity of CeO_2. Therefore, the surface area analysis was conducted for the synthesized cubic-CeO_2 (Figure 32, Table 7). The results have shown that cubic-CeO_2 exhibits a type III isotherm with a BET surface area of 15 $m^2.g^{-1}$. It is worth noting that the surface area of cubic-CeO_2 is lower than that of nanorod-CeO_2 reported in the previous study (52 $m^2.g^{-1}$). This can be attributed to the lower porosity exhibited by cubic-CeO_2 (0.08 $cm^3.g^{-1}$) compared to that of the former (0.3 $cm^3.g^{-1}$). However, cubic-CeO_2 exhibited a broader pore size distribution averaging 19.9 nm.

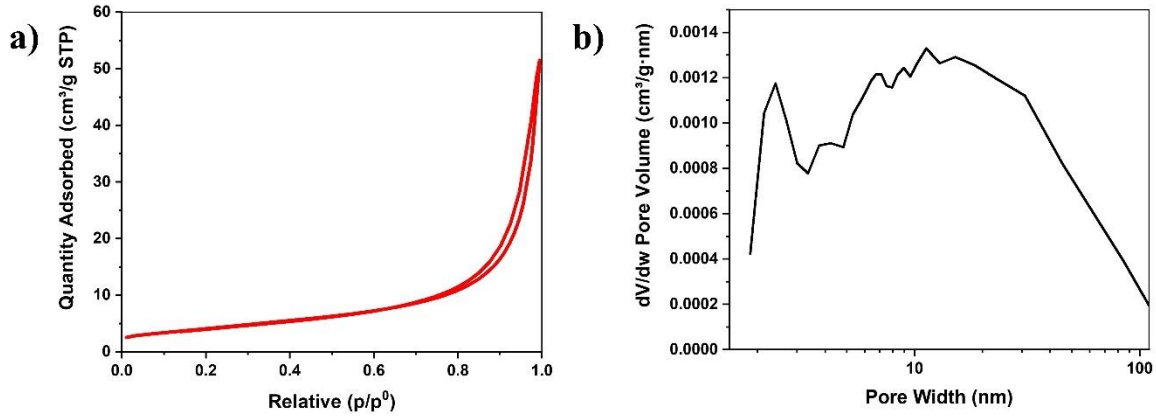

Figure 32:a) BET N_2 adsorption isotherms and b) corresponding pore size distribution of cubic-CeO_2

Table 7: BET analyses result of bare cubic-CeO_2

Sample	BET Surface Area ($m^2.g^{-1}$)	BJH Pore Volume ($cm^3.g^{-1}$)	BJH Average Pore Size (nm)
Cubic-CeO_2	15	0,08	19,9

The fuel cell performance of the electrodes containing a variable amount of cubic-CeO_2 are shown in. Similar to the previous chapter, the results clearly show an outperformance of electrodes containing cubic-CeO_2 compared to cathodes with no cubic-CeO_2. This further demonstrates the catalyst enhancement ability of cubic-CeO_2. To get a better understanding of the enhancement effect provoked by cubic-CeO_2, a closer look at the polarization curve at high voltages is needed. It is worth restating that kinetic overpotentials dominate the region of the polarization curve with high voltage. Therefore, it is adequate to compare the current density output at 0.6V. The result shows that introducing cubic-CeO_2 increases the current density at 0.6V from 204.7 $mA.cm^{-2}$ for 0% CeO_2 to 351.4 $mA.cm^{-2}$ for 10% CeO_2 marking a 41.7% increase. The effect of CeO_2 on the ORR was further solidified upon incorporating higher loads of cubic-CeO_2. The current density recorded at 0.6V increased dramatically up to 541.4 $mA.cm^{-2}$ marking an additional 35% boost in the ORR performance (Figure 33,Table 8). To take a closer look at the ORR activity, EIS measurements were conducted at 0.6V bias potential for cathodes containing 10% and 20% cubic-CeO_2. The Nyquist plots presented in Figure 34 show a clear advantage for increasing the cubic-CeO_2 content and their impact on the ORR activity. The fitted results exhibited a

0.138 Ω in the charge transfer resistance (R_{ORR}) for 10% CeO_2 loaded cathodes. However, upon increasing the CeO_2 content to 20%, R_{ORR} decreases drastically by half (50.7%) reaching 0.068 Ω. All in all, cathodes without any CeO_2 addition recorded a maximum power density of 293.82 $mW.cm^{-2}$. The power density was significantly boosted with CeO_2 additions recording 387.9 and 430.6 $mW.cm^{-2}$ for 10% and 20% CeO_2 additions (Table 8). The reported results coincide with the previously reported result in Chapter 4. However, the added cubic-CeO_2 corresponds only to 0.0375 $mg.cm^{-2}$ and 0.075 $mg.cm^{-2}$ for 10% and 20%. Compared to nanorod-CeO_2 loading used in the previous study. However, nanorod-CeO_2 boosted the performance by 29.85%. on the other side, cubic-CeO_2 with respectively lower loadings served in boosting the power density up to 31.76%. This can be attributed to the oxygen storage capacity accompanied by the crystal facets. It is well known for CeO_2 that the crystallographic plane concentration can facilitate/alter the movement of oxygen within [179]. For instance, in terms of oxygen capacity, the [100] plane of nano-cubes can store more oxygen than irregular CeO_2 [180]. They also exceed that of [110]/[100] of nanorods which in turn exceeds [111]/[100] of nanopolyhedra [181]. To further illustrate the effect of morphology on the performance of the electrode, 20% cubic, rod, and octahedral CeO_2 were compared as shown in Figure 35 and Table 8. The results have shown a greater performance of cubic-shaped CeO_2 at low current density compared to nanorod CeO_2. This was clearly seen upon comparing the current density recorded at 0.6V in which cubic-CeO_2 recorded 541.2 $mA.cm^{-2}$ while nanorod-CeO_2 recorded 523.9 $mA.cm^{-2}$ (3.2% less). However, nanorod-CeO_2 exhibited a notable outperformance at high current density. This can be related to facilitated mass transfer which can be attributed to the higher pore volume exhibited by nanorod-CeO_2 compared to that of cubic-CeO_2. This resulted in an overall higher power density output accompanied by nanorod-CeO_2 utilization. On the other hand, octahedral-CeO_2 showed an even slightly higher performance in the low current density region (575.6 $mA.cm^{-2}$ at 0.6V) while reasonably retaining at higher current density. As a result, octahedral-CeO_2 resulted in a high-power output of 483.4 $mW.cm^{-2}$.

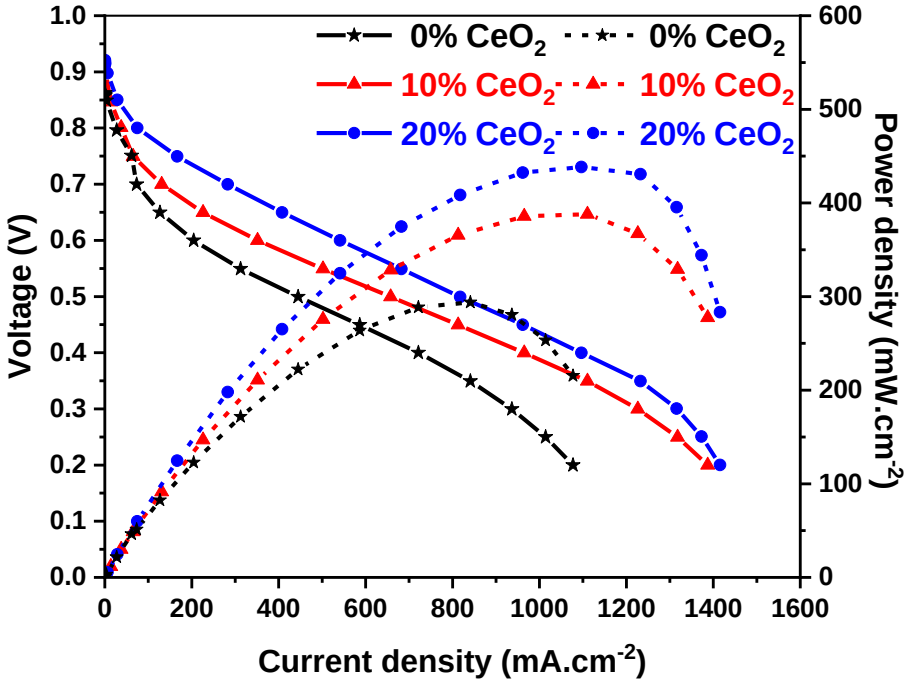

Figure 33: Polarization curves of MEAs with cathodes of 0.15 mg.cm^{-2} and variable amount of cubic-CeO_2 additive

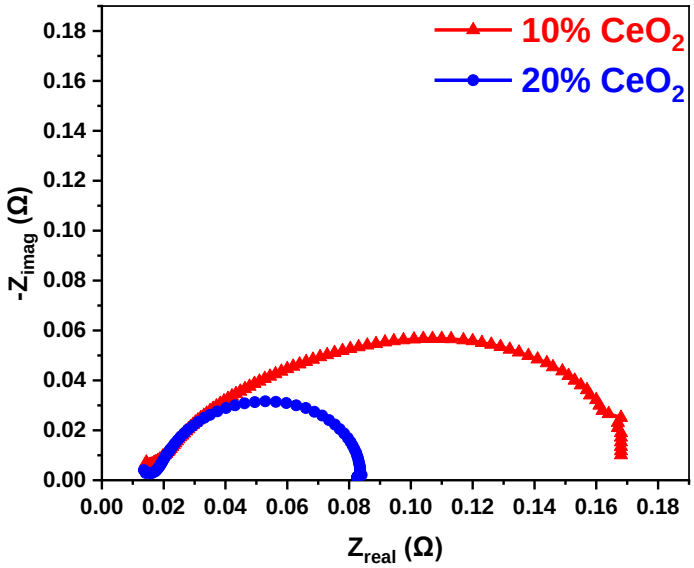

Figure 34: EIS Nyquist plots of MEAs with cathodes containing 10% and 20% cubic-CeO_2 collected at a bias potential of 0.6V

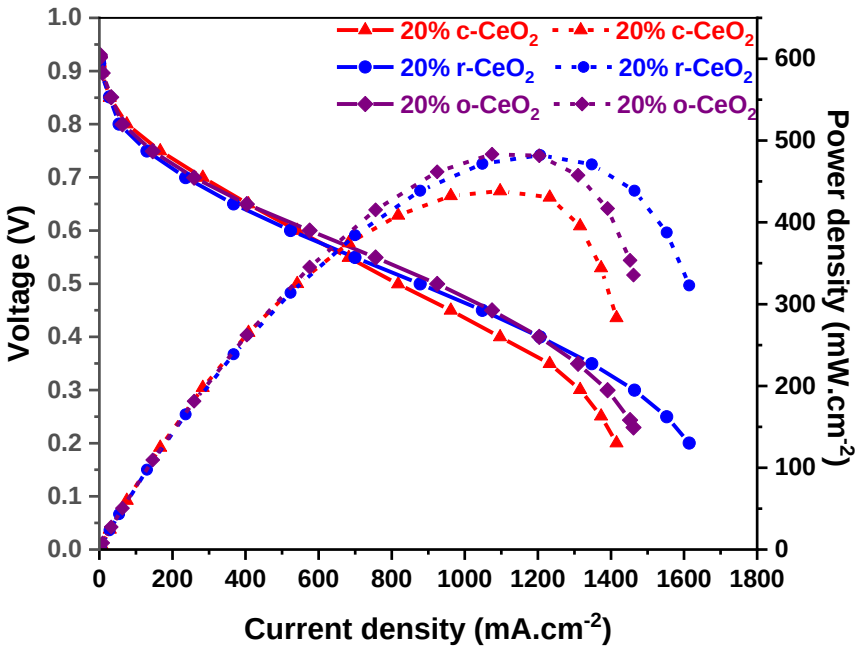

Figure 35: Polarization curve of cubic CeO_2 (c-CeO_2), rod CeO_2 (r-CeO_2), and octahedral CeO_2 (o-CeO_2) obtained at 100 RH, 0.125/0.5 H_2/air feed and 25 psi back pressure

Table 8: The recorded current density, maximum power density for MEAs containing cathodes with 10% and 20% cubic-CeO_2, 20% nanorod CeO_2, and octahedral CeO_2

		BOL		30000 cycles	
CeO_2 morphology	Amount of cubic-CeO_2 additive (%)	Current density at 0.6V ($mA.cm^{-2}$)	Maximum Power density ($mW.cm^{-2}$)	Current density at 0.6V ($mA.cm^{-2}$)	Maximum Power density ($mW.cm^{-2}$)
Cube	10	351.4	387.9	376.8	317.0
Cube	20	541.4	430.6	441.4	352.0
Rod	20	523.9	474.3	391.9	286.7
Octahedron	20	575.6	483.4	365.2	274.7

Pt-dissolution AST was performed for the aforementioned electrodes containing 10% and 20% cubic-CeO_2 (Figure 36). Both loadings have shown a similar behavior after 30000 cycles of AST. Expectedly, a decline in performance was noticed in the low current density (kinetics) region. This is correlated to the Pt dissolution/agglomeration. As a result, 376.82 (9.27% decrease) and 441.39 $mA.cm^{-2}$ (18.48% decrease) current density were recorded at 0.6V for 10% and 20% cubic-CeO_2 loaded cathodes after 30000 AST cycles, respectively. The greater decrease in current density for the higher cubic-CeO_2 seemed unexpected.

However, the hydrophilic nature of CeO_2 can help retain water within the electrodes. This in turn results in increasing the Pt dissolution rate [182]. It is worth noting here that even after Pt-dissolution AST, the current density at 0.6 V for both loadings is still higher than that of electrodes without any cubic-CeO_2 (204.67 $mA.cm^{-2}$ at 0.6 V). Regarding the power output, the 10% cubic-CeO_2 suffered a loss of 24.43% of its maximum power density compared to 19.70% for 20% cubic-CeO_2 loaded cathodes. It is worth mentioning that the power output loss extent for the cubic-CeO_2 loaded electrodes is remarkable compared to additive free electrodes reported elsewhere in the literature which retains only 50% of its power output after Pt AST [63].

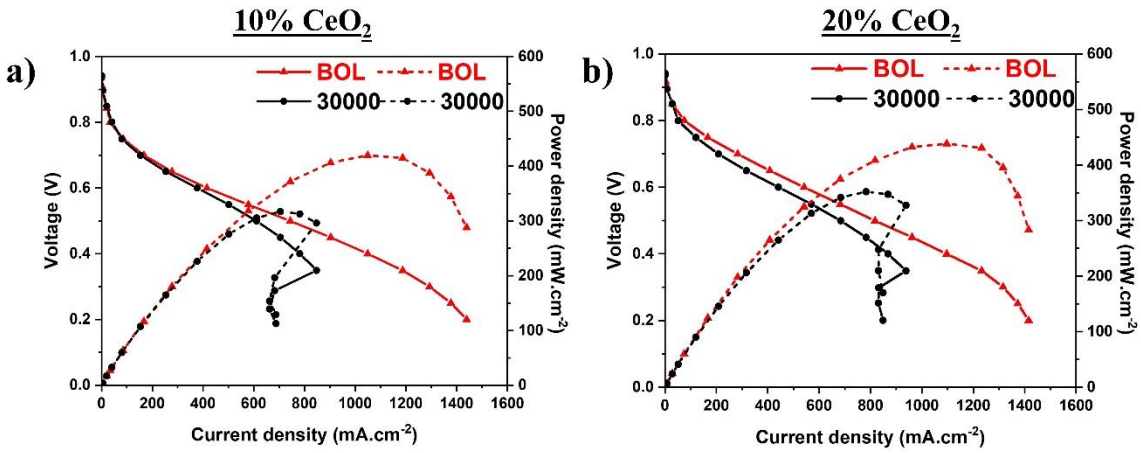

Figure 36: Polarization curve at BOL and after 30000 Pt-dissolution AST cycles of a) 10% cubic CeO_2 and b) 20% cubic CeO_2 containing electrodes

To have a deeper insight into the effect of CeO_2 morphology on the durability of the Pt/C catalyst, Pt-dissolution AST tests were performed, and the polarization curves and Nyquist plots of the MEA at BOL and after 30000 cycles are shown in Figure 37 and Table 8. Expectedly, a drop in performance was evident for all electrodes at all current density regions. However, the degree of decline in performance has shown to be morphology dependent. The different morphologies of CeO_2 can contribute to stabilizing Pt to different degrees. For instance, upon comparing the current density at 0.6V, cubic CeO_2 containing electrode (Figure 37a) has shown a drop of only 18.4% compared to drastic drop of 38.9% and 36.5% for nanorod CeO_2 (Figure 37b) and octahedral CeO_2 (Figure 37c) containing electrodes, respectively. This was accompanied by a drop in the $R_{ch,t}$ of the electrodes as

shown in their corresponding Nyquist plots. In a similar fashion, cubic, nanorod, and octahedral CeO_2 have shown a decline of 13.1% ,59.8%, and 51.4% of their initial $R_{ch,t}$. This further implies that, depending on their morphology, CeO_2 are able to maintain the ORR activity with minimal depression for extended periods of time.

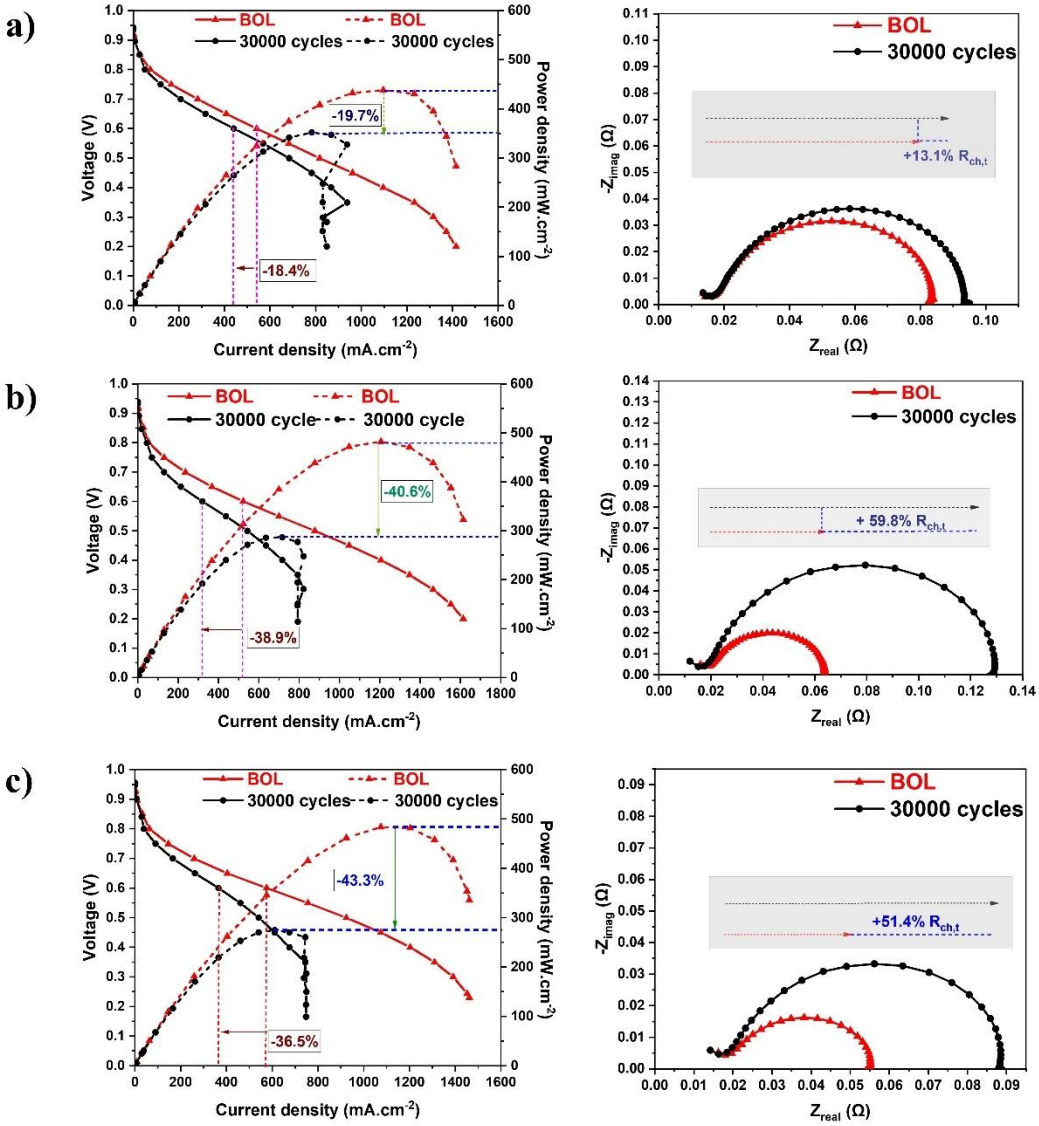

Figure 37: Polarization curves and Nyquist plots of 20% a) cubic CeO_2, b) nanorod CeO_2 and b) octahedral CeO_2 containing electrodes at BOL and after 30000 Pt dissolution AST cycles

5.4. Conclusions

In this study, cubic-CeO_2 and octahedral-CeO_2 were successfully synthesized via a hydrothermal method. This was approved by XRD data which has shown the existence of

cubic-CeO_2 without a significant trace of impurity. The cubic and the octahedral structures was further investigated via SEM which revealed the formation of particles with the aforementioned morphologies. The BET surface area was measured and analyzed to reveal a relatively low surface area (15 $m^2.g^{-1}$) with a low cumulative pore volume and with an average pore size of 19 nm. The electrochemical activity of cubic-CeO_2 was investigated upon incorporating it in sprayed electrodes. In the prepared GDEs, the Pt/C and Nafion® loadings were kept constant while varying the cubic-CeO_2/(Pt/C) loadings. The results have shown an overall enhancement in fuel cell performance (up to 31.8% increase in maximum power density) for cubic-CeO_2 loadings reaching only 0.075 $mg.cm^{-2}$ (20% CeO_2). The ORR activity was further investigated through EIS. The analysis results have shown a drastic decrease in the ORR resistance (R_{ORR}) upon increasing the cubic-CeO_2 loadings. Upon comparing electrodes with fixed platinum loading (0.15 $mg.cm^{-2}$) and fixed additive (20%) but different morphologies, all morphologies showed an enhancement in the overall performance. Remarkably, octahedral CeO_2 showed the highest enhancement in the ORR compared to cubic and rod shaped CeO_2.Cubic-CeO_2 loaded electrodes have shown a remarkable retention in performance after 30000 cycles of Pt-dissolution AST. The MEAs retained up to 80.3% of their initial power output. On the other hand, rod and octahedral shape CeO_2 showed a significant decline in maximum power density reaching 43.3%. This was accompanied by a significant depression in the ORR kinetics where $R_{ch,t}$ showed an increase of 51.4%.

CHAPTER 6: CONCLUSIONS

The main objective of the studies discussed in this dissertation is to amplify the performance and durability of PEMFC electrode through enhancing the different operational processes occurring. First, it was intended to enhance the ORR kinetics through increasing the Pt accessibility. The accessibility of Pt particles was promoted through several methods. The 1st was morphological through tailoring the electrode in a self-standing fibrous array exposing broader Pt surface. The 2nd was additive-based through increasing the accessibility of Pt to oxygen through using CeO_2-based material additives. Second, the study targets a cost-effective cathode through substituting Nafion® proton conducting moiety with a inorganic-based alternative; sulfonated silica (S-SiO_2). Third, self-water management through tuning the hydrophilic (S-SiO_2)- hydrophobic (carrier polymer) content within the fibrous electrode is adhered.

Chapters 1 introduced the main concepts related to polymer electrolyte fuel cells, and electrospinning. Chapter 2 briefly discusses the fundamentals of the characterization methods used within this dissertation. In Chapter 3, Pt/C/S-SiO_2/P(VDF-TrFE) and PVDF nanofibers were fabricated using electrospinning. The fiber mats were morphologically analyzed using SEM, TEM, and mercury intrusion porosimetry. The results proved the continuous distribution of Pt/C and S-SiO_2 particles across the carrier polymer. Furthermore, even overlapping distribution of both Pt/C and S-SiO_2 was observed. MEAs containing electrodes with varying S-SiO_2/carrier polymer, Nafion®/PVDF, and classical sprayed electrodes were prepared and subjected to electrochemical characterization. The results have shown a superior ECSA for fiber-based electrode containing MEAs. Furthermore, an increase in the

ECSA was evident upon increasing the S-SiO_2/carrier polymer ratio. This was translated into better power output and lower ORR resistance through the obtained fuel cell polarization curves and EIS. Furthermore, electrodes with higher S-SiO_2/carrier polymer ratio were able to retain more of their performance when operated in partially humidified conditions (60%RH). In contrast, Pt-dissolution increased with increasing S-SiO_2/carrier polymer ratio. This is due to the increasing water content within the electrodes speeding up Pt dissolution/agglomeration. Furthermore, all electrodes suffered from a mat pore collapse due to polymer degradation resulting in a decline in mass transfer. Carbon corrosion AST revealed enhanced retention of maximum power density with increasing S-SiO_2/carrier polymer ratio which is due to the increase in the Pt/water interface. All in all, a maximum power density performance was obtained of 417.7 $mW.cm^{-2}$ and 86.5% retention in performance after 30000 Pt-dissolution AST and a 2.7 gain in performance after 1000 cycles carbon corrosion AST.

Chapters 4 and 5 dealt mainly with the incorporation of CeO_2-based additives with different morphologies into the cathode and their impact on the ORR. Nanorod-CeO_2, nanorod-CeO_2/NrGO, and cubic-CeO_2 were all synthesized via a hydrothermal method. The chemical composition of the synthesized particles was revealed using XRD ensuring the formation of CeO_2. Morphological characterization (SEM) confirmed the formation of cubic particles. The surface area of the products was analyzed using BET to reveal an enhanced surface area upon decorating NrGO with nanorods of CeO_2 (52 $m^2.g^{-1}$) to form nanorod-CeO_2/NrGO (79 $m^2.g^{-1}$). However, cubic-CeO_2 recorded a much lower surface area and cumulative pore volume (15 $m^2.g^{-1}$). The results have shown that the ORR activity drastically increased upon the introduction of CeO_2-based additives. This is mainly due to the oxygen storage and buffering characteristic of CeO_2. However, this storage capacity varies with the variation of the CeO_2 particle morphology. Upon comparing the performance of MEAs with equal loadings of CeO_2 of different morphologies, it was found that the octahedral morphology showed the highest boost in performance followed by the rod-shaped morphology and the cubic morphology. However, cubic-CeO_2 loaded electrodes 35% increase in performance. Furthermore, cubic-CeO_2 loaded electrodes retained 80.3% of their initial performance.

REFERENCES

[1] Alipour Moghadam Esfahani, R.; Fruehwald, H. M.; Afsahi, F.; Easton, E. B., Enhancing fuel cell catalyst layer stability using a dual-function sulfonated silica-based ionomer. *Applied Catalysis B: Environmental*, *232* (**2018)** 314-321 http://dx.doi.org/:10.1016/j.apcatb.2018.03.080

[2] Dong-Yun Zhang , X. Y., and Zi-Feng Ma, Polarization Curve. In *PEM Fuel Cell Diagnostic Tools*, Haijiang Wang, X.-Z. Y., Hui Li, Ed. CRC Press: 2011; Vol. 1.

[3] J. K. Nørskov, J. R., A. Logadottir, and L. Lindqvist, Origin of the Overpotential for Oxygen Reduction at a Fuel-Cell Cathode. *J Phys Chem*, *108* (**2004)** 17886-17892

[4] Kulkarni, A.; Siahrostami, S.; Patel, A.; Norskov, J. K., Understanding Catalytic Activity Trends in the Oxygen Reduction Reaction. *Chem Rev*, *118* (5) (**2018)** 2302-2312 http://dx.doi.org/:10.1021/acs.chemrev.7b00488

[5] Mistry, H.; Varela, A. S.; Kühl, S.; Strasser, P.; Cuenya, B. R., Nanostructured electrocatalysts with tunable activity and selectivity. *Nature Reviews Materials*, *1* (4) (**2016)** http://dx.doi.org/:10.1038/natrevmats.2016.9

[6] Tritsaris, G. A.; Greeley, J.; Rossmeisl, J.; Nørskov, J. K., Atomic-Scale Modeling of Particle Size Effects for the Oxygen Reduction Reaction on Pt. *Catal Lett*, *141* (7) (**2011)** 909-913 http://dx.doi.org/:10.1007/s10562-011-0637-8

[7] Qiao, Z.; Hwang, S.; Li, X.; Wang, C.; Samarakoon, W.; Karakalos, S.; Li, D.; Chen, M.; He, Y.; Wang, M.; Liu, Z.; Wang, G.; Zhou, H.; Feng, Z.; Su, D.; Spendelow, J. S.; Wu, G., 3D porous graphitic nanocarbon for enhancing the performance and durability of Pt catalysts: a balance between graphitization and hierarchical porosity. *Energy & Environmental Science*, *12* (9) (**2019)** 2830-2841 http://dx.doi.org/:10.1039/c9ee01899a

[8] Yu, X.; Ye, S., Recent advances in activity and durability enhancement of Pt/C catalytic cathode in PEMFC. *J Power Sources*, *172* (1) (**2007)** 133-144 http://dx.doi.org/:10.1016/j.jpowsour.2007.07.049

[9] Kudo, K.; Jinnouchi, R.; Morimoto, Y., Humidity and Temperature Dependences of Oxygen Transport Resistance of Nafion Thin Film on Platinum Electrode. *Electrochim Acta*, *209* (**2016)** 682-690 http://dx.doi.org/:10.1016/j.electacta.2016.04.023

[10] Wang, Y.; Ruiz Diaz, D. F.; Chen, K. S.; Wang, Z.; Adroher, X. C., Materials, technological status, and fundamentals of PEM fuel cells – A review. *Mater Today*, (**2019)** http://dx.doi.org/:10.1016/j.mattod.2019.06.005

[11] Sethuraman, V. A.; Khan, S.; Jur, J. S.; Haug, A. T.; Weidner, J. W., Measuring oxygen, carbon monoxide and hydrogen sulfide diffusion coefficient and solubility in Nafion membranes. *Electrochim Acta*, *54* (27) (**2009)** 6850-6860 http://dx.doi.org/:10.1016/j.electacta.2009.06.068

[12] Fouzaï, I.; Gentil, S.; Bassetto, V. C.; Silva, W. O.; Maher, R.; Girault, H. H., Catalytic layer-membrane electrode assembly methods for optimum triple phase boundaries and fuel cell performances. *Journal of Materials Chemistry A*, *9* (18) (**2021)** 11096-11123 http://dx.doi.org/:10.1039/d0ta07470e

[13] Sasikumar, G.; Ihm, J. W.; Ryu, H., Dependence of optimum Nafion content in catalyst layer on platinum loading. *J Power Sources*, *132* (1-2) (**2004**) 11-17 http://dx.doi.org/:10.1016/j.jpowsour.2003.12.060
[14] Braaten, J. P.; Kariuki, N. N.; Myers, D. J.; Blackburn, S.; Brown, G.; Park, A.; Litster, S., Integration of a high oxygen permeability ionomer into polymer electrolyte membrane fuel cell cathodes for high efficiency and power density. *J Power Sources*, *522* (**2022**) http://dx.doi.org/:10.1016/j.jpowsour.2021.230821
[15] Aylin Rahnavard , S. R., Mohammad Javad Parnian,Gholam Reza Amirkhanlou, The effect of sulfonated poly (ether ether ketone) as the electrode ionomer for self-humidifying nanocomposite proton exchange membrane fuel cells. *Energy*, *82* (**2015**) 746-757 http://dx.doi.org/:10.1016/j.energy.2015.01.086
[16] Jung, H.-Y.; Cho, K.-Y.; Sung, K. A.; Kim, W.-K.; Park, J.-K., The effect of sulfonated poly(ether ether ketone) as an electrode binder for direct methanol fuel cell (DMFC). *J Power Sources*, *163* (1) (**2006**) 56-59 http://dx.doi.org/:10.1016/j.jpowsour.2006.01.075
[17] Virginie Detallante , D. L., Corinne Chappey,Michel Métayer, Régis Mercier, Michel Pinéri Water vapor sorption in naphthalenic sulfonated polyimide membranes. *J Membr Sci*, *190* (**2001**) 227-241 http://dx.doi.org/:10.1016/S0376-7388(01)00437-9
[18] Muldoon, J.; Lin, J.; Wycisk, R.; Takeuchi, N.; Hamaguchi, H.; Saito, T.; Hase, K.; Stewart, F. F.; Pintauro, P. N., High Performance Fuel Cell Operation with a Non-fluorinated Polyphosphazene Electrode Binder. *Fuel Cells*, *9* (5) (**2009**) 518-521 http://dx.doi.org/:10.1002/fuce.200900123
[19] von Kraemer, S.; Puchner, M.; Jannasch, P.; Lundblad, A.; Lindbergh, G. r., Erratum: Gas Diffusion Electrodes and Membrane Electrode Assemblies Based on a Sulfonated Polysulfone for High-Temperature PEMFC [J. Electrochem. Soc., 153, A2077 (2006)]. *J Electrochem Soc*, *153* (12) (**2006**) http://dx.doi.org/:10.1149/1.2374936
[20] Bae, B.; Yoda, T.; Miyatake, K.; Uchida, H.; Watanabe, M., Proton-conductive aromatic ionomers containing highly sulfonated blocks for high-temperature-operable fuel cells. *Angew Chem Int Ed Engl*, *49* (2) (**2010**) 317-20 http://dx.doi.org/:10.1002/anie.200905355
[21] Ng, F.; Bae, B.; Miyatake, K.; Watanabe, M., Polybenzimidazole block sulfonated poly(arylene ether sulfone) ionomers. *Chem Commun (Camb)*, *47* (31) (**2011**) 8895-7 http://dx.doi.org/:10.1039/c1cc12266e
[22] Strong, A.; Britton, B.; Edwards, D.; Peckham, T. J.; Lee, H.-F.; Huang, W. Y.; Holdcroft, S., Alcohol-Soluble, Sulfonated Poly(arylene ether)s: Investigation of Hydrocarbon Ionomers for Proton Exchange Membrane Fuel Cell Catalyst Layers. *J Electrochem Soc*, *162* (6) (**2015**) F513-F518 http://dx.doi.org/:10.1149/2.0251506jes
[23] Eastcott, J. I.; Easton, E. B., Sulfonated silica-based fuel cell electrode structures for low humidity applications. *J Power Sources*, *245* (**2014**) 487-494 http://dx.doi.org/:10.1016/j.jpowsour.2013.07.005
[24] Eastcott, J. I.; Easton, E. B., Investigation of Transport Mechanisms for Sulfonated Silica-Based Fuel Cell Electrode Structures. *J Electrochem Soc*, *162* (7) (**2015**) F764-F771 http://dx.doi.org/:10.1149/2.0841507jes
[25] E. B. Easton, R. A., R. Alipour Moghadam Esfahani, V. J. Cavallari, R. B. Moghaddam, H. M. Fruehwald, and F. Afsahi, Recent Advances with Sulfonated Silica Ceramic Carbon Electrodes for Fuel Cells *ECS Transactions*, *92* (8) (**2019**) 559-570 http://dx.doi.org/:10.1149/09208.0559
[26] Supramaniam Srinivasan, S. M., A. Parthasarathy, A. Cesar Ferreira, Masanobu Wakizoe, Yong Woo Rho, Junbom Kim, Renaut A. Mosdale, Ronald F. Paetzold, James Lee, Shinichi Hirano and A. John Appleby, PROTON EXCHANGE MEMBRANE FUEL CELLS FOR FROM BASIC RESEARCH TO TECHNOLOGY DEVELOPMENT SPACE AND ELECTRIC VEHICLE APPLICATIONS - *Texas A&M University System*, (**1994**) 409-420

[27] D. BEVERS, N. W. a. M. V. B., INNOVATIVE PRODUCTION PROCEDURE FOR LOW COST PEFC ELECTRODES AND ELECTRODE/MEMBRANE STRUCTURES *Int J Hydrogen Energy*, *23* (1) (**1998)** 57-63
[28] Shimshon Gottesfeld, T. A. Z., Polymer Electrolyte Fuel Cells. In *Advances in Electrochemical Science and Engineering,*, Prof. Richard C. Alkire, P. D. H. G., Dieter M. Kolb,Charles W. Tobias, Ed. Wiley: 1997; Vol. 5, pp 195-301.
[29] Şanlı, L. I.; Bayram, V.; Yarar, B.; Ghobadi, S.; Gürsel, S. A., Development of graphene supported platinum nanoparticles for polymer electrolyte membrane fuel cells: Effect of support type and impregnation–reduction methods. *Int J Hydrogen Energy*, *41* (5) (**2016)** 3414-3427 http://dx.doi.org/:10.1016/j.ijhydene.2015.12.166
[30] Mehta, V.; Cooper, J. S., Review and analysis of PEM fuel cell design and manufacturing. *J Power Sources*, *114* (1) (**2003)** 32-53 http://dx.doi.org/:10.1016/s0378-7753(02)00542-6
[31] Talukdar, K.; Helmly, S.; Schulze, M.; Sanchez, D. G.; Handl, M.; Hiesgen, R.; Kraut, J.; Friedrich, K. A., Enveloping of catalyst powder by ionomer for dry spray coating in polymer electrolyte membrane fuel cells. *J Power Sources*, *424* (**2019)** 82-90 http://dx.doi.org/:10.1016/j.jpowsour.2019.03.093
[32] Lei, C.; Yang, F.; Macauley, N.; Spinetta, M.; Purdy, G.; Jankovic, J.; Cullen, D. A.; More, K. L.; Kim, Y. S.; Xu, H., Impact of Catalyst Ink Dispersing Solvent on PEM Fuel Cell Performance and Durability. *J Electrochem Soc*, *168* (4) (**2021)** http://dx.doi.org/:10.1149/1945-7111/abf2b0
[33] Smirnova, A.; Dong, X.; Hara, H.; Vasiliev, A.; Sammes, N., Novel carbon aerogel-supported catalysts for PEM fuel cell application. *Int J Hydrogen Energy*, *30* (2) (**2005)** 149-158 http://dx.doi.org/:10.1016/j.ijhydene.2004.04.014
[34] Parrondo, J.; Mijangos, F.; Rambabu, B., Platinum/tin oxide/carbon cathode catalyst for high temperature PEM fuel cell. *J Power Sources*, *195* (13) (**2010)** 3977-3983 http://dx.doi.org/:10.1016/j.jpowsour.2010.01.027
[35] Xiao-Zi Yuan, H. W., PEM Fuel Cell Catalyst Layers and MEAs. In *PEM Fuel Cell Electrocatalysts and Catalyst Layers: Fundamentals and Applications*, Zhang, J., Ed. Springer-Verlag: London, 2008; pp 355-380.
[36] Litster, S.; McLean, G., PEM fuel cell electrodes. *J Power Sources*, *130* (1-2) (**2004)** 61-76 http://dx.doi.org/:10.1016/j.jpowsour.2003.12.055
[37] Amirinejad, M.; Rowshanzamir, S.; Eikani, M. H., Effects of operating parameters on performance of a proton exchange membrane fuel cell. *J Power Sources*, *161* (2) (**2006)** 872-875 http://dx.doi.org/:10.1016/j.jpowsour.2006.04.144
[38] Chunzhi He, S. D., Garth Brown, and Srinivas Bollepalli, PEM Fuel Cell Catalysts:Cost, Performance, and Durability. *The Electrochemical Society Interface*, *14* (**2005)** 41
[39] Shao-Horn, Y.; Sheng, W. C.; Chen, S.; Ferreira, P. J.; Holby, E. F.; Morgan, D., Instability of Supported Platinum Nanoparticles in Low-Temperature Fuel Cells. *Top Catal*, *46* (3-4) (**2007)** 285-305 http://dx.doi.org/:10.1007/s11244-007-9000-0
[40] Kotaro Sasaki, M. S. R. A., Dissolution and Stabilization of Platinum in Oxygen Cathodes. In *Polymer Electrolyte Fuel Cell Durability*, Felix N. Büchi, M. I., Thomas J. Schmidt, Ed. Springer-Verlag: New York, 2009; pp 7-27.
[41] Shao, Y.; Yin, G.; Gao, Y., Understanding and approaches for the durability issues of Pt-based catalysts for PEM fuel cell. *J Power Sources*, *171* (2) (**2007)** 558-566 http://dx.doi.org/:10.1016/j.jpowsour.2007.07.004
[42] Zhang, J. Z. a. J., Catalyst Layer/MEA Performance Evaluation. In *PEM Fuel cell Electrocatalysts and Catalyst Layers Fundamentals and Applications*, Zhang, J., Ed. Springer-Verlag: London, 2008; pp 965-1002.
[43] Haider, A.; Haider, S.; Kang, I.-K., A comprehensive review summarizing the effect of electrospinning parameters and potential applications of nanofibers in biomedical and

biotechnology. *Arabian Journal of Chemistry*, *11* (8) (**2018)** 1165-1188 http://dx.doi.org/:10.1016/j.arabjc.2015.11.015
[44] Sill, T. J.; von Recum, H. A., Electrospinning: applications in drug delivery and tissue engineering. *Biomaterials*, *29* (13) (**2008)** 1989-2006 http://dx.doi.org/:10.1016/j.biomaterials.2008.01.011
[45] Silke Megelski, J. S. S., D. Bruce Chase, and John F. Rabolt, Micro- and Nanostructured Surface Morphology on Electrospun Polymer Fibers. *Macromolecules*, *35* (**2002)** 8456-8466
[46] De Vrieze, S.; Van Camp, T.; Nelvig, A.; Hagström, B.; Westbroek, P.; De Clerck, K., The effect of temperature and humidity on electrospinning. *Journal of Materials Science*, *44* (5) (**2009)** 1357-1362 http://dx.doi.org/:10.1007/s10853-008-3010-6
[47] Pillay, V.; Dott, C.; Choonara, Y. E.; Tyagi, C.; Tomar, L.; Kumar, P.; du Toit, L. C.; Ndesendo, V. M. K., A Review of the Effect of Processing Variables on the Fabrication of Electrospun Nanofibers for Drug Delivery Applications. *Journal of Nanomaterials*, *2013* (**2013)** 1-22 http://dx.doi.org/:10.1155/2013/789289
[48] Haider, S.; Al-Zeghayer, Y.; Ahmed Ali, F. A.; Haider, A.; Mahmood, A.; Al-Masry, W. A.; Imran, M.; Aijaz, M. O., Highly aligned narrow diameter chitosan electrospun nanofibers. *Journal of Polymer Research*, *20* (4) (**2013)** http://dx.doi.org/:10.1007/s10965-013-0105-9
[49] Angammana, C. J.; Jayaram, S. H., Analysis of the Effects of Solution Conductivity on Electrospinning Process and Fiber Morphology. *IEEE Transactions on Industry Applications*, *47* (3) (**2011)** 1109-1117 http://dx.doi.org/:10.1109/tia.2011.2127431
[50] Lannutti, J.; Reneker, D.; Ma, T.; Tomasko, D.; Farson, D., Electrospinning for tissue engineering scaffolds. *Materials Science and Engineering: C*, *27* (3) (**2007)** 504-509 http://dx.doi.org/:10.1016/j.msec.2006.05.019
[51] Seigo Kotera, H. W., Katsuya Fujii,Ichiro Terada,Chie Matsubara, Hiroshi Uyama, Study on the cathode fabricated by spinning process and its performance in PEFC. *ECS Transactions*, *25* (1) (**2009)** 821-830
[52] Zhang, W.; Pintauro, P. N., High-performance nanofiber fuel cell electrodes. *ChemSusChem*, *4* (12) (**2011)** 1753-7 http://dx.doi.org/:10.1002/cssc.201100245
[53] Brodt, M.; Wycisk, R.; Pintauro, P. N., Nanofiber Electrodes with Low Platinum Loading for High Power Hydrogen/Air PEM Fuel Cells. *J Electrochem Soc*, *160* (8) (**2013)** F744-F749 http://dx.doi.org/:10.1149/2.008308jes
[54] Hong Chen, J. D. S., and Yossef A. Elabd, Electrospinning and Solution Properties of Nafion and Poly(acrylic acid). *Macromolecules*, *41* (**2008)** 128-135
[55] Brodt, M.; Han, T.; Dale, N.; Niangar, E.; Wycisk, R.; Pintauro, P., Fabrication, In-Situ Performance, and Durability of Nanofiber Fuel Cell Electrodes. *J Electrochem Soc*, *162* (1) (**2014)** F84-F91 http://dx.doi.org/:10.1149/2.0651501jes
[56] Kabir, S.; Van Cleve, T.; Khandavalli, S.; Medina, S.; Pylypenko, S.; Mauger, S.; Ulsh, M.; Neyerlin, K. C., Toward Optimizing Electrospun Nanofiber Fuel Cell Catalyst Layers: Microstructure and Pt Accessibility. *ACS Applied Energy Materials*, *4* (4) (**2021)** 3341-3351 http://dx.doi.org/:10.1021/acsaem.0c03073
[57] Wenjing Zhang, M. W. B., and Peter N. Pintauro Nanofiber Cathodes for Low and High Humidity Hydrogen Fuel Cell Operation *ECS Transactions*, *41* (1) (**2011)** 891-899
[58] Meyers, J. P.; Darling, R. M., Model of Carbon Corrosion in PEM Fuel Cells. *J Electrochem Soc*, *153* (8) (**2006)** http://dx.doi.org/:10.1149/1.2203811
[59] Young, A. P.; Stumper, J.; Gyenge, E., Characterizing the Structural Degradation in a PEMFC Cathode Catalyst Layer: Carbon Corrosion. *J Electrochem Soc*, *156* (8) (**2009)** http://dx.doi.org/:10.1149/1.3139963

[60] Liu, H.; Si, D.; Ding, H.; Wang, S.; Zhang, J.; Liu, Y., Cold start capability and durability of electrospun catalyst layer for proton exchange membrane fuel cell. *Int J Hydrogen Energy*, *46* (19) (**2021)** 11140-11149 http://dx.doi.org/:10.1016/j.ijhydene.2020.06.032
[61] Brodt, M.; Wycisk, R.; Dale, N.; Pintauro, P., Power Output and Durability of Electrospun Fuel Cell Fiber Cathodes with PVDF and Nafion/PVDF Binders. *J Electrochem Soc*, *163* (5) (**2016)** F401-F410 http://dx.doi.org/:10.1149/2.0711605jes
[62] Su, H.; Pasupathi, S.; Bladergroen, B.; Linkov, V.; Pollet, B. G., Optimization of gas diffusion electrode for polybenzimidazole-based high temperature proton exchange membrane fuel cell: Evaluation of polymer binders in catalyst layer. *Int J Hydrogen Energy*, *38* (26) (**2013)** 11370-11378 http://dx.doi.org/:10.1016/j.ijhydene.2013.06.107
[63] Slack, J. J.; Brodt, M.; Cullen, D. A.; Reeves, K. S.; More, K. L.; Pintauro, P. N., Impact of Polyvinylidene Fluoride on Nanofiber Cathode Structure and Durability in Proton Exchange Membrane Fuel Cells. *J Electrochem Soc*, *167* (5) (**2020)** http://dx.doi.org/:10.1149/1945-7111/ab77fb
[64] Si, D.; Zhang, S.; Huang, J.; Wang, C.; Liu, Y.; Zhang, J., Electrochemical Characterization of Pre-conditioning Process of Electrospun Nanofiber Electrodes in Polymer Electrolyte Fuel Cells. *Fuel Cells*, *18* (5) (**2018)** 576-585 http://dx.doi.org/:10.1002/fuce.201700209
[65] Slack, J. J.; Gumeci, C.; Dale, N.; Parrondo, J.; Macauley, N.; Mukundan, R.; Cullen, D.; Sneed, B.; More, K.; Pintauro, P. N., Nanofiber Fuel Cell MEAs with a PtCo/C Cathode. *J Electrochem Soc*, *166* (7) (**2019)** F3202-F3209 http://dx.doi.org/:10.1149/2.0151907jes
[66] Slack, J.; Halevi, B.; McCool, G.; Li, J.; Pavlicek, R.; Wycisk, R.; Mukerjee, S.; Pintauro, P., Electrospun Fiber Mat Cathode with Platinum-Group-Metal-Free Catalyst Powder and Nafion/PVDF Binder. *ChemElectroChem*, *5* (12) (**2018)** 1537-1542 http://dx.doi.org/:10.1002/celc.201800283
[67] Hong, S.; Hou, M.; Zhang, H.; Jiang, Y.; Shao, Z.; Yi, B., A high-performance PEM fuel cell with ultralow platinum electrode via electrospinning and underpotential deposition. *Electrochim Acta*, *245* (**2017)** 403-409 http://dx.doi.org/:10.1016/j.electacta.2017.05.066
[68] Schwarz, K., Materials design of solid electrolytes. *The National Academy of Sciences of the USA*, *103* (10) (**2006)** 3497
[69] Juan P. Holgado, R. A., Guillermo Munuera, Study of CeO XPS spectra by factor analysis: reduction of CeO_2 *Appl Surf Sci*, *161* (**2000)** 301-315
[70] M. Romeo, K. B., J. El Fallah, F. Le Normand and L. Hilaire, XPS Study of the Reduction of Cerium Dioxide *Surf Interface Anal*, *20* (**1993)** 508-512
[71] Deshpande, S.; Patil, S.; Kuchibhatla, S. V. N. T.; Seal, S., Size dependency variation in lattice parameter and valency states in nanocrystalline cerium oxide. *Appl Phys Lett*, *87* (13) (**2005)** http://dx.doi.org/:10.1063/1.2061873
[72] Lawrence, N. J.; Brewer, J. R.; Wang, L.; Wu, T. S.; Wells-Kingsbury, J.; Ihrig, M. M.; Wang, G.; Soo, Y. L.; Mei, W. N.; Cheung, C. L., Defect engineering in cubic cerium oxide nanostructures for catalytic oxidation. *Nano Lett*, *11* (7) (**2011)** 2666-71 http://dx.doi.org/:10.1021/nl200722z
[73] Chen, J.; Patil, S.; Seal, S.; McGinnis, J. F., Rare earth nanoparticles prevent retinal degeneration induced by intracellular peroxides. *Nat Nanotechnol*, *1* (2) (**2006)** 142-50 http://dx.doi.org/:10.1038/nnano.2006.91
[74] Herman, G. S., Characterization of surface defects on epitaxial CeO_2 (001) films. *Surf Sci*, *437* (**1999)** 207-214
[75] De Souza, R. A.; Ramadan, A.; Hörner, S., Modifying the barriers for oxygen-vacancy migration in fluorite-structured CeO2electrolytes through strain: a computer simulation study. *Energy Environ Sci*, *5* (1) (**2012)** 5445-5453 http://dx.doi.org/:10.1039/c2ee02508f

[76] Migani, A.; Vayssilov, G. N.; Bromley, S. T.; Illas, F.; Neyman, K. M., Greatly facilitated oxygen vacancy formation in ceria nanocrystallites. *Chem Commun (Camb)*, *46* (32) (**2010)** 5936-8 http://dx.doi.org/:10.1039/c0cc01091j
[77] Jiang, Y.; Adams, J. B.; van Schilfgaarde, M., Density-functional calculation of CeO2 surfaces and prediction of effects of oxygen partial pressure and temperature on stabilities. *J Chem Phys*, *123* (6) (**2005)** 64701 http://dx.doi.org/:10.1063/1.1949189
[78] Sun, C.; Li, H.; Chen, L., Nanostructured ceria-based materials: synthesis, properties, and applications. *Energy & Environmental Science*, *5* (9) (**2012)** http://dx.doi.org/:10.1039/c2ee22310d
[79] Lim, D.-H.; Lee, W.-D.; Choi, D.-H.; Kwon, H.-H.; Lee, H.-I., The effect of cerium oxide nanoparticles on a Pt/C electrocatalyst synthesized by a continuous two-step process for low-temperature fuel cell. *Electrochem Commun*, *10* (4) (**2008)** 592-596 http://dx.doi.org/:10.1016/j.elecom.2008.02.001
[80] Motoi Takahashi, T. M., Hirotaka Togasaki, Keisuke Fugane,Akio Tada, Vladimir Matolin and John Drennan Influence of Pt and Ce02 iteraction in Pt-Ce02 electrode on anode and cathode performance for fuel cell applications *Transactions of the Materials Research Society ofJapan*, *33* (4) (**2008)** 1101-1104
[81] Lee, K. H.; Kwon, K.; Roev, V.; Yoo, D. Y.; Chang, H.; Seung, D., Synthesis and characterization of nanostructured PtCo-CeOx/C for oxygen reduction reaction. *J Power Sources*, *185* (2) (**2008)** 871-875 http://dx.doi.org/:10.1016/j.jpowsour.2008.09.029
[82] Zhao, J.; Chen, W.; Zheng, Y., Effect of ceria on carbon supported platinum catalysts for methanol electrooxidation. *Mater Chem Phys*, *113* (2-3) (**2009)** 591-595 http://dx.doi.org/:10.1016/j.matchemphys.2008.07.107
[83] Lim, D.-H.; Lee, W.-D.; Choi, D.-H.; Lee, H.-I., Effect of ceria nanoparticles into the Pt/C catalyst as cathode material on the electrocatalytic activity and durability for low-temperature fuel cell. *Applied Catalysis B: Environmental*, *94* (1-2) (**2010)** 85-96 http://dx.doi.org/:10.1016/j.apcatb.2009.10.024
[84] Fugane, K.; Mori, T.; Ou, D. R.; Suzuki, A.; Yoshikawa, H.; Masuda, T.; Uosaki, K.; Yamashita, Y.; Ueda, S.; Kobayashi, K.; Okazaki, N.; Matolinova, I.; Matolin, V., Activity of oxygen reduction reaction on small amount of amorphous CeO promoted Pt cathode for fuel cell application. *Electrochim Acta*, *56* (11) (**2011)** 3874-3883 http://dx.doi.org/:10.1016/j.electacta.2011.02.034
[85] S. Michael Stewart, R. L. B., Mahlon S. Wilson, Abhaya Datye and Fernando H. Garzon, Ceria and Doped Ceria Nanoparticle Additives For Polymer Fuel Cell Lifetime Improvement. *ECS Transactions*, *64* (**2014)** 403
[86] Pearman, B. P.; Mohajeri, N.; Brooker, R. P.; Rodgers, M. P.; Slattery, D. K.; Hampton, M. D.; Cullen, D. A.; Seal, S., The degradation mitigation effect of cerium oxide in polymer electrolyte membranes in extended fuel cell durability tests. *J Power Sources*, *225* (**2013)** 75-83 http://dx.doi.org/:10.1016/j.jpowsour.2012.10.015
[87] Lei, M.; Wang, Z. B.; Li, J. S.; Tang, H. L.; Liu, W. J.; Wang, Y. G., CeO2 nanocubes-graphene oxide as durable and highly active catalyst support for proton exchange membrane fuel cell. *Sci Rep*, *4* (**2014)** 7415 http://dx.doi.org/:10.1038/srep07415
[88] Joseph Goldstein , D. E. N., David C. Joy, Charles E. Lyman, Patrick Echlin, Eric Lifshin , Linda Sawyer, J.R. Michael, *Scanning Electron Microscopy and X-Ray Microanalysis- Third Edition*. Springer US: United States 2003;
[89] David B. Williams, C. B. C., *Transmission Electron Microscopy A Textbook for Materials Science*. Springer New York: Newyork, 2009;
[90] B. D. Cullity and , S. R. S., *Elements of X-ray Diffraction*. Prentice-Hall: New Jersey, 2001; Vol. 3,

[91] Naderi, M., Surface Area: Brunauer–Emmett–Teller (BET). In *Progress in Filtration and Separation*, Tarleton, S., Ed. Elsevier: 2015; pp 585-608.
[92] Wagner, N., Electrochemical Impedance Spectroscopy. In *PEM FUEL CELL DURABILITY HANDBOOK*, Haijiang Wang, X.-Z. Y., and Hui Li, Ed. CRC Press: London, 2011; pp 37-70.
[93] Xiao-Zi Yuan, C. S., Haijiang Wang, Jiujun Zhang, *Electrochemical Impedance Spectroscopy in PEM Fuel Cells Fundamentals and Applications*. Springer: London 2010;
[94] Jinfeng Wu, X.-Z. Y., Haijiang Wang, Cyclic Voltammetry. In *PEM Fuel Cell Diagnostic Tools*, Haijiang Wang, X.-Z. Y., Hui Li, Ed. CRC Press: London 2011; pp 71-84.
[95] Cooper, K. R., In Situ PEM Fuel Cell Electrochemical Surface Area and Catalyst Utilization Measurement. *Fuel Cell Magazine*, (**2009)**
[96] Chi Linh Do, T. S. P., Ngoc Phong Nguyen and Viet Quan Tran, Properties of Pt/C nanoparticle catalysts synthesized by electroless deposition for proton exchange membrane fuel cell. *Advances in Natural Sciences: Nanoscience and Nanotechnology*, *4* (**2013)** 035011
[97] Inaba, M.; Kinumoto, T.; Kiriake, M.; Umebayashi, R.; Tasaka, A.; Ogumi, Z., Gas crossover and membrane degradation in polymer electrolyte fuel cells. *Electrochim Acta*, *51* (26) (**2006)** 5746-5753 http://dx.doi.org/:10.1016/j.electacta.2006.03.008
[98] Yu, J.; Matsuura, T.; Yoshikawa, Y.; Islam, M. N.; Hori, M., In Situ Analysis of Performance Degradation of a PEMFC under Nonsaturated Humidification. *Electrochem Solid-State Lett*, *8* (3) (**2005)** http://dx.doi.org/:10.1149/1.1854781
[99] Shengsheng Zhang, X.-Z. Y., Haijiang Wang, Linear Sweep Voltammetry. In *PEM Fuel Cell Diagnostic Tools*, Haijiang Wang, X.-Z. Y., Hui Li, Ed. CRC Press: Londin 2011; pp 87-98.
[100] Wang, J.; Zhao, C.-X.; Liu, J.-N.; Ren, D.; Li, B.-Q.; Huang, J.-Q.; Zhang, Q., Quantitative kinetic analysis on oxygen reduction reaction: A perspective. *Nano Materials Science*, *3* (3) (**2021)** 313-318 http://dx.doi.org/:10.1016/j.nanoms.2021.03.006
[101] Zhang, X.-Q.; Zhao, C.-Z.; Huang, J.-Q.; Zhang, Q., Recent Advances in Energy Chemical Engineering of Next-Generation Lithium Batteries. *Engineering*, *4* (6) (**2018)** 831-847 http://dx.doi.org/:10.1016/j.eng.2018.10.008
[102] Shubbak, M. H., Advances in solar photovoltaics: Technology review and patent trends. *Renewable and Sustainable Energy Reviews*, *115* (**2019)** http://dx.doi.org/:10.1016/j.rser.2019.109383
[103] Zegers, P., Fuel cell commercialization: The key to a hydrogen economy. *J Power Sources*, *154* (2) (**2006)** 497-502 http://dx.doi.org/:10.1016/j.jpowsour.2005.10.051
[104] Kocha, S. S., Polymer Electrolyte Membrane (PEM) Fuel Cells: Automotive Applications. In *Fuel Cells and Hydrogen Production: A Volume in the Encyclopedia of Sustainability Science and Technology, Second Edition*, Lipman, T. E.; Weber, A. Z., Eds. Springer New York: New York, NY, 2019; pp 135-171.
[105] Ahluwalia, R. K.; Wang, X.; Kwon, J.; Rousseau, A.; Kalinoski, J.; James, B.; Marcinkoski, J., Performance and cost of automotive fuel cell systems with ultra-low platinum loadings. *J Power Sources*, *196* (10) (**2011)** 4619-4630 http://dx.doi.org/:10.1016/j.jpowsour.2011.01.059
[106] Muthukumar, M.; Rengarajan, N.; Velliyangiri, B.; Omprakas, M. A.; Rohit, C. B.; Kartheek Raja, U., The development of fuel cell electric vehicles – A review. *Materials Today: Proceedings*, *45* (**2021)** 1181-1187 http://dx.doi.org/:10.1016/j.matpr.2020.03.679
[107] Wang, Y.; Chen, K. S.; Mishler, J.; Cho, S. C.; Adroher, X. C., A review of polymer electrolyte membrane fuel cells: Technology, applications, and needs on fundamental research. *Applied Energy*, *88* (4) (**2011)** 981-1007 http://dx.doi.org/:10.1016/j.apenergy.2010.09.030
[108] L. Carrette, K. A. F. a. U. S., Fuel Cells -Fundamentals and Applications. *FUEL CELLS*, *1* (1) 5-39

[109] Choi, S.; Yuk, S.; Lee, D.-H.; Doo, G.; Lee, D. W.; Choo, M.-J.; Kim, H.-T., Rugged catalyst layer supported on a Nafion fiber mat for enhancing mass transport of polymer electrolyte membrane fuel cells. *Electrochim Acta*, *268* (**2018)** 469-475 http://dx.doi.org/:10.1016/j.electacta.2018.02.097
[110] Tsuchiya, H., Mass production cost of PEM fuel cell by learning curve. *Int J Hydrogen Energy*, *29* (10) (**2004)** 985-990 http://dx.doi.org/:10.1016/j.ijhydene.2003.10.011
[111] Gagliardi, G. G.; Ibrahim, A.; Borello, D.; El-Kharouf, A., Composite Polymers Development and Application for Polymer Electrolyte Membrane Technologies—A Review. *Molecules*, *25* (7) (**2020)** http://dx.doi.org/:10.3390/molecules25071712
[112] Wang, X. X.; Swihart, M. T.; Wu, G., Achievements, challenges and perspectives on cathode catalysts in proton exchange membrane fuel cells for transportation. *Nature Catalysis*, *2* (7) (**2019)** 578-589 http://dx.doi.org/:10.1038/s41929-019-0304-9
[113] Cullen, D. A.; Neyerlin, K. C.; Ahluwalia, R. K.; Mukundan, R.; More, K. L.; Borup, R. L.; Weber, A. Z.; Myers, D. J.; Kusoglu, A., New roads and challenges for fuel cells in heavy-duty transportation. *Nature Energy*, *6* (5) (**2021)** 462-474 http://dx.doi.org/:10.1038/s41560-021-00775-z
[114] Jason Marcinkoski, R. V., Jesse Adams, Brian James, John Kopasz, Rajesh Ahluwalia, DOE Advanced Truck Technologies :Subsection of the Electrified Powertrain Roadmap Technical Targets for Hydrogen-Fueled Long-Haul Tractor-Trailer Trucks.
[115] Jha, S.; Bhandary, N.; Basu, S.; Ingole, P. P., Electro-deposited Pt3Co on Carbon Fiber Paper as Nafion-Free Electrode for Enhanced Electro-catalytic Activity toward Oxygen Reduction Reaction. *ACS Applied Energy Materials*, *2* (9) (**2019)** 6269-6279 http://dx.doi.org/:10.1021/acsaem.9b00849
[116] Martin, S.; Garcia-Ybarra, P. L.; Castillo, J. L., High platinum utilization in ultra-low Pt loaded PEM fuel cell cathodes prepared by electrospraying. *Int J Hydrogen Energy*, *35* (19) (**2010)** 10446-10451 http://dx.doi.org/:10.1016/j.ijhydene.2010.07.069
[117] Ganesan, A.; Narayanasamy, M., Ultra-low loading of platinum in proton exchange membrane-based fuel cells: a brief review. *Materials for Renewable and Sustainable Energy*, *8* (4) (**2019)** http://dx.doi.org/:10.1007/s40243-019-0156-x
[118] Park, H.-S.; Cho, Y.-H.; Cho, Y.-H.; Park, I.-S.; Jung, N.; Ahn, M.; Sung, Y.-E., Modified Decal Method and Its Related Study of Microporous Layer in PEM Fuel Cells. *J Electrochem Soc*, *155* (5) (**2008)** http://dx.doi.org/:10.1149/1.2844420
[119] Sasikumar, G.; Ihm, J. W.; Ryu, H., Optimum Nafion content in PEM fuel cell electrodes. *Electrochim Acta*, *50* (2-3) (**2004)** 601-605 http://dx.doi.org/:10.1016/j.electacta.2004.01.126
[120] Millington, B.; Whipple, V.; Pollet, B. G., A novel method for preparing proton exchange membrane fuel cell electrodes by the ultrasonic-spray technique. *J Power Sources*, *196* (20) (**2011)** 8500-8508 http://dx.doi.org/:10.1016/j.jpowsour.2011.06.024
[121] Thanasilp, S.; Hunsom, M., Effect of MEA fabrication techniques on the cell performance of Pt–Pd/C electrocatalyst for oxygen reduction in PEM fuel cell. *Fuel*, *89* (12) (**2010)** 3847-3852 http://dx.doi.org/:10.1016/j.fuel.2010.07.008
[122] Wang, M.; Park, J. H.; Kabir, S.; Neyerlin, K. C.; Kariuki, N. N.; Lv, H.; Stamenkovic, V. R.; Myers, D. J.; Ulsh, M.; Mauger, S. A., Impact of Catalyst Ink Dispersing Methodology on Fuel Cell Performance Using in-Situ X-ray Scattering. *ACS Applied Energy Materials*, *2* (9) (**2019)** 6417-6427 http://dx.doi.org/:10.1021/acsaem.9b01037
[123] Waldrop, K.; Wycisk, R.; Pintauro, P. N., Application of electrospinning for the fabrication of proton-exchange membrane fuel cell electrodes. *Current Opinion in Electrochemistry*, *21* (**2020)** 257-264 http://dx.doi.org/:10.1016/j.coelec.2020.03.007

[124] Hong, S.; Hou, M.; Xiao, Y.; Shao, Z.; Yi, B., Investigation of a High-Performance Nanofiber Cathode with Ultralow Platinum Loading for Proton Exchange Membrane Fuel Cells. *Energy Technology*, *5* (8) (**2017)** 1457-1463 http://dx.doi.org/:10.1002/ente.201600734
[125] Lu, Y.; Jiang, Y.; Lou, Z.; Shi, R.; Chen, D.; Shen, G., Wearable supercapacitor self-charged by P(VDF-TrFE) piezoelectric separator. *Progress in Natural Science: Materials International*, *30* (2) (**2020)** 174-179 http://dx.doi.org/:10.1016/j.pnsc.2020.01.023
[126] Chung, M. H.; Yoo, S.; Kim, H. J.; Yoo, J.; Han, S. Y.; Yoo, K. H.; Jeong, H., Enhanced output performance on LbL multilayer PVDF-TrFE piezoelectric films for charging supercapacitor. *Sci Rep*, *9* (1) (**2019)** 6581 http://dx.doi.org/:10.1038/s41598-019-43098-6
[127] Ico, G.; Showalter, A.; Bosze, W.; Gott, S. C.; Kim, B. S.; Rao, M. P.; Myung, N. V.; Nam, J., Size-dependent piezoelectric and mechanical properties of electrospun P(VDF-TrFE) nanofibers for enhanced energy harvesting. *Journal of Materials Chemistry A*, *4* (6) (**2016)** 2293-2304 http://dx.doi.org/:10.1039/c5ta10423h
[128] Lee, J.-H.; Yoon, H.-J.; Kim, T. Y.; Gupta, M. K.; Lee, J. H.; Seung, W.; Ryu, H.; Kim, S.-W., Micropatterned P(VDF-TrFE) Film-Based Piezoelectric Nanogenerators for Highly Sensitive Self-Powered Pressure Sensors. *Adv Funct Mater*, *25* (21) (**2015)** 3203-3209 http://dx.doi.org/:10.1002/adfm.201500856
[129] Nunes-Pereira, J.; Ribeiro, S.; Ribeiro, C.; Gombek, C. J.; Gama, F. M.; Gomes, A. C.; Patterson, D. A.; Lanceros-Méndez, S., Poly(vinylidene fluoride) and copolymers as porous membranes for tissue engineering applications. *Polym Test*, *44* (**2015)** 234-241 http://dx.doi.org/:10.1016/j.polymertesting.2015.05.001
[130] Rajabalizadeh Mojarrad, N.; Iskandarani, B.; Taşdemir, A.; Yürüm, A.; Alkan Gürsel, S.; Yarar Kaplan, B., Nanofiber based hybrid sulfonated silica/P(VDF-TrFE) membranes for PEM fuel cells. *Int J Hydrogen Energy*, *46* (25) (**2021)** 13583-13593 http://dx.doi.org/:10.1016/j.ijhydene.2020.08.005
[131] Kim, T.; Lee, J.; Yang, T.-H.; Yoon, Y.-G.; Park, S.-H.; Yim, S.-D., Novel catalyst layer synthesized by an in situ sol–gel process with tetraethoxysilane in a Nafion ionomer solution with Pt/C for PEFCs: the effect of self-assembled Nafion–SiO2 on Pt ORR activity and an increased water content in the polymer membranes. *RSC Advances*, *2* (17) (**2012)** http://dx.doi.org/:10.1039/c2ra20796f
[132] LIN-KK tool. https://www.iam.kit.edu/et/english/Lin-KK.php (accessed December , 2021).
[133] Lohmann-Richters, F. P.; Abel, B.; Varga, Á., In situ determination of the electrochemically active platinum surface area: key to improvement of solid acid fuel cells. *Journal of Materials Chemistry A*, *6* (6) (**2018)** 2700-2707 http://dx.doi.org/:10.1039/c7ta10110d
[134] Atsushi Ohma, K. S., Akihiro Iiyama, Toshihiko Yoshida ,and Akimasa Daimaru, Membrane and Catalyst Performance Targets for Automotive Fuel Cells by FCCJ Membrane, Catalyst, MEA WG *ECS Transactions*, *41* (1) (**2011)** 775-784
[135] He, G.; Nie, L.; Han, X.; Dong, H.; Li, Y.; Wu, H.; He, X.; Hu, J.; Jiang, Z., Constructing facile proton-conduction pathway within sulfonated poly(ether ether ketone) membrane by incorporating poly(phosphonic acid)/silica nanotubes. *J Power Sources*, *259* (**2014)** 203-212 http://dx.doi.org/:10.1016/j.jpowsour.2014.02.091
[136] R. Byron Bird, W. E. S., Edwin N. Lightfoot, Transport Phenomena, Revised 2nd Edition. *Wiley*, (**2006)**
[137] Warren McCabe , J. S., Peter Harriott Unit Operations of Chemical Engineering, 7th Edition. *McGraw-Hill, Newyork*, (**2005)**
[138] Yu, Z.; Carter, R. N.; Zhang, J., Measurements of Pore Size Distribution, Porosity, Effective Oxygen Diffusivity, and Tortuosity of PEM Fuel Cell Electrodes. *Fuel Cells*, *12* (4) (**2012)** 557-565 http://dx.doi.org/:10.1002/fuce.201200017

[139] Zhao, J.; Shahgaldi, S.; Alaefour, I.; Xu, Q.; Li, X., Gas permeability of catalyzed electrodes in polymer electrolyte membrane fuel cells. *Applied Energy*, *209* (**2018)** 203-210 http://dx.doi.org/:10.1016/j.apenergy.2017.10.087
[140] Larbi, B.; Alimi, W.; Chouikh, R.; Guizani, A., Effect of porosity and pressure on the PEM fuel cell performance. *Int J Hydrogen Energy*, *38* (20) (**2013)** 8542-8549 http://dx.doi.org/:10.1016/j.ijhydene.2012.11.022
[141] Perego, A.; Avid, A.; Mamania, D. N.; Chen, Y.; Atanassov, P.; Yildirim, H.; Odgaard, M.; Zenyuk, I. V., Investigation of cathode catalyst layer interfaces evolution during accelerated stress tests for polymer electrolyte fuel cells. *Applied Catalysis B: Environmental*, *301* (**2022)** http://dx.doi.org/:10.1016/j.apcatb.2021.120810
[142] Liu, Y.; Ji, C.; Gu, W.; Baker, D. R.; Jorne, J.; Gasteiger, H. A., Proton Conduction in PEM Fuel Cell Cathodes: Effects of Electrode Thickness and Ionomer Equivalent Weight. *J Electrochem Soc*, *157* (8) (**2010)** http://dx.doi.org/:10.1149/1.3435323
[143] Kallenberger, P. A.; Fröba, M., Water harvesting from air with a hygroscopic salt in a hydrogel–derived matrix. *Communications Chemistry*, *1* (1) (**2018)** http://dx.doi.org/:10.1038/s42004-018-0028-9
[144] Ergün, A. N.; Kocabaş, Z. Ö.; Yürüm, A.; Yürüm, Y., Diffusion of alcohols and aromatics in a mesoporous MCM-41 material. *Fluid Phase Equilib*, *382* (**2014)** 169-179 http://dx.doi.org/:10.1016/j.fluid.2014.09.009
[145] Ergün, A. N.; Kocabaş, Z. Ö.; Baysal, M.; Yürüm, A.; Yürüm, Y., Synthesis of Mesoporous Mcm-41 Materials with Low-Power Microwave Heating. *Chem Eng Commun*, *200* (8) (**2013)** 1057-1070 http://dx.doi.org/:10.1080/00986445.2012.737386
[146] Kregar, A.; Kravos, A.; Katrašnik, T., Methodology for Evaluation of Contributions of Ostwald Ripening and Particle Agglomeration to Growth of Catalyst Particles in PEM Fuel Cells. *Fuel Cells*, *20* (4) (**2020)** 487-498 http://dx.doi.org/:10.1002/fuce.201900208
[147] Inan, T. Y.; Doğan, H.; Unveren, E. E.; Eker, E., Sulfonated PEEK and fluorinated polymer based blends for fuel cell applications: Investigation of the effect of type and molecular weight of the fluorinated polymers on the membrane's properties. *Int J Hydrogen Energy*, *35* (21) (**2010)** 12038-12053 http://dx.doi.org/:10.1016/j.ijhydene.2010.07.084
[148] Okonkwo, P. C.; Otor, C., A review of gas diffusion layer properties and water management in proton exchange membrane fuel cell system. *International Journal of Energy Research*, *45* (3) (**2020)** 3780-3800 http://dx.doi.org/:10.1002/er.6227
[149] S.kocha, S., *Polymer Electrolyte Fuel Cell Degradation, Chapter 3: Electrochemical Degradation: Electrocatalyst and Support Durability*. Academic Press: Boston: 2012;
[150] Peden, C. T. C. a. C. H. F., Oxygen Vacancies and Catalysis on Ceria Surfaces. *Science*, *309* (5735) (**2005)** 713-714
[151] Swartz, S. L., *Catalysis by Ceria and Related Materials*. Journal of American Chemical Society: London, 2002; Vol. 2,
[152] Leandro Gonza´lez-Rovira, J. M. S. n.-A., Miguel Lo´pez-Haro, Eloy del Rio, Ana B. Hungrı´a, Paul Midgley, Jose´ J. Calvino, Serafı´n Bernal, and F. Javier Botana, Single-Step Process To Prepare CeO_2 Nanotubes with Improved Catalytic Activity. *Nano Lett*, *9* (4) (**2009)** 1395-1400
[153] Dean C. Sayle, S. A. M., and Graeme W. Watson, Atomistic Models for CeO_2(111), (110), and (100) Nanoparticles, Supported on Yttrium-Stabilized Zirconia. *American Chemical Society*, *124* (**2002)** 11429-11439
[154] Wu, Z.; Li, M.; Howe, J.; Meyer, H. M., 3rd; Overbury, S. H., Probing defect sites on CeO2 nanocrystals with well-defined surface planes by Raman spectroscopy and O2 adsorption. *Langmuir*, *26* (21) (**2010)** 16595-606 http://dx.doi.org/:10.1021/la101723w

[155] Ma, Z.; Yuan, X.; Li, L.; Ma, Z.-F.; Wilkinson, D. P.; Zhang, L.; Zhang, J., A review of cathode materials and structures for rechargeable lithium–air batteries. *Energy & Environmental Science*, *8* (8) (**2015)** 2144-2198 http://dx.doi.org/:10.1039/c5ee00838g
[156] Işıkel Şanlı, L.; Bayram, V.; Ghobadi, S.; Düzen, N.; Alkan Gürsel, S., Engineered catalyst layer design with graphene-carbon black hybrid supports for enhanced platinum utilization in PEM fuel cell. *Int J Hydrogen Energy*, *42* (2) (**2017)** 1085-1092 http://dx.doi.org/:10.1016/j.ijhydene.2016.08.210
[157] Quesnel, E.; Roux, F.; Emieux, F.; Faucherand, P.; Kymakis, E.; Volonakis, G.; Giustino, F.; Martín-García, B.; Moreels, I.; Gürsel, S. A.; Yurtcan, A. B.; Noto, V. D.; Talyzin, A.; Baburin, I.; Tranca, D.; Seifert, G.; Crema, L.; Speranza, G.; Tozzini, V.; Bondavalli, P.; Pognon, G.; Botas, C.; Carriazo, D.; Singh, G.; Rojo, T.; Kim, G.; Yu, W.; Grey, C. P.; Pellegrini, V., Graphene-based technologies for energy applications, challenges and perspectives. *2D Materials*, *2* (3) (**2015)** http://dx.doi.org/:10.1088/2053-1583/2/3/030204
[158] Chen, P.; Xiao, T. Y.; Qian, Y. H.; Li, S. S.; Yu, S. H., A nitrogen-doped graphene/carbon nanotube nanocomposite with synergistically enhanced electrochemical activity. *Adv Mater*, *25* (23) (**2013)** 3192-6 http://dx.doi.org/:10.1002/adma.201300515
[159] Sung, C.-C.; Liu, C.-Y.; Cheng, C. C. J., Durability improvement at high current density by graphene networks on PEM fuel cell. *Int J Hydrogen Energy*, *39* (22) (**2014)** 11706-11712 http://dx.doi.org/:10.1016/j.ijhydene.2014.05.154
[160] Al-Tememy, M. G. H.; Devrim, Y., Development of effective bimetallic catalyst for high-temperature

PEM

fuel cell to improve

CO

tolerance. *International Journal of Energy Research*, *45* (2) (**2020)** 3343-3357 http://dx.doi.org/:10.1002/er.6032
[161] Sanjeev Mukerjee, S. S., and Manuel P. Soriaga,James McBreen, Effect of Preparation Conditions of Pt Alloys on Their Electronic, Structural, and Electrocatalytic Activities for Oxygen Reduction—XRD, XAS, and Electrochemical Studies. *J Phys Chem*, *99* (**1995)** 4577-4589
[162] Trogadas, P.; Parrondo, J.; Mijangos, F.; Ramani, V., Degradation mitigation in PEM fuel cells using metal nanoparticle additives. *J Mater Chem*, *21* (48) (**2011)** http://dx.doi.org/:10.1039/c1jm14077a
[163] Mamat, M. S.; Grigoriev, S. A.; Dzhus, K. A.; Grant, D. M.; Walker, G. S., The performance and degradation of Pt electrocatalysts on novel carbon carriers for PEMFC applications. *Int J Hydrogen Energy*, *35* (14) (**2010)** 7580-7587 http://dx.doi.org/:10.1016/j.ijhydene.2010.04.147
[164] Matthew H. Frey, D. M. P., Steven J. Hamrock HIGH DURABILITY FUEL CELL COMPONENTS WITH CERIUM OXDE ADDITIVES 2013.
[165] Ehlinger, V. M.; Crothers, A. R.; Kusoglu, A.; Weber, A. Z., Modeling proton-exchange-membrane fuel cell performance/degradation tradeoffs with chemical scavengers. *Journal of Physics: Energy*, *2* (4) (**2020)** http://dx.doi.org/:10.1088/2515-7655/abb194
[166] Ostroverkh, A.; Johánek, V.; Dubau, M.; Kúš, P.; Khalakhan, I.; Šmíd, B.; Fiala, R.; Václavů, M.; Ostroverkh, Y.; Matolín, V., Optimization of ionomer-free ultra-low loading Pt catalyst for anode/cathode of PEMFC via magnetron sputtering. *Int J Hydrogen Energy*, *44* (35) (**2019)** 19344-19356 http://dx.doi.org/:10.1016/j.ijhydene.2018.12.206
[167] Breitwieser, M.; Bayer, T.; Büchler, A.; Zengerle, R.; Lyth, S. M.; Thiele, S., A fully spray-coated fuel cell membrane electrode assembly using Aquivion ionomer with a graphene

oxide/cerium oxide interlayer. *J Power Sources*, *351* (**2017)** 145-150 http://dx.doi.org/:10.1016/j.jpowsour.2017.03.085
[168] Mori, T.; Ou, D. R.; Zou, J.; Drennan, J., Present status and future prospect of design of Pt–cerium oxide electrodes for fuel cell applications. *Progress in Natural Science: Materials International*, *22* (6) (**2012)** 561-571 http://dx.doi.org/:10.1016/j.pnsc.2012.11.010
[169] Nováková, J.; Dubau, M.; Fuka, Š.; Duchoň, T.; Johánek, V.; Fiala, R.; Veltruská, K.; Potin, V.; Matolín, V.; Matolínová, I., Role of nitrogenated carbon in tuning Pt-CeOx based anode catalysts for higher performance of hydrogen-powered fuel cells. *Appl Surf Sci*, *515* (**2020)** http://dx.doi.org/:10.1016/j.apsusc.2020.146054
[170] Chourashiya, M.; Gyergyek, S.; Andersen, S. M., Solution combustion synthesized ceria or alumina supported Pt as cathode electrocatalyst for PEM fuel cells. *Mater Chem Phys*, *242* (**2020)** http://dx.doi.org/:10.1016/j.matchemphys.2019.122444
[171] Tasdemir, A.; Bulut Kopuklu, B.; Kirlioglu, A. C.; Alkan Gursel, S.; Yurum, A., The influence of nitrogen doping on reduced graphene oxide as highly cyclable Li-ion battery anode with enhanced performance. *Int J Hydrogen Energy*, *46* (21) (**2021)** 11865-11877 http://dx.doi.org/:10.1016/j.ijhydene.2021.01.099
[172] Yarar Kaplan, B.; Haghmoradi, N.; Jamil, E.; Merino, C.; Alkan Gürsel, S., Platinum nanoparticles decorated carbon nanofiber hybrids as highly active electrocatalysts for polymer electrolyte membrane fuel cells. *International Journal of Energy Research*, *44* (13) (**2020)** 10251-10261 http://dx.doi.org/:10.1002/er.5646
[173] Yarar Kaplan, B.; Haghmoradi, N.; Biçer, E.; Merino, C.; Alkan Gürsel, S., High performance electrocatalysts supported on graphene based hybrids for polymer electrolyte membrane fuel cells. *Int J Hydrogen Energy*, *43* (52) (**2018)** 23221-23230 http://dx.doi.org/:10.1016/j.ijhydene.2018.10.222
[174] Sevim Yılmaz, M.; Kaplan, B. Y.; Metin, Ö.; Gürsel, S. A., A facile synthesis and assembly of ultrasmall Pt nanoparticles on reduced graphene oxide-carbon black hybrid for enhanced performance in PEMFC. *Materials & Design*, *151* (**2018)** 29-36 http://dx.doi.org/:10.1016/j.matdes.2018.04.041
[175] Ruichun Jiang, F. D. C., Timothy J. Fuller CERIUM NANOFIBER ADDITIVES FOR IMPROVED FUEL CELL DURABILITY. 2021.
[176] Lin, R.; Cao, C.; Zhang, H.; Huang, H.; Ma, J., Electro-catalytic activity of enhanced CO tolerant cerium-promoted Pt/C catalyst for PEM fuel cell anode. *Int J Hydrogen Energy*, *37* (5) (**2012)** 4648-4656 http://dx.doi.org/:10.1016/j.ijhydene.2011.05.021
[177] Brkovic, S. M.; Marceta Kaninski, M. P.; Lausevic, P. Z.; Saponjic, A. B.; Radulovic, A. M.; Rakic, A. A.; Pasti, I. A.; Nikolic, V. M., Non-stoichiometric tungsten-carbide-oxide-supported Pt–Ru anode catalysts for PEM fuel cells – From basic electrochemistry to fuel cell performance. *Int J Hydrogen Energy*, *45* (27) (**2020)** 13929-13938 http://dx.doi.org/:10.1016/j.ijhydene.2020.03.086
[178] Yazici, M. S.; Dursun, S.; Borbáth, I.; Tompos, A., Reformate gas composition and pressure effect on CO tolerant Pt/Ti0.8Mo0.2O2–C electrocatalyst for PEM fuel cells. *Int J Hydrogen Energy*, *46* (25) (**2021)** 13524-13533 http://dx.doi.org/:10.1016/j.ijhydene.2020.08.226
[179] Naganuma, T., Shape design of cerium oxide nanoparticles for enhancement of enzyme mimetic activity in therapeutic applications. *Nano Research*, *10* (1) (**2016)** 199-217 http://dx.doi.org/:10.1007/s12274-016-1278-4
[180] Zhang, J.; Kumagai, H.; Yamamura, K.; Ohara, S.; Takami, S.; Morikawa, A.; Shinjoh, H.; Kaneko, K.; Adschiri, T.; Suda, A., Extra-low-temperature oxygen storage capacity of CeO2 nanocrystals with cubic facets. *Nano Lett*, *11* (2) (**2011)** 361-4 http://dx.doi.org/:10.1021/nl102738n

[181] Hao-Xin Mai, L.-D. S., Ya-Wen Zhang, Rui Si, Wei Feng, Hong-Peng Zhang, Hai-Chao Liu, and Chun-Hua Yan, Shape-Selective Synthesis and Oxygen Storage Behavior of Ceria Nanopolyhedra, Nanorods, and Nanocubes. *J Phys Chem*, *109* (**2005)** 24380-24385
[182] Iskandarani, B.; Rajabalizadeh Mojarrad, N.; Yürüm, A.; Alkan Gürsel, S.; Yarar Kaplan, B., Electrospun Nanofiber Electrodes for Boosted Performance and Durability at Lower Humidity Operation of PEM Fuel Cells. *Energy & Fuels*, *36* (16) (**2022)** 9282-9294 http://dx.doi.org/:10.1021/acs.energyfuels.2c01595